British Geological Survey
NATURAL ENVIRONMENT RESEARCH COUNCIL

Mineralogical investigations of the interaction between iron corrosion products and bentonite from the NF-PRO Experiments (Phase 2)

Chemical and Biological Hazards Programme

Commissioned Report CR/07/225N

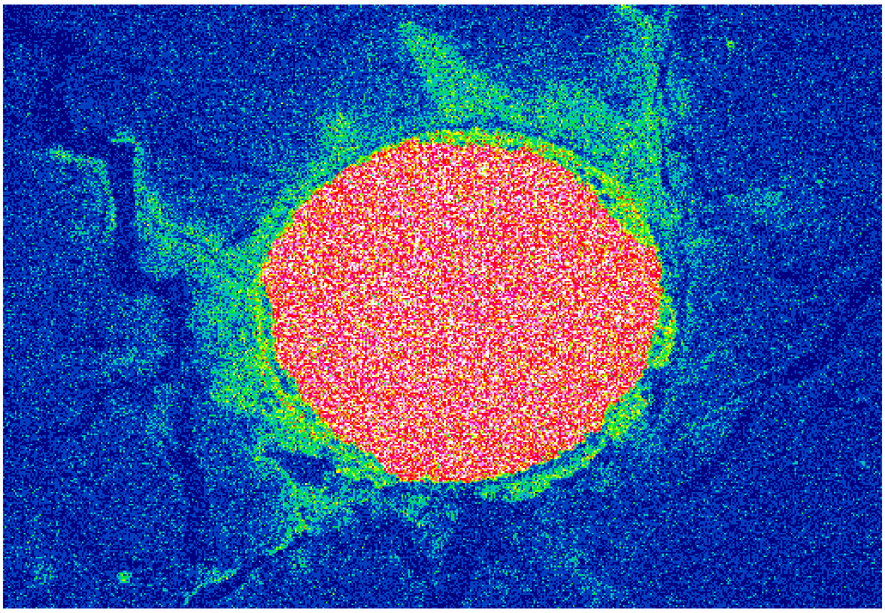

BRITISH GEOLOGICAL SURVEY

COMMISSIONED REPORT CR/07/225N

Mineralogical investigations of the interaction between iron corrosion products and bentonite from the NF-PRO Experiments (Phase 2)

A.E. Milodowski, M.R. Cave, S.J. Kemp, H. Taylor, K. Green, C.L. Williams, R.A. Shaw, C.J.B. Gowing and N.D. Eatherington

Key words

Iron corrosion, radioactive waste, spent fuel, bentonite, smectite, chlorite, iron oxides, aragonite, ion exchange, exchangeable cations. .

Front cover

Energy-dispersive X-ray map showing the distribution of iron around a corroding carbon steel wire within bentonite matrix (in polished thin section). Field of view = 0.85 mm wide. Serco Assurance NF-PRO Experiment NFC12.

Bibliographical reference

MILODOWSKI, A E, CAVE, M R, KEMP, S J, TAYLOR, H, GREEN, K, WILLIAMS, C L, SHAW, R A, GOWING, C J AND EATHERINGTON, N D. 2007. Mineralogical investigations of the interaction between iron corrosion products and bentonite from the NF-PRO Experiments (Phase 2). *British Geological Survey Commissioned Report*, CR/07/225N. 76pp.

Keyworth, Nottingham British Geological Survey 2007

BRITISH GEOLOGICAL SURVEY

The full range of Survey publications is available from the BGS Sales Desks at Nottingham and Edinburgh; see contact details below or shop online at www.thebgs.co.uk

The London Information Office maintains a reference collection of BGS publications including maps for consultation.

The Survey publishes an annual catalogue of its maps and other publications; this catalogue is available from any of the BGS Sales Desks.

The British Geological Survey carries out the geological survey of Great Britain and Northern Ireland (the latter as an agency service for the government of Northern Ireland), and of the surrounding continental shelf, as well as its basic research projects. It also undertakes programmes of British technical aid in geology in developing countries as arranged by the Department for International Development and other agencies.

The British Geological Survey is a component body of the Natural Environment Research Council.

Keyworth, Nottingham NG12 5GG
☎ 0115-936 3241 Fax 0115-936 3488
e-mail: sales@bgs.ac.uk
www.bgs.ac.uk
Shop online at: www.thebgs.co.uk

Murchison House, West Mains Road, Edinburgh EH9 3LA
☎ 0131-667 1000 Fax 0131-668 2683
e-mail: scotsales@bgs.ac.uk

London Information Office at the Natural History Museum (Earth Galleries), Exhibition Road, South Kensington, London SW7 2DE
☎ 020-7589 4090 Fax 020-7584 8270
☎ 020-7942 5344/45 email: bgslondon@bgs.ac.uk

Forde House, Park Five Business Centre, Harrier Way, Sowton, Exeter, Devon EX2 7HU
☎ 01392-445271 Fax 01392-445371

Geological Survey of Northern Ireland, 20 College Gardens, Belfast BT9 6BS
☎ 028-9066 6595 Fax 028-9066 2835

Maclean Building, Crowmarsh Gifford, Wallingford, Oxfordshire OX10 8BB
☎ 01491-838800 Fax 01491-692345

Parent Body

Natural Environment Research Council, Polaris House, North Star Avenue, Swindon, Wiltshire SN2 1EU
☎ 01793-411500 Fax 01793-411501
www.nerc.ac.uk

Foreword

This report is the published product of a study by the British Geological Survey (BGS) commissioned by the Svensk Kärnbränslehantering AB (SKB) to provide background mineralogical information, for laboratory experiments on the interaction between iron corrosion products and bentonite, undertaken on behalf of SKB by Serco Assurance as part of European Union Framework VI project NF-PRO (Smart et al., 2006). This report forms the second of two studies on the post-experimental mineralogical characterisation of residues from the NF-PRO experiments. The results of the Phase 1 mineralogical investigation are presented in an earlier report by Milodowski et al. (2007). The purpose of these BGS investigations were to determine whether or not there is mineralogical or geochemical evidence for clay mineral alteration by Fe within the bentonite.

Acknowledgements

Dr Nick Smart (Serco Assurance) is acknowledged for providing background information on the experimental studies and helpful discussions on the interpretation of the data. Dr Lars Werme (SKB) and Dr Virginia Oversby are also thanked for his support and encouragement during the project.

Contents

FIGURES

TABLES

Summary

This report describes the findings of a second programme of work (Phase 2) undertaken by the British Geological Survey (BGS) on behalf of Svensk Kärnbränslehantering AB (SKB), to characterise the mineralogical alteration of samples of compacted bentonite from experiments that SKB have co-funded in a study by Serco Assurance (Culham Laboratory, Oxfordshire, United Kingdom) to investigate the interaction of iron and bentonite, within the EU Framework 6 NF-PRO Project (Smart et al., 2006).

Reacted bentonite residues from four NF-PRO Experiments – NFC1, NFC4, NFC7 and NFC13 were examined by BGS using; X-ray diffraction analysis (XRD); petrographical analysis with backscattered scanning electron microscopy (BSEM) with energy-dispersive X-ray microanalysis (EDXA) techniques, cation exchange capacity (CEC) and exchangeable cation analysis; and sequential chemical extraction. In addition, background chemical analysis of altered and background bentonite were also obtained by X-ray fluorescence spectrometry (XRFS).

Bentonite immediately adjacent to corroding steel wires was found to have interacted with Fe released from the corroding metal. This resulted in the formation of narrow haloes of altered bentonite around the corroding steel wires, in which the clay matrix was significantly enriched in Fe. Similar observations were observed in bentonite around corroded iron coupons (observed in experiments NFC4 and NFC7 only), although the alteration zones were not as well developed in comparison to those around corroded steel wires. Detailed petrographical observation found no evidence for the formation discrete iron oxide or iron oxyhydroxide phases within the clay matrix but appeared to show that the clay particles themselves had become enriched in Fe. However, data from sequential chemical extraction suggests that a significant proportion (26 to 68 %) of the iron in the altered bentonite is present as amorphous iron oxide or crystalline iron oxides (15 to 33 % of the total iron). Some of the crystalline iron is present as primary magnetite and ilmenite present from the original MX-80 bentonite but part of this will also probably be secondary magnetite formed as a corrosion product of the steel. Nevertheless, sequential chemical extraction analyses also suggest that a large proportion of the iron (11-38 %) may be present within the silicate/clay mineral lattice. The implication of this would be that there has been significant conversion of the original montmorillonite to an Fe-rich clay mineral within these alteration haloes. Although XRD does not detect very much change in clay mineralogy, and suggests that the smectite in the altered bentonite is dioctahedral, it is likely that the subsampling for XRD analysis was on too coarse a scale to be able to resolve the alteration within these very narrow reaction zones around the corroded wires.

The alteration observed around the corroded steel wires in experiments NFC4, NFC7 and NFC13 is more complex than that in NFC1 or earlier experiments studied in Phase 1 (Milodowski et al., 2007) or previously by Smart et al. (2006). The reacted bentonite from these experiments exhibited the formation of a Mg-Fe-rich clay mineral or aluminosilicate alteration product. This was formed within the Fe-enriched alteration halo but appears to have formed relatively early and was subsequently partially overprinted or replaced by more Fe-rich aluminosilicate. EDXA microchemical mapping did suggest some slight Mg enhancement in the reacted bentonite from NFC1 but no discrete Mg-rich phase was detected. Whilst Mg may potentially have been derived from the "Allard" reference water used in experiment NFC4, in the case of NFC7 and NFC13 it could only have been derived from the breakdown of the bentonite itself since the porefluid only contained NaCl in these two experiments.

XRD observations indicated a slight increase in d_{002}/d_{003} peak ratio, which could possibly be accounted for by a small amount of substitution of Fe into the octahedral layers of the smectite. This is not supported by exchangeable cation analyses, which show very little exchangeable Fe to be present within the altered bentonite. The cation exchange capacity (CEC) and exchangeable cation chemistry of the bentonite show very little difference in properties between

reacted and background bentonite. However, it is also possible that the subsampling for exchangeable cation analysis was also on too coarse a scale to be able to resolve such changes within the fine alteration haloes.

Fe released from the corroding steel was also observed to displace Ca^{2+} from the interlayer cation sites in the montmorillonite component. This was manifested by the marked concentration of Ca at the interface with the corroding metal and along the leading edges of ‘fronts’ of Fe diffusing into the bentonite matrix. The displaced Ca was seen to have re-precipitated as aragonite.

The petrographical observations show that the bentonite within the alteration zone, that has reacted with and is enriched by Fe, has a tendency to show significantly reduced shrinkage on sample drying than the unaltered bentonite. Conversely, this would suggest that the reacted and altered clay will also have less ability to swell on hydration with water. This behaviour might be consistent with the partial conversion of the montmorillonite to an iron rich dioctahedral smectite such as nontronite. If this is the case, then this may have important implications for the long-term behaviour of bentonite seals around radioactive waste canisters made of iron or steel.

1 Introduction

The Svensk Kärnbränslehantering AB (SKB) disposal concept for the disposal of spent fuel and high-level radioactive waste considers using a system that consists of a copper-clad iron waste canister that is surrounded by bentonite clay, and emplaced within an underground repository located in crystalline basement rocks. The canister and the bentonite act as the engineered barrier that is designed to prevent the release of radionuclides into the biosphere. Initially, the disposal concept design was for emplacement of the canisters and bentonite over-pack within vertical disposal holes drilled within the galleries of an underground repository in granitic host rocks. More recently consideration has also been given to emplacement within horizontally drilled boreholes, which has advantages with respect to reducing the size and height that is required in the excavated repository galleries. However, emplacement in horizontal disposal holes requires a steel 'cage' to be used to hold the bentonite blocks in place around the canister, and to provide strength to prevent deformation of the canister, during its emplacement.

One aspect of concern, regarding the long-term stability and integrity of the barrier system, is the effect of possible interactions that might occur between the iron and steel components and the bentonite buffer material. Of particular concern are whether or not the bentonite might enhance iron corrosion, and whether or not the oxidation of iron and its iron corrosion products might interact with the bentonite, thereby altering its swelling/sealing, ion exchange, sorption and radionuclide retardation properties. Potentially important changes that might be expected in bentonite as a result of interaction with iron and its corrosion products include:

- Substitution of interlayer cations such as Na^+ and Ca^{2+} in the smectite component by Fe^{2+} produced by iron corrosion (Kamei et al., 1999; Idemitsu et al., 2003);
- Reduction of Fe^{3+} in octahedral structural sites in the smectite clay mineral component by the oxidation of the adjacent metallic iron (Stuki, 1984; Kostka et al., 1999);
- Alteration (transformation) of smectite to a Fe-rich clay mineral such as mixed-layer chlorite-smectite or chlorite (e.g. Wilson et al., 2006a,b).

In order to investigate these problems, the SKB have co-funded an experimental study by Serco Assurance (Culham Laboratory, Oxfordshire, United Kingdom) to investigate the interaction of iron and bentonite, within the EU Framework 6 NF-PRO Project (Smart et al., 2006). Initial results from the Serco Assurance experiments have indicated higher than expected rates of iron corrosion, and significant increases in Fe content have been identified in the bentonite in contact with the corroding iron. However, the analyses of the experimental residues have been inconclusive in regard to either (i) the reason for the enhanced corrosion; (ii) the nature of the Fe enhancement in the bentonite, or; (iii) evidence for any alteration or transformation of the smectite clay mineral component to an Fe-rich phase. Consequently, the British Geological Survey (BGS) were requested by SKB (Dr Lars Werme) to undertake a programme of specialist mineralogical analyses to characterise the clay mineralogy and determine the iron distribution characteristics within the reacted bentonite residues from the Serco Assurance experiments that have been completed to date. This was undertaken in two stages: (i) Phase 1 (reported previously by Milodowski et al., 2007), examined the alteration characteristics in experiments NFC12, NFC16 and NFC17, and; (ii) Phase 2 (the subject of this report), examined the alteration characteristics from experiments NFC1, NFC4, NFC7 and NFC13. The purpose of the BGS investigations was to determine whether or not there is evidence for clay mineral alteration by Fe within the bentonite. The results will be used to help guide the future characterisation of experimental residues from further Serco Assurance experiments that are currently in progress.

2 The iron-bentonite interaction experiment samples

The experimental system of the bentonite-iron interaction experiments conducted by Serco Assurance is described by Smart et al. (2006). It consists of a series of experimental cells containing composite cylinders of compacted bentonite with iron coupons and steel wires. These were loaded into a stainless steel holder, which was designed to allow artificial groundwater to enter the bentonite and gas to escape through porous sintered metal filters (gas permeable). The cells were then placed within a stainless steel pressure vessel (cf. Figure 1 in Smart et al. 2006). The composite bentonite cylinders used in the experiments comprised two discrete components (illustrated schematically in Figure 1):

- A central region consisting of MX-80 bentonite dry mixed with carbon steel wires (5 mm in length, 0.45 mm diameter), then compressed to form a short cylinder. This was sandwiched between:
- An outer region of compacted MX-80 bentonite at either end of the composite cylinder, containing a flat coupon of iron.

The composition of the steel wires used in the experiments is reported by Smart et al. (2006) as BS4360 grade 43A (EN1024B-1) carbon steel (composition wt % C 0.21; Si 0.220; Mn 0.7; S 0.017; P 0.017, balance = Fe).

The experiments were conducted in an oxygen-free nitrogen-flushed glove box to study iron corrosion under a reducing environment. The experimental conditions for the reacted bentonite from the three cells examined in this study are given in Table 1 (data provided by Dr N R Smart, Serco Assurance).

Table 1. Summary of operating conditions for the NF-PRO experiments

Experiment	Fluid	Temp. (°C)	pH	Start Date	End Date	Exposure Time (days)
NFC1	0.01M NaCl	30	8.4	15/7/2005	21/3/2007	614
NFC4	"Allard"[1] Reference Groundwater	30	8.4	17/7/2005	21/3/2007	614
NFC7	1M NaCl	30	11	22/8/2005	10/7/2007	687
NFC13	1M NaCl	30	8.4	27/8/2005	21/3/2007	571

[1] Refer to Table 2 for "Allard" Reference Groundwater composition.

Samples of the residues from the experimental runs (Serco Assurance experiments NFC1, NFC4, NFC7 and NFC13) were selected by Serco Assurance. The vessels were opened and sampled within a nitrogen-purged glove-box to exclude oxygen. Samples were then taken from selected parts of each cylinder by cutting the soft bentonite with a sharp knife. These samples were then sealed into crimp-welded plastic bags (triple bagged), which were filled with oxygen-free nitrogen inside the glove-box. All sampling was carried out by Serco Assurance at Culham Laboratory, and the sealed sub-samples were then passed on to the BGS for mineralogical analysis. On receipt of the samples by the BGS, reference photographs were recorded of the reacted bentonite prior to further sampling and analysis.

Table 2. Composition of modified ”Allard” Reference Groundwater (from Vuorinen and Snellman, 1998)

	(mg/L)	(mmol/L)
Na^+	52.5	2.3
Ca^{2+}	5.1	0.13
Mg^{2+}	0.7	0.03
K^+	3.9	0.10
SiO_2	1.7	0.03
SO_4^{2-}	9.6	0.10
Cl^-	48.8	1.4
HCO_3^-	65.0	1.1

$pH_{\text{theoretical, log pCO2= -4}}$ 8.8

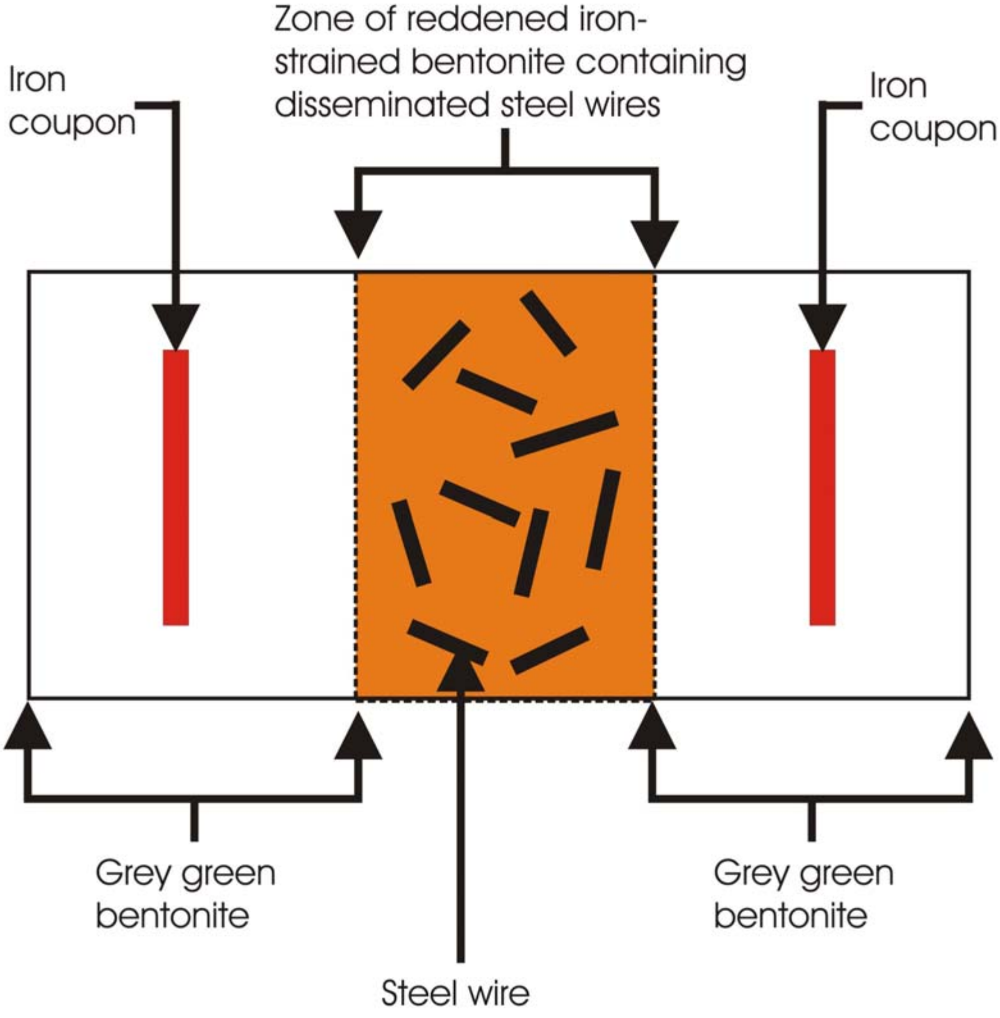

Figure 1. Schematic illustrating the different parts of the compacted bentonite-iron composite from the Serco Assurance NF-PRO experimental cells after reaction.

Table 3. Summary description of sub-samples examined from the NF-PRO experiments

SERCO Experiment	SERCO Sample Code	BGS Sample Code		Description	
NFC1	Sample 1 CELL 1	MPLM767	A	Block with the interface between red-brown bentonite (containing disseminated steel wires, and pervasively stained with corrosion products) and unaltered grey-green background bentonite. The opposite end of the sample contains the interface with the iron coupon.	Background fresh grey-green bentonite from edge of sample.
			B		Iron-stained bentonite matrix material from between corroded steel wires.
NFC4	Section 1 CELL 4 “steel side/ bentonite”	MPLM768		Largely fresh, grey-green bentonite, which at one end contains the interface with iron coupon that is surrounded by thin layer of iron-stained bentonite.	
	Section 1 CELL 4 “wire/ bentonite”	MPLM771		Block containing bentonite with disseminated steel wires, pervasively stained with corrosion products at one end. Opposite end is grey bentonite with surface stained impression of the interface with an iron coupon.	
NFC7	Section 1 CELL 7 “carbon steel surface”	MPLM769		Largely fresh, grey-green bentonite, which at one end contains the impression of a corroded iron coupon surround by thin layer of iron-stained bentonite.	
	Section 2 CELL 7 “wire/ bentonite”	MPLM772		Greenish-brown bentonite disc containing disseminated corroded steel wires on one side, with heavily iron-stained matrix	
NFC13	Section 1 CELL 13 “cell end section”	MPLM770		Disc of background unaltered grey-green bentonite from end of reaction cell	
	Section 2 CELL 13 “wire/ bentonite”	MPLM773	A	Bentonite block with steel wires, pervasively stained with brown corrosion products at one end. Opposite end is largely unaltered grey-green bentonite with the impression of an iron stained iron coupon.	Background fresh grey-green bentonite from edge of sample.
			B		Iron-stained bentonite matrix material between corroded wires.

The residues from all four experiments displayed obvious reddish-brown staining of the central region of the bentonite cylinder that was associated with the corrosion of the disseminated steel wires (cf. Figure 1). The iron coupons also showed some small-scale staining of the bentonite immediately in contact with the corroded metal. Since the focus of the BGS investigations was to investigate the potential alteration of the bentonite by interaction with iron corrosion products, sub-samples for detailed petrographical analysis were prepared from the central region of bentonite blocks containing disseminated steel wires, which visually displayed the greatest apparent alteration, and from the interface between the bentonite and the iron coupons). Sub-samples were selected for bulk mineralogical analysis and geochemical analyses from the iron stained bentonite matrix within the zone containing disseminated steel wires and from the adjacent unstained bentonite.

Since no unreacted MX-80 bentonite starting material was available for comparison, apparently unaltered compacted bentonite from the distal end of the cylinders from experiment NFC13 was examined to provide ‘background’ reference material for comparison with bentonite associated with iron and steel corrosion from the central region of the reacted bentonite cylinders. Details of the samples taken for analysis are summarised in Table 3.

3 Analytical methods

The sub-samples of reacted bentonite from NF-PRO experiments were provided by Serco Assurance in a moist state, and intended to be preserved within heat-sealed plastic bags filled with oxygen-free nitrogen. However, when inspected on receipt at the BGS, the heat-welded seals of the sample bags for NFC1, NFC 4 (both sub-samples), and NFC13 were found to have failed. All samples were opened and rapidly transferred to an Edwards Modulyo vacuum freeze drying unit, which was then immediately pumped down to vacuum to minimise exposure to air, thereby minimising the risk of oxidation of any ferrous iron phases. The samples were then left to dry for 72 hours under vacuum, after which they were stored under vacuum until required to be sub-sampled for analysis.

The total amount of material that was available from the experimental cells for mineralogical characterisation was very limited because of the need to undertake several types of analysis. In addition, because the intention was to examine mineralogical differences between sub-samples of the bentonite taken from different regions in the cells the mass of material that could be used for each analysis technique was further reduced.

3.1 PETROGRAPHICAL ANALYSIS

Petrographical analysis were focussed on observing the alteration characteristics and interaction of bentonite with iron corrosion products immediately adjacent to the corroding steel wires within the centre of the compacted bentonite-iron composite (Figure 1) used in the NF-PRO experiments. This region was characterised by zone of reddened iron-strained bentonite. Samples were then examined in polished thin section using backscattered scanning electron microscopy (BSEM), after initial examination by petrological microscope (in transmitted light). Image brightness in BSEM images is related to the average atomic number of the phases observed (Goldstein et al., 1981), and this therefore allows differentiation of the different minerals present. Element distributions in the bentonite matrix surrounding corroded steel wires were also studied by using digital energy-dispersive X-ray microanalysis (EDXA) elemental mapping.

3.1.1 Polished section preparation

Intact vacuum-dried fragments of this material, approximately 20 x 10 mm were impregnated with epoxy-resin under vacuum in order to stabilise the material for polished section preparation. These resin-impregnated blocks were then cut and polished under paraffin (to prevent reaction of the smectite with water-based cutting fluids) to produce polished thin sections 30 µm thick bonded onto 45 x 28 mm glass microscope slides with a colourless epoxy-resin. A blue dye was added to the epoxy-resin prior to vacuum impregnation to differentiate between porosity originally present within the vacuum-dried sample and artefacts of the sectioning process (e.g. grain plucking), when subsequently observed by transmitted-light microscopy. The sections were finished by polishing with 0.45 µm diamond paste.

3.1.2 Backscattered scanning electron microscopy

BSEM was carried out using a LEO 435VP variable pressure digital scanning electron microscope fitted with a solid-state 4-element (diode) backscattered electron detector, and equipped with an Oxford Instruments INCA EDXA system with a thin window Si-Li X-ray detector capable of detecting elements from boron to uranium. The scanning electron microscope instrument was operated in the conventional high vacuum mode ($<1 \times 10^{-4}$ torr), using a 10-20 kV electron beam accelerating potential, beam currents between 200-800 pA, and a working distance of 17-20 mm, as required. Phase identification was aided by microchemical information obtained from observation of semi-quantitative EDXA spectra recorded from features of interest. Digital EDXA X-ray element maps were recorded from selected areas of interest, using a 20 kV electron beam, 200-400 pA beam currents and at a working distance of 19 mm. EDXA spectra and digital X-ray elemental maps were processed using the INCA Suite Version 4.08 (2006) software package. X-ray element maps were typically produced by summation of data recorded from 30-100 frame scans recorded over 45-120 minutes. Images were processed to show relative element concentrations using a 'rainbow colour scale' ranging from blue (representing zero background) through green, yellow and orange (low to intermediate concentration) to high red or white (representing high concentration).

X-ray elemental maps were recorded at a resolution of 1024 x 768 pixels for:

- C and Cl, which indicate where epoxy-resin impregnates the samples. Cl might also show where residual sodium chloride pore fluid has deposited salt upon sample drying;
- Si, Al, and Mg, which would be derived from the silicate mineral assemblage of the bentonite. Mg might also be present within the exchangeable cation sites in the smectite or might also be derived from the modified "Allard" reference groundwater used in Experiment NFC4 (Table 2).
- Na, K, and Ca, which might be derived from the exchangeable cation component of the smectite clay mineral that dominates the bentonite. K and Na would also be recorded from minor amounts of K-feldspar, albite and zeolites, and Ca from minor calcite that may also be present in the bentonite. Na concentration could also be indicative of salt deposited from drying of any residual saline pore fluid. K and Ca might also be derived from residual salts or reaction products formed by interaction with the "Allard" reference groundwater used in the case of Experiment NFC4 (Table 2);
- Fe maps primarily record the location of the steel wires and any Fe-rich alteration products. Accessory Fe-bearing minerals such as pyrite and natural iron oxides (ilmenite, magnetite) would also be shown in the Fe maps.
- Maps for P and Mn were also recorded.

Quantitative elemental profiles were estimated from the X-ray elemental maps, using the steel to provide an internal reference against which the concentrations could be normalised. The profiles were selected to examine the variation in element concentration away from the margin of the corroding steel wire or iron coupon into the adjacent bentonite matrix. Although microchemical data were recorded for every pixel, the elemental line profile data were smoothed using a 25-pixel sliding average in order to reduce the noise from the background heterogeneity of the bentonite matrix.

3.2 X-RAY DIFFRACTION ANALYSIS

3.2.1 Sample preparation

Due to the very small size of the sample material available for analysis from the experiments and nature of the regions of the samples to be analysed, 'zero-background' silicon crystal substrate X-ray diffraction (XRD) mounts were used rather than the standard cavity XRD sample holders or ceramic tiles which require greater volumes of sample.

Firstly, in order to study the mineralogy of the samples as supplied and to prevent further oxidation of any Fe-bearing species, small (typically c.10 mg) portions of material were rapidly removed using a scalpel. Any steel wire remaining in these sub-samples was removed using a hand magnet before grinding the material to a fine powder in an agate pestle and mortar. The powder was then deposited onto the surface of the silicon crystal substrate using a single drop of acetone to form a random orientation. Such analyses were carried out to determine the nature of any non-clay minerals present in the samples and also to determine the d_{060} spacing of any clay minerals present.

Secondly, the clay mineral assemblages of the samples were studied by preparing oriented mounts. Typically, such analyses would be initiated by the isolation of a fine, <2 µm size fraction to increase the concentration of clay minerals. However in this case, clay minerals form >75% of the MX-80 bentonite starting material (Madsen, 1998) and therefore any such concentration is unnecessary. In addition, size separation of sodium bentonites is typically difficult as they form colloidal gels in water. Any requirement for the addition of a dispersing agent (typically sodium hexametaphosphate, 'Calgon') would also alter the exchangeable cation chemistry of the bentonite and its XRD characteristics. Therefore in this study, material for oriented XRD mounts was prepared by further dispersing small (typically c.10 mg) portions of material in deionised water using ultrasound treatment and no dispersant was added. The dispersions were then pipetted onto 'zero-background' silicon crystal substrates and allowed to dry at room temperature.

3.2.2 Analysis

XRD analysis was carried out using a PANalytical X'Pert Pro series diffractometer equipped with a cobalt-target tube, X'Celerator detector and operated at 45 kV and 40 mA.

The random powder mounts were scanned from 4.5-85 °2θ at 2.76 °2θ/minute. Diffraction data were initially analysed using PANalytical X'Pert Highscore Plus version 2.2a software coupled to the latest version of the International Centre for Diffraction Data (ICDD) database.

The oriented mounts were scanned from 2-40 °2θ at 1 °2θ/minute after air-drying, after glycol-solvation and after heating to 550 °C for 2 hours.

3.2.3 Clay mineral modelling

In order to gain further information about the nature of the clay minerals present in the samples, modelling of the XRD profiles was carried out using Newmod-for-Windows™ (Reynolds and Reynolds, 1996) software. Modelling was also used to assess the relative proportions of clay minerals present by comparison of sample XRD traces with Newmod-for-Windows™ modelled profiles. The modelling process requires the input of diffractometer scan parameters and a quartz intensity factor (instrumental conditions), and the selection of different sheet compositions and chemistries. In addition, an estimate of the crystallite size distribution of the species may be determined by comparing peak profiles of calculated diffraction profiles with experimental data. By modelling the individual clay mineral species in this way, mineral *'reference intensities'* were established and used for quantitative standardization following the method outlined in Moore and Reynolds (1997).

3.3 CATION EXCHANGE CAPACITY AND EXCHANGEABLE CATION ANALYSIS

The cation exchange capacity (CEC) was determined using the technique based on the compulsive exchange between an aqueous solution of magnesium sulphate and a barium soil (Bascomb, 1964). This method is routinely used in the analysis of rocks and soils for environmental assessment (Gillespie et al., 2000a,b, 2001). The samples were shaken with two separate portions of barium chloride solution, buffered at pH 8.1 with triethanolamine, and then washed with water to remove any excess barium chloride. Magnesium sulphate solution was then added to the barium-saturated materials to displace the barium, which was precipitated as insoluble barium sulphate. The amount of magnesium exchanged was then determined by titrating the excess magnesium sulphate with EDTA.

Exchangeable cations were determined on the $BaCl_2$/triethanolamine extractant by inductively-coupled plasma – atomic emission spectroscopy (ICP-AES), and checked against matrix matched standards. The cation species determined by ICP-AES included Ca, Mg, Mn, Na, K and Fe.

3.4 X-RAY FLUORESCENCE ANALYSIS

X-ray fluorescence (XRFS) analysis was carried out to examine the variations in bulk major element chemical composition of the bentonite adjacent to and distant from the corroding steel wires in NF-PRO experiments NFC1 (BGS sub-samples MPLM767A and MPLM767B), NFC4 (BGS sub-sample MPLM771) and NFC13 (BGS sub-samples MPLM770, MPLM773A and MPLM773B). The details of the sub-samples are given in Table 3 and the analyses are presented in Appendix 1.

XRFS analysis was performed by wavelength-dispersive spectrometry, using the samples prepared as fused glass beads. The sample was dried overnight at 105 °C before LOI and pre-ignited at 1050°C before analysis by XRFS. Major elements determined included SiO_2, TiO_2, Al_2O_3, Fe_2O_3(t), Mn_3O_4, MgO, CaO, Na_2O, K_2O and P_2O_5. In addition, minor elements Cr_2O_3, SrO, ZrO_2, BaO, NiO, CuO, ZnO, PbO and SO_3 were also determined. Loss on ignition was determined after 1 hour at 1050 °C. Fe_2O_3(t) represents total iron expressed as Fe_2O_3. SO_3 represents sulphur retained in the fused bead after fusion at 1200 °C. The sum of the major oxides in sample MPLM770 failed one of the routine quality control (QC) criteria (total >99%) but passed all other QC criteria. Dark flecks were visible in cast beads made from samples MPLM767B, MPLM771 and MPLM773A; the presence of these flecks did not appear to have any effect of the totals oxide content. Reanalysis of these four samples could not be carried out because there was insufficient material left after the first analysis.

3.5 SEQUENTIAL CHEMICAL EXTRACTION ANALYSIS

As in the Phase 1 study (Milodowski et al., 2007), the chemical partitioning of iron between the different ‘mineral phases’ in the reacted bentonite was explored further by using sequential chemical extraction. Three samples of bentonite, heavily stained with red-brown iron alteration products taken from immediately adjacent to the corroding steel wires in NF-PRO Experiment NFC1 (BGS sub-sample MPLM767), NFC4 (BGS sub-sample MPLM771) and NFC13 (BGS sub-sample MPLM773), together with unaltered bentonite taken from the end of the reaction cell in NFC13 (BGS sub-sample MPLM770), were studied. The sequential extraction methodology used was the ‘Chemometric Identification of Mineral Substrates and Element Distributions (CISED) Test’ (Cave et al. 2004), which is based on the chemometric data interpretation of a series of 14 solutions (involving 2 replicates for each of 7 leachant stages) derived from the extraction of solutes using separate aliquots of Aqua Regia of increasing concentration (Table 4).

3.5.1 Extraction procedure

To obtain the CISED extracts, approximately 0.2 g of bentonite was accurately weighed into 8 ml Sterilin containers and 4 ml of the starting leachant (de-ionised water) was added. The container was mounted on an end-over-end tumbler for 5-10 minutes, allowing the leachant and the bentonite to mix. The unit was then centrifuged for 5 minutes, or until separated, at 3000 rpm. The surface leachate collected was then removed using a pipette for analysis by ICP-AES, before the next leachant was added and the process was repeated. The sequence of leachants used is summarised in Table 4.

To obtain the total major and trace cation contents for comparison with the CISED extraction data, a 0.1 g portion of each sample was digested in PTFE tubes with a mixture of hydrofluoric, perchloric and nitric acids. In addition, 0.1, 0.2, 0.3 and 0.4 ml, respectively, of hydrogen peroxide were added to leachates G/H, I/J, K/L and M/N (Table 4) before making up to volume.

Table 4. Summary details of the sequential extraction leachants used in the CISED test

Leachate Fraction No.	Leachant solution
A/B	De-ionised water
C/D	0.01 M Aqua Regia
E/F	0.05 M Aqua Regia
G/H	0.1 M Aqua Regia
I/J	0.5 M Aqua Regia
K/L	1 M Aqua Regia
M/N	5 M Aqua Regia

3.5.2 Chemical analysis

All extracts were analysed by ICP-AES at dilutions made to volume using 1% HNO_3 except the A and B extracts for which dilutions were made using deionised water. Stable colloidal or precipitated material was observed in many of the extracts at analysis; care was taken not to disturb this material during analysis. Detectable concentrations of some determinands were found in the procedural blank performed with the extractions, specifically Al, Fe, Total P and Zn. Data have not been corrected for these blank concentrations.

4 Results

4.1 PETROGRAPHICAL OBSERVATIONS

4.1.1 Experiment NFC1

4.1.1.1 General observations

The small sample provided by SERCO Assurance from the cylinder of compacted bentonite recovered from Experiment NFC1 displayed visually-similar alteration characteristics to that seen in the experimental residue materials examined previously by Milodowski et al. (2007).

One end of the sample was defined by an interface between bentonite and a corroded iron coupon (Figure 2a). It was evident that the bentonite was stained by orange iron oxidation products within a narrow zone up to 4 mm wide around the edges of the impression left by the iron coupon (the coupon was not included in the sample provided to the BGS). However, most of the 'iron staining' in the bentonite was seen to be limited to within 1-2 mm of the face of the iron coupon.

Significant alteration and reaction had occurred within the central region containing the dispersed steel wires, as evident from the very strong red-brown staining of the bentonite within this region (Figure 2b,c). The iron-stained central region extended to about 5 mm from the margins of the zone containing the steel wires (Figure 2b). Much of the reddish brown ferruginous staining was developed along a 'chicken wire mesh-like' network of interconnected hairline fractures within this central region, with extensive diffusive impregnation of the discolouration into the adjacent bentonite matrix.

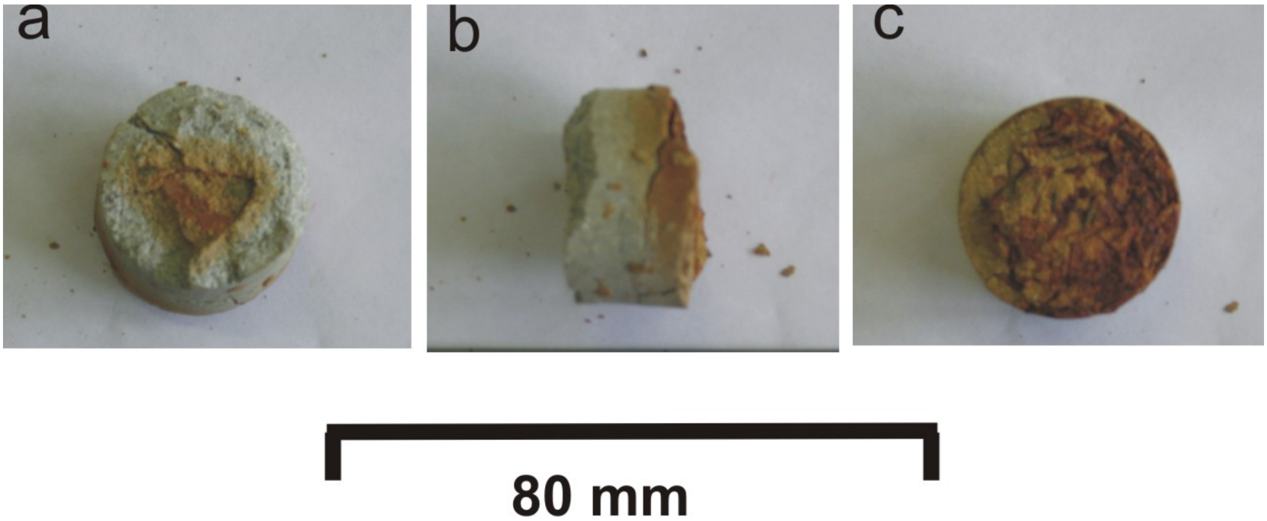

Figure 2. Photograph of bentonite block from NF-PRO-Experiment NFC1, Serco Assurance Sample 1, Cell 1 (BGS sample MPLM767): (a) end-face containing ferruginous staining and impression from corroded iron coupon; (b) interface between heavily iron-stained zone and unaltered bentonite; (c) end-face exposing corroded steel wires surrounded by halos of red-brown iron oxide and iron oxide-stained bentonite

Close examination of freshly broken fragments (after vacuum drying) taken from the zone of corroded wires in the bentonite cylinder showed that the surfaces of the steel wires were coated with a very thin film of very dark brown to black oxide corrosion product, surrounded by a halo of dark reddish-brown colouration of the adjacent bentonite that becomes a more diffuse and lighter orange to light reddish brown stain in the bentonite matrix beyond about 0.1-0.5 mm distance from the wire surface. Fragments of the dark brown to black oxide corrosion product were found to be ferromagnetic and could be attracted to a strong hand magnet. This suggests that the corrosion products possibly include magnetite (Fe_3O_4) or maghemite (γ-Fe_2O_3).

As in the previous study (Milodowski et al., 2007) it was noticeable that the shrinkage behaviour of the bentonite matrix on drying was different between the heavy iron-stained central part of the steel wire-bearing region and the margins of the bentonite that were free of steel wires. The heavily iron-impregnated areas from the centre of the zone with abundant corroded steel wire displayed much less shrinkage and cracking after vacuum-drying than the margins of the zone that were free of corroded steel wires.

4.1.1.2 DETAILED PETROGRAPHY

BSEM petrographical analysis of the polished thin section, prepared through the zone of bentonite containing disseminated steel wires, indicates that there has been significant reaction and corrosion of the steel wires, with the formation of a halo of alteration in the enclosing bentonite (e.g. Figure 3, Figure 4 and Figure 5). This alteration halo shows up brighter than the background bentonite due to an enhanced concentration of Fe, as a result of which, it has a higher average atomic number and a much higher backscattered electron coefficient (i.e. it is more ‘reflective’ to electrons) than the Na-Si-Al-dominated matrix of the unaltered bentonite.

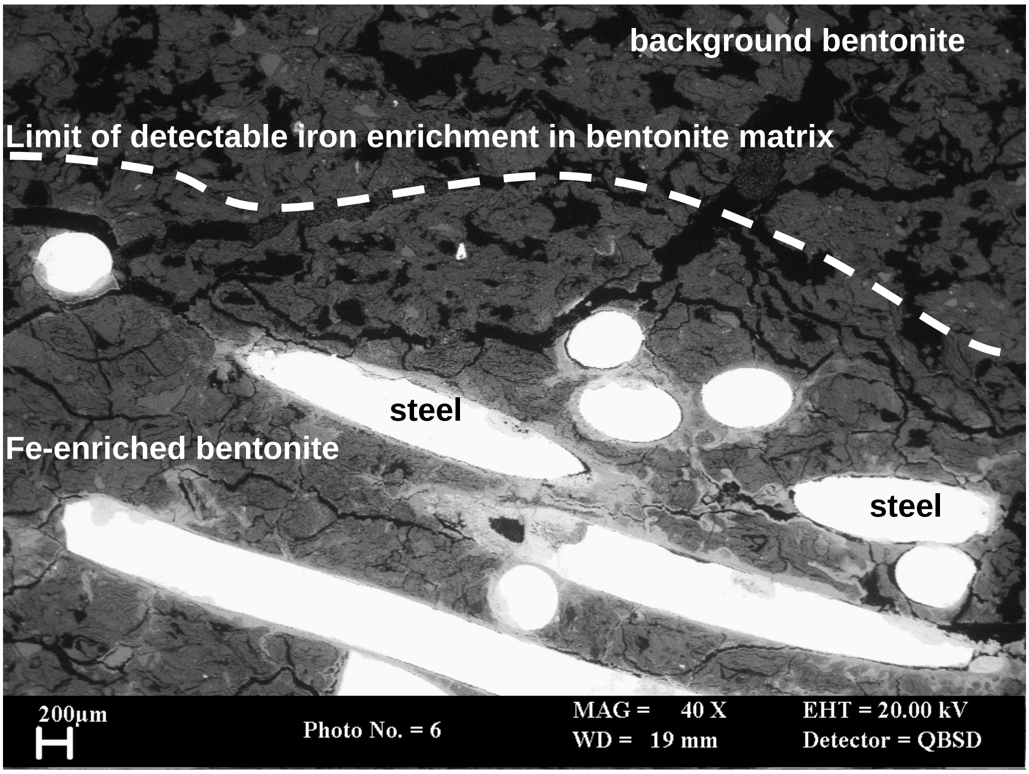

Figure 3. BSEM photomicrograph showing the boundary between the zone of bentonite containing disseminated steel wires and background bentonite. The bentonite adjacent to the corroding steel wires shows significant enrichment (appears brighter under BSEM). NF-PRO-Experiment NFC1 (Serco Assurance Sample 1, Cell 1 – BGS sample MPLM767)

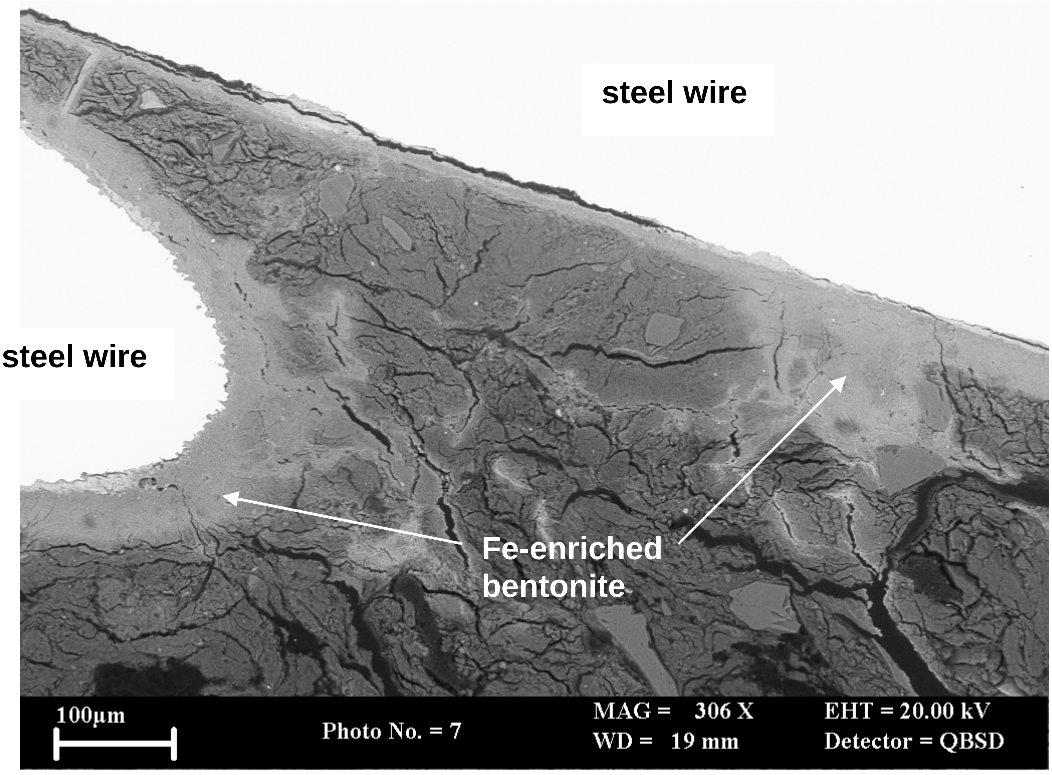

Figure 4 BSEM photomicrograph showing narrow zone of altered bentonite (brighter) in contact with corroded steel wires. The alteration is associated with significant enrichment of Fe. The altered bentonite is cut by numerous open microfractures, which display enhanced Fe (brighter) in their bentonite walls. NF-PRO-Experiment NFC1 (Serco Assurance Sample 1, Cell 1 – BGS sample MPLM767)

EDXA microchemical mapping clearly shows that the bentonite adjacent to the corroded steel wires is enriched in Fe (Figure 5, Figure 6 and Figure 7). The halo of altered bentonite around the corroded steel wires was observed to be generally between 50-300 µm thick but Fe-enrichment in the bentonite was detectable by BSEM-EDXA to about 1.5 mm from the zone of corroding steel wires in some cases (Figure 3). The greatest apparent alteration and highest concentration of Fe is seen in the bentonite matrix between corroded steel wires within the core region of the interval of bentonite-with-disseminated steel wires. In comparison, the alteration zones around steel wires at the margins of the interval were observed to be much narrower (cf. Figure 3 and Figure 5).

Figure 7 shows a typical Fe concentration profile in the bentonite around a corroding wire. Immediately adjacent to the corroded metal surface Fe concentrations were observed to be up to 80 wt.%, decreasing to about 70 wt.% at about 40 µm from the steel. Within this narrow region the alteration halo must therefore consist mainly of iron oxides (cf. wustite (FeO) contains 77.7 wt. % Fe) magnetite (Fe_3O_4) contains 72.4 wt.% Fe and hematite (Fe_2O_3) contains 69.9 wt. % Fe). Petrographical analysis confirms that abundant discrete iron oxide has formed immediately against the steel within this interval, displacing the bentonite and penetrating the adjacent bentonite along grain boundaries and microfractures (Figure 8). Between 40 and 100 µm distance, the Fe concentration decreases rapidly to about 25 wt.% Fe, thereafter decreasing less rapidly to a concentration close to that expected for background unaltered bentonite (average 2.83 wt. % Fe from data in Appendix 1) at a distance of between 600-1000 µm from the metal. The amount of Fe present within this altered zone is much greater than can be accounted for by Fe in exchangeable cation sites. BSEM-EDXA reveals that some Fe is present as discrete very fine Fe oxide (Figure 8). However, the very fine smectitic matrix also appears to be significantly enriched in Fe (it has a much higher backscattered electron coefficient

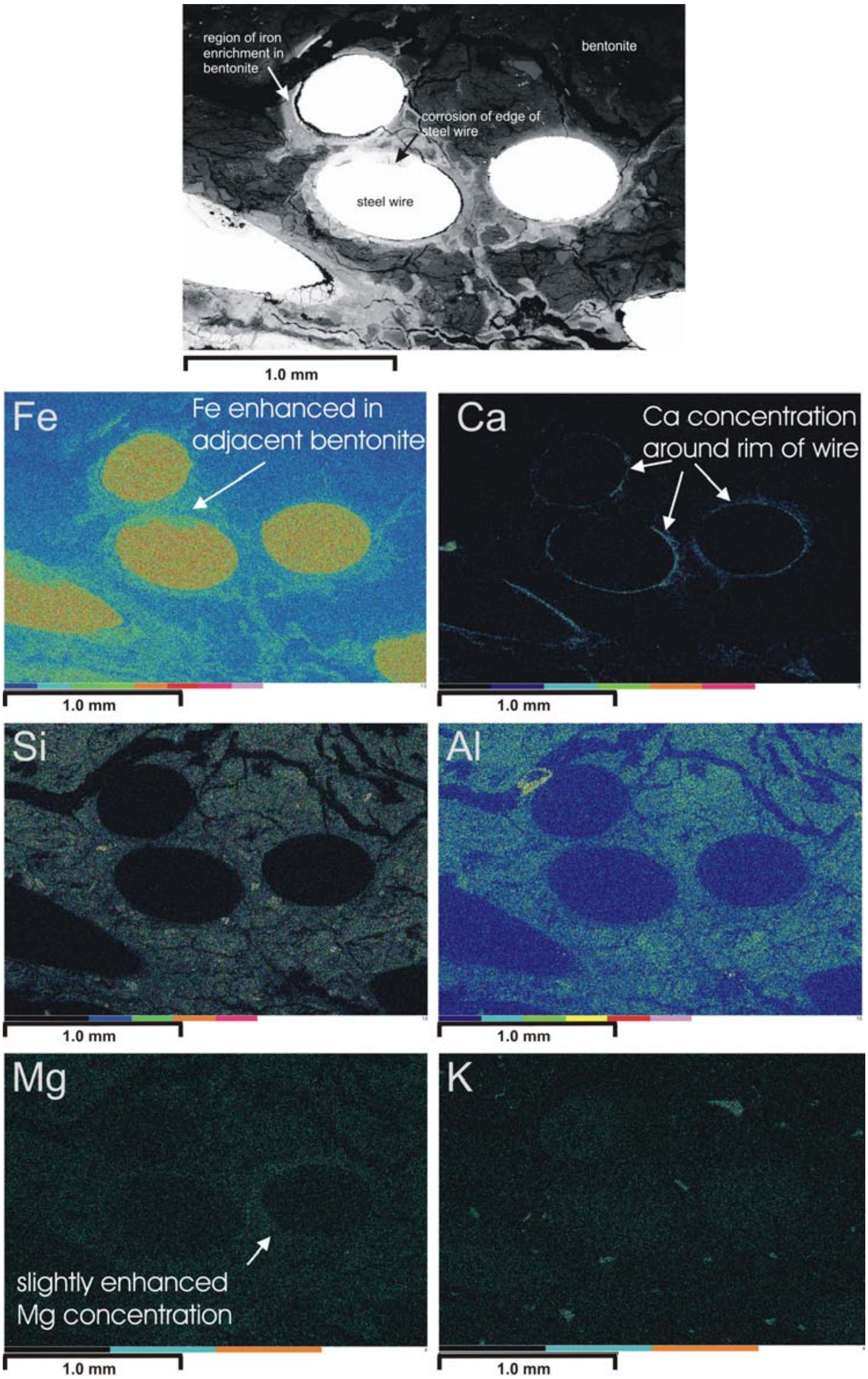

Figure 5. BSEM photomicrograph (top) with corresponding EXDA maps for Fe, Ca, Si, Al, Mg and K distributions in bentonite around a corroding steel wire. Fe and Ca display enhanced concentrations in the bentonite close to the corroding steel wire, with Fe enrichment along a network of microfractures in the bentonite matrix; Si and Al display little change or only slight depletion relative to background bentonite; Mg possibly displays a very slight enhancement in the bentonite close to corroding steel; K distribution is unaffected by corroding metal and shows only relatively high local concentrations corresponding K-feldspar fragments in the bentonite. NF-PRO-Experiment NFC1 (Serco Assurance Sample 1, Cell 1 – BGS sample MPLM767)

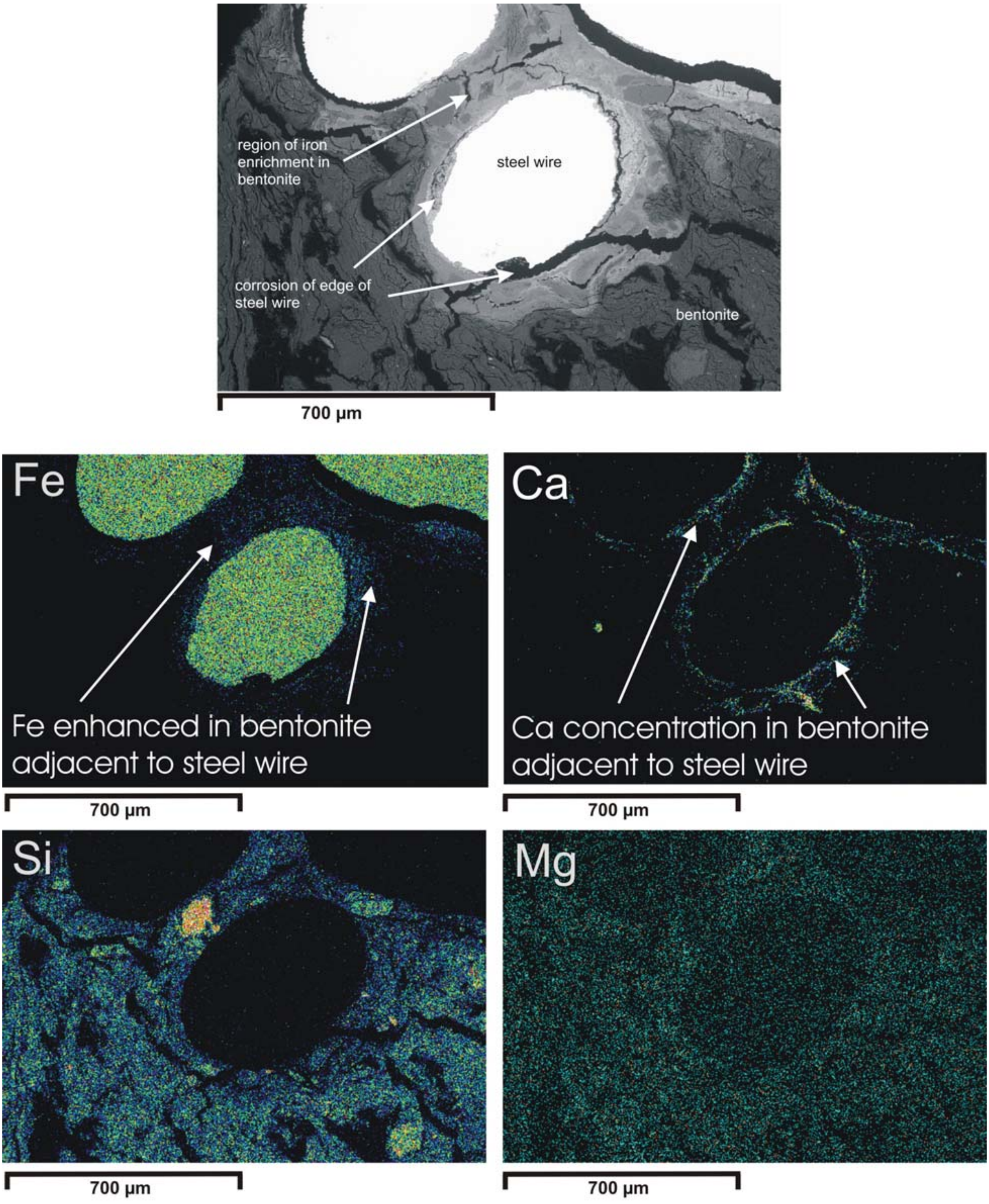

Figure 6. BSEM photomicrograph (top) with corresponding EXDA maps for Fe, Ca, Si and Mg distributions in bentonite around a corroding steel wire. Fe and Ca display enhanced concentrations in the bentonite close to the corroding steel wire; Si is slightly depleted relative to background bentonite; Mg possibly displays a very slight enhancement in the bentonite close to corroding steel. NF-PRO-Experiment NFC1 (Serco Assurance Sample 1, Cell 1 – BGS sample MPLM767)

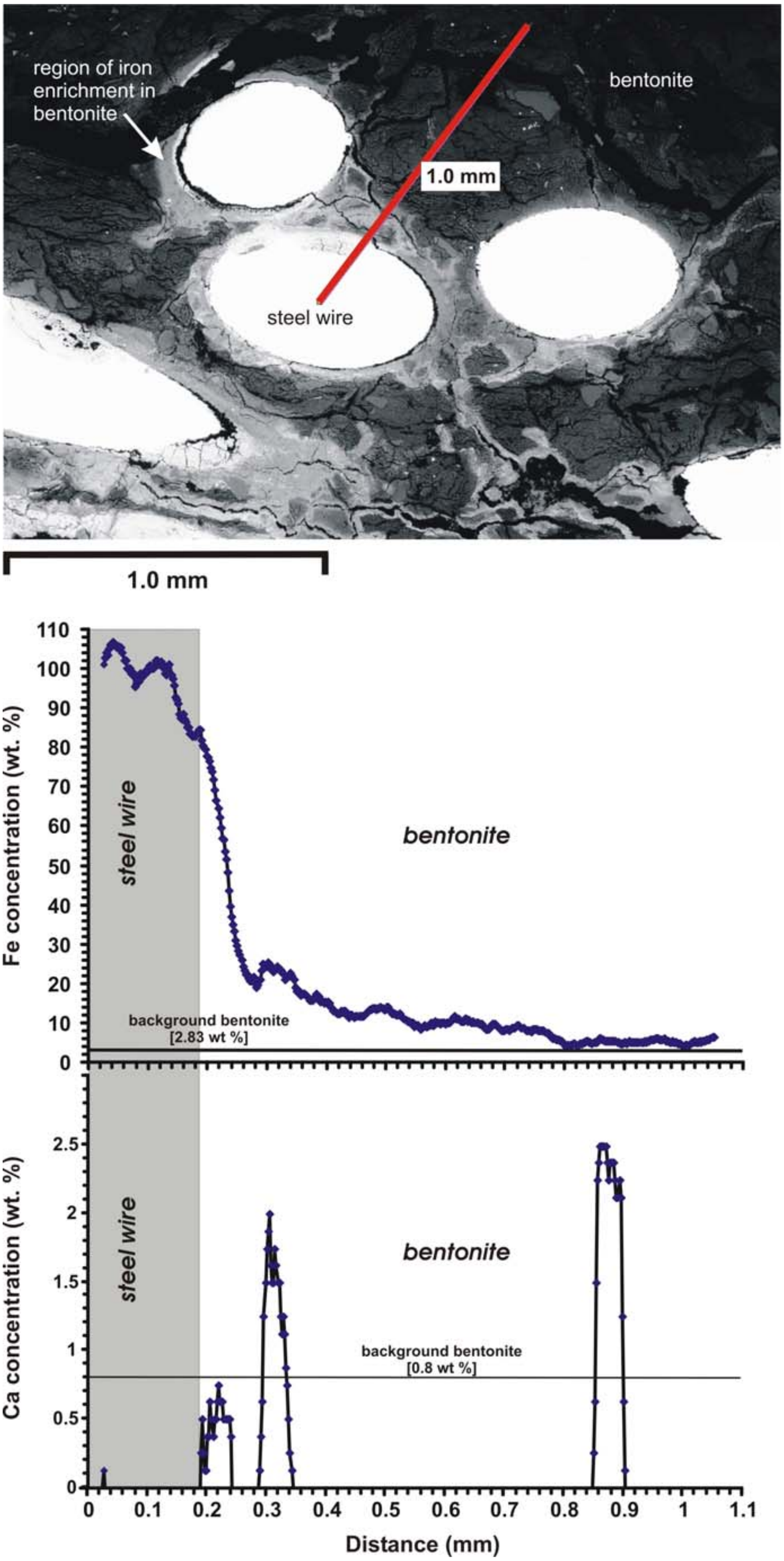

Figure 7. EDXA concentration profiles for Fe and Ca in bentonite with distance from corroding steel wire. Line of profile shown in BSEM photomicrograph (top). NF-PRO-Experiment NFC1 (Serco Assurance Sample 1, Cell 1 – BGS sample MPLM767)

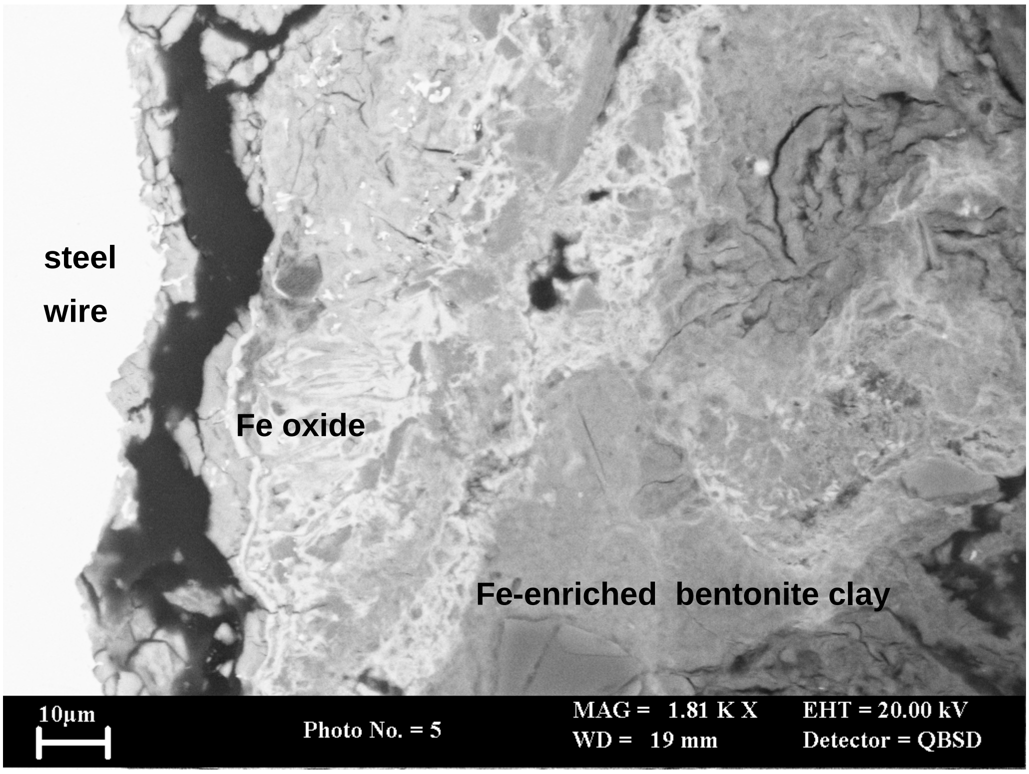

Figure 8. BSEM photomicrograph showing colloform and gel-like dense iron oxide alteration products (bright) formed immediately adjacent to the corroding steel wire, and penetrating into the smectitic clay matrix along grain boundaries (grey). NF-PRO-Experiment NFC1 (Serco Assurance Sample 1, Cell 1 – BGS sample MPLM767)

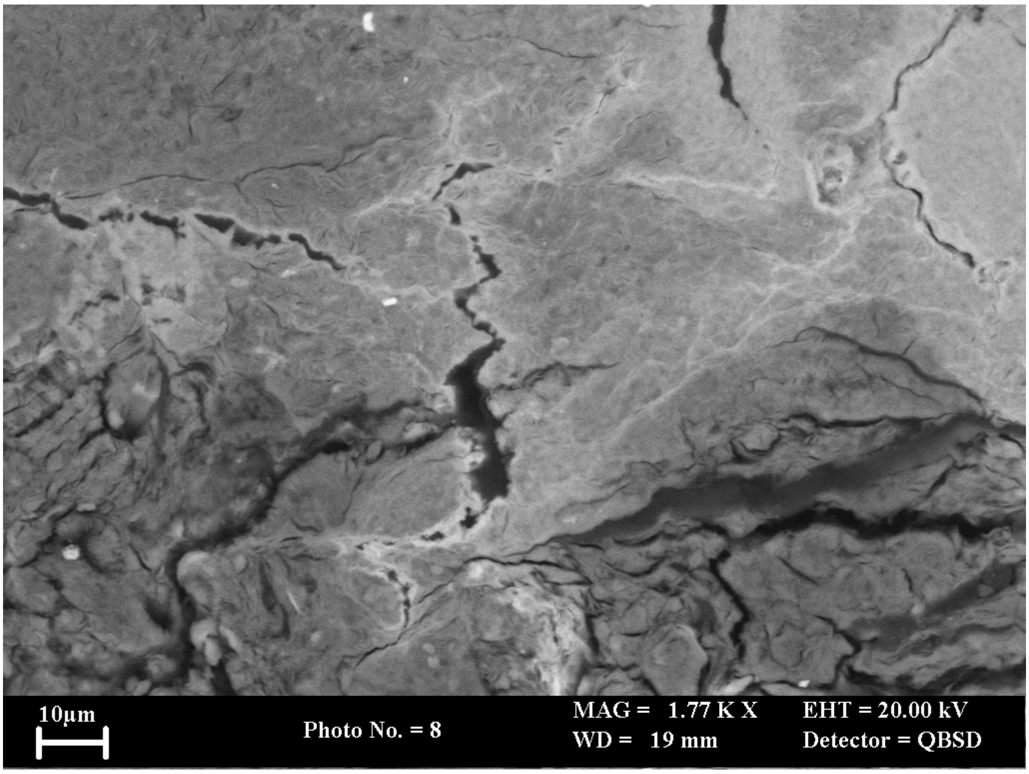

Figure 9. BSEM photomicrograph showing open microfractures are lined by fine iron oxide (white). The adjacent bentonite in the fracture walls is brighter due to higher Fe concentration. NF-PRO-Experiment NFC1 (Serco Assurance Sample 1, Cell 1 – BGS sample MPLM767)

than unaltered silicate matrix), with no discrete iron oxides resolvable by BSEM-EDXA. In this case, it would appear that at least part of the Fe has been incorporated within the silicate clay mineral, at least at the scale of resolution of these petrographical observations.

High concentrations of Fe were also observed in the bentonite immediately adjacent to irregular open microfractures radiating from around each of the altered wires (e.g. Figure 5 and Figure 9). These microfractures penetrated the bentonite matrix for up to 1 mm from the wire surface around some of the wires. In this section, the fractures had apertures from < 1 μm up to about 10 μm, although this was probably accentuated by shrinkage of the smectitic clay during sample drying and impregnation with epoxy-resin. Detailed BSEM-EDXA observations showed that the fracture surfaces were coated with a thin film (typically ≤ 1 μm) (Figure 9). Some of the finer fractures were filled with fine iron oxides (Figure 10). Close examination also revealed that clay mineral matrix adjacent to these iron-oxide mineralised fractures also has a high concentration of Fe. BSEM shows that the very fine platy clay mineral particles within this altered clay matrix appear to have a much higher backscattered electron coefficient (appear brighter – cf. Figure 10). This suggests, within the limits of resolution of the BSEM technique (probably better than 0.1 μm) that the clay mineral (smectite) particles themselves have become enriched in Fe within the alteration haloes.

Although, the apertures of these fractures may have been accentuated by shrinkage of the smectite during sample drying and subsequent resin impregnation during thin section preparation, the fact that they are mineralised with iron oxides and show significant enrichment of Fe in the smectite forming the fracture walls clearly demonstrates that the fractures must have formed during the course of the experiment.

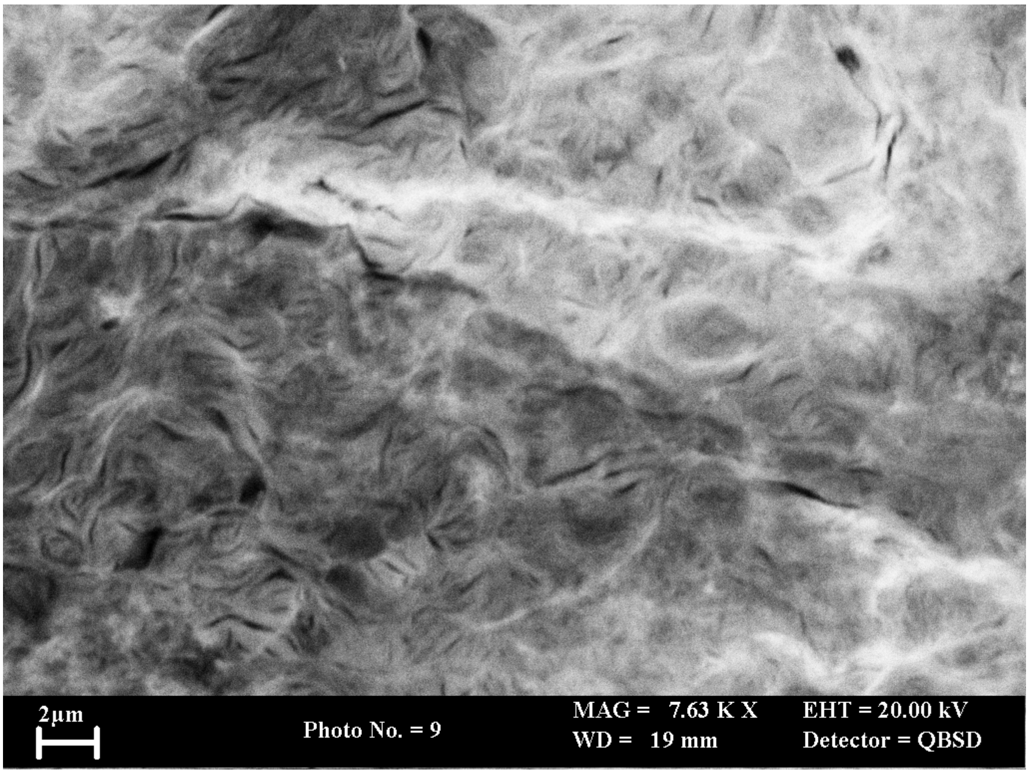

Figure 10. BSEM photomicrograph showing detail of clay matrix fabric within the narrow zone of altered bentonite (brighter) surrounding corroded steel wire. A microfracture can be seen filled with fine grained iron oxide (white). The wispy or micaceous clay mineral particles in the bentonite matrix display brighter surfaces due to Fe enrichment or uptake along basal [001] surfaces and cleavage planes. NF-PRO-Experiment NFC1 (Serco Assurance Sample 1, Cell 1 – BGS sample MPLM767)

EDXA microchemical mapping also showed that Ca had also been concentrated within a narrow zone in the altered bentonite close to the corroding steel wires (Figure 5, Figure 6 and Figure 11). Similar effects were observed in the reacted bentonite from the earlier NF-PRO experiments studied previously by Milodowski et al. (2007). Chemical distribution profiles (e.g. Figure 7) and EDXA element maps (Figure 11) show that the Ca enrichment occurs as a series of bands within the zone of Fe-enrichment, between 0 to 1000 µm from the corroding metal. Close petrographical observations show that the Ca tends to be concentrated as a series of “fronts” developed at the leading edge of “fronts” of iron concentration moving from the steel surface into the bentonite (Figure 11).

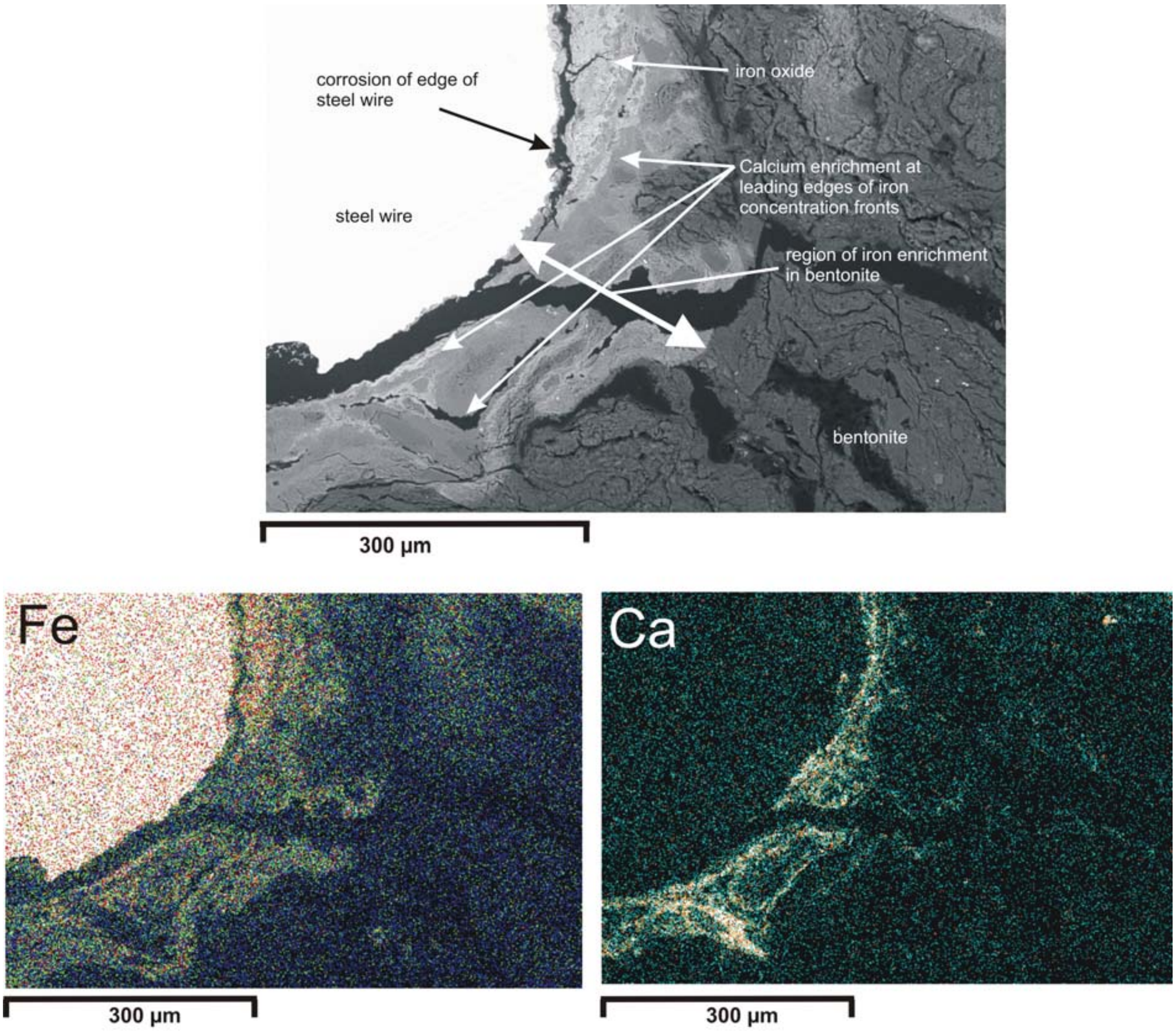

Figure 11. BSEM photomicrograph (top) with corresponding EXDA maps for Fe and Ca distributions in bentonite around a corroding steel wire, showing Ca and Fe concentration fronts. NF-PRO-Experiment NFC1 (Serco Assurance Sample 1, Cell 1 – BGS sample MPLM767)

C concentrations coincide with the accumulation of Ca, suggesting that this reaction product may be a calcium carbonate phase, although it is often difficult to discriminate C in this Ca-rich alteration phase from the C present in the epoxy-resin used in making the polished thin sections. Detailed BSEM observation revealed that this Ca-rich phase occurs as fine acicular (needle-like) crystals (up to 10 µm long) precipitated on the walls of cavities within open microfractures around the margins of the corroded steel and in microfractures radiating away from the corroding wires. In addition, similar, fine-grained acicular Ca-rich material is seen nucleated within, or replacing, the Fe-impregnated bentonite immediately adjacent to the iron oxide corrosion layer. It seems most likely that this neoformed Ca-phase corresponds to the aragonite that was identified from the altered bentonite by XRD (Section 4.2.2).

Other chemical changes associated with the metal corrosion were also observed. EDXA maps often show a slight depletion in Si and Al within the clay matrix of bentonite alteration haloes. This does not necessarily indicate that Si and Al have migrated away from the alteration zone. Rather, it may largely reflect the effective dilution of Si and Al in the silicate mineral matrix by secondary iron oxide precipitates and the addition of Fe from the corroding metal. Some microchemical maps tentatively indicate a slight enrichment of Mg within the clay matrix in the alteration halos around the steel wires (Figure 6). However, any enhancement in Mg is very small, and in most cases it is barely perceptible above the background heterogeneity observed in the unaltered bentonite. No discernable variations were observed in the distribution P, Mn, Na and K between altered and unaltered bentonite. The distribution of K largely highlighted the presence of disseminated grains of mica and K-feldspar. P and Mn were largely below detection (likely to be of the order of 0.25-0.5 wt.% under the operating conditions used), except where detectable concentration coincided with traces of primary apatite and ilmenite in the bentonite.

The surfaces of the steel wires were observed to be pitted and etched, with thin concentric bands of very fine grained secondary iron oxide or iron oxyhydroxide coating the corroded metal surface. This secondary iron oxide alteration either forms a structureless coating filling corrosion pits or appears to be highly microporous. The corrosion pits on some wires were seen locally to penetrate up to 100 µm deep into the metal, but in most cases the corrosion pitting is around 10-20 µm deep. The corrosion is often asymmetric, with one side of the wire preferentially corroded. Generally the thickness of the alteration halo around the corroded wire is greatest adjacent to where the wire is most extensively corroded.

4.1.2 Experiment NFC4

4.1.2.1 GENERAL OBSERVATIONS

The two small samples provided by SERCO Assurance from the cylinder of compacted bentonite recovered from Experiment NFC4 (Section 1 Cell 4 “steel side/bentonite” – BGS sample MPLM768, and Section 1 Cell 4 “wire/bentonite”) represent material from the interface between a iron coupon and bentonite, and material from the edge of the central interval of bentonite containing disseminated steel wires, respectively. Both samples displayed visually-similar alteration characteristics to that seen in the experimental residue from NF-PRO Experiment NFC1 (Section 4.1.1.1) and materials examined previously by Milodowski et al. (2007).

One face of the sample Section 1 Cell 4 “steel side/bentonite” (MPKM768) was defined by the interface between bentonite and a corroded iron coupon (Figure 12: top a). It was evident that the bentonite was stained by orange iron oxidation products within a narrow zone, 2 to 4 mm wide, around the edges of the metal (Figure 12: top b).

Significant alteration and reaction was evident in sample Section 1 Cell 4 “wire/bentonite”(MPLM771). The central region containing the dispersed steel wires displayed very strong red-brown staining of the bentonite within this region (Figure 12: bottom c). The iron-stained central region associated with the corroded steel wires extended to about 5 mm from the margins of the zone containing the steel wires (Figure 12: bottom b). Much of the reddish brown ferruginous staining was developed along a fine, ‘chicken wire mesh-like’ network of interconnected hairline fractures within this central region, with extensive diffusive impregnation of the discolouration into the adjacent bentonite matrix. The opposite face of the sample corresponded to the interface between an iron coupon and bentonite, and displayed an iron oxide-stained impression of the surface of the iron coupon (not present in this sample).

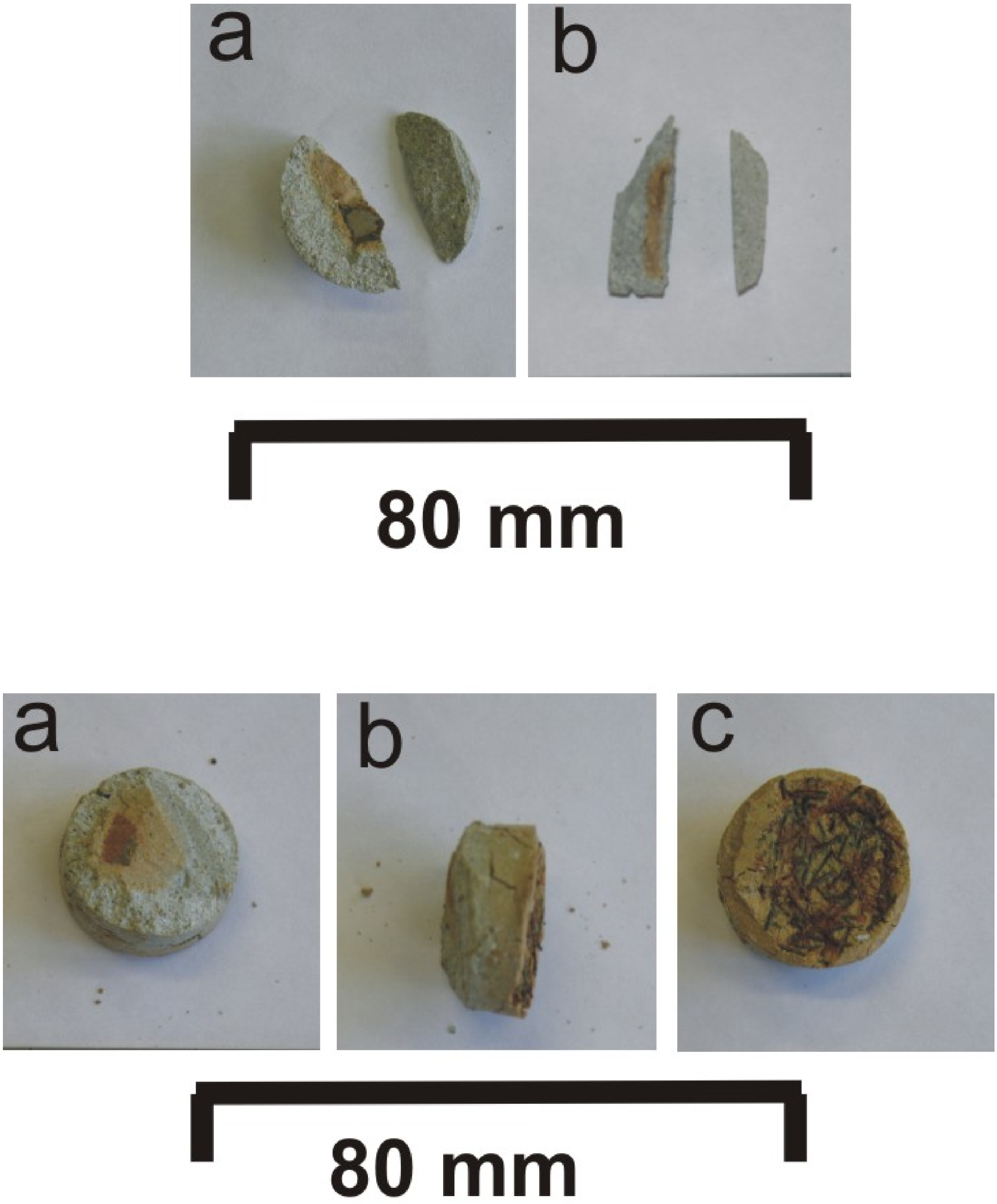

Figure 12. Photograph of bentonite samples from NF-PRO-Experiment NFC1. Top: Serco Assurance Section 1 "steel side/bentonite", Cell 4 (BGS sample MPLM768): (a) end-face containing ferruginous staining around a corroded iron coupon; (b) fractured perpendicular to axis showing the bentonite and the iron coupon surrounded by iron stained halo. Bottom: Serco Assurance Section 1, Cell 4 "wire/bentonite", (BGS sample MPLM771): (a) end-face containing ferruginous staining and impression from corroded iron coupon; (b) interface between heavily iron-stained zone and unaltered bentonite; (c) end-face exposing corroded steel wires surrounded by halos of red-brown iron oxide and iron oxide-stained bentonite

Close examination of freshly broken fragments (after vacuum drying) taken from the corroded steel wire zone region of the bentonite cylinder showed that the surfaces of the steel wires were coated with a very thin film of very dark brown to black oxide corrosion product, surrounded by a halo of dark reddish-brown colouration of the adjacent bentonite that becomes a more diffuse and lighter orange to light reddish brown stain in the bentonite matrix beyond about 0.1-0.5 mm distance from the wire surface. Fragments of the dark brown to black oxide corrosion product were found to be ferromagnetic and could be attracted to a strong hand magnet. This suggests that the corrosion products possibly include magnetite (Fe_3O_4) or maghemite (γ-Fe_2O_3).

As in the previous study (Milodowski et al., 2007) it was noticeable that the shrinkage behaviour of the bentonite matrix on drying was different between the heavy iron-stained central part of the steel wire-bearing region and the margins of the bentonite that were free of steel wires. The heavily iron-impregnated areas from the centre of the zone with abundant corroded steel wire displayed much less shrinkage and cracking after vacuum-drying than the margins of the zone that were free of corroded steel wires.

4.1.2.2 DETAILED PETROGRAPHY

Alteration around the corroded iron coupon

Overall, very little alteration was observed in the bentonite in contact with the corroded iron coupon (Figure 13). The Ca distribution along a profile from the contact with the iron into the bentonite (Figure 14) shows a slight enhancement of Ca of up to 1.8 wt. % Ca (compared to 0.8 wt. % for background bentonite) within 0 to 100 µm from the metal surface. Elsewhere, the variation in Ca reflects the distribution of primary Ca-rich mineral grains such as plagioclase, apatite and calcite, within the bentonite.

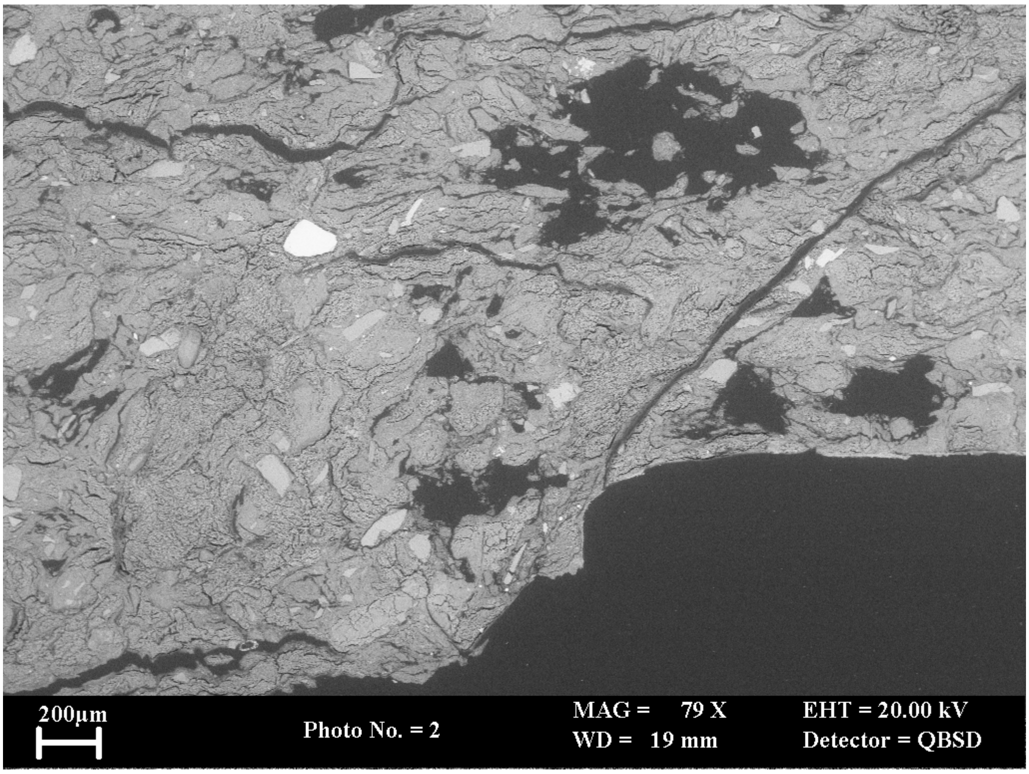

Figure 13. BSEM photomicrograph of the contact between corroded iron coupon (bottom right). The coupon was not present in the sample. A very thin bright layer is seen along the contact margin, representing secondary calcium carbonate. NF-PRO-Experiment NFC4 (Serco Assurance Section 1, Cell 4 – BGS sample MPLM768)

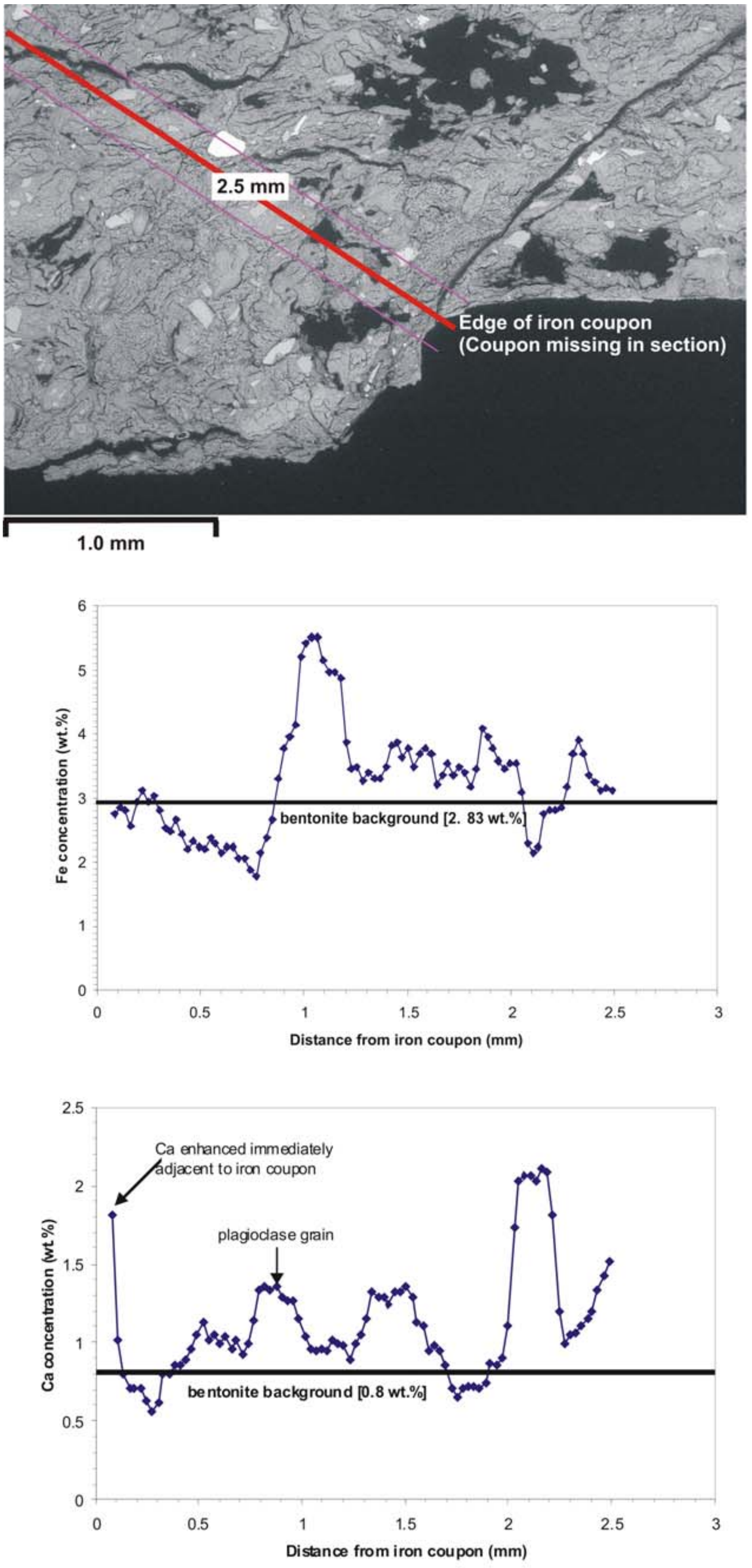

Figure 14. EDXA concentration profiles for Fe and Ca in bentonite with distance from corroded iron coupon. Line of profile shown in BSEM photomicrograph (top). NF-PRO-Experiment NFC4 (Serco Assurance Section 1, Cell 4 "steel side/bentonite" – BGS sample MPLM768)

Despite visible orange-red staining around the iron coupon, no significant Fe enrichment was detected in the bentonite adjacent to the iron metal, above background variations due to original iron oxide and other iron-bearing mineral phases. Elemental maps for Si, Al, P, Na, K, and Mg displayed no obvious alteration effects related to the corrosion of the iron coupon. Mn was below detection in all cases.

Alteration associated the corroded steel wires

BSEM petrographical analysis revealed significant alteration of the bentonite matrix in contact with corroding steel wires in Serco Assurance Section 1, Cell 4 "wire/bentonite" (BGS sample MPLM771).

The corroded wires are surrounded by an alteration halo of bentonite with enhanced concentrations of Fe, extending up to 0.5 mm from the surface of the corroding metal (Figure 15, Figure 16, Figure 17 and Figure 18). Fe concentration varies from c. 10 wt % adjacent to the metal to background bentonite values (c.2.9 wt % Fe) at a distance of about 1-2 mm. This clearly exceeds the amount of iron that can be simply present in cation exchange sites in the smectite (see Section 4.3). BSEM observations show that fine iron oxide is sometimes present immediately adjacent to the metal surface, and this has been shown by XRD analysis to include magnetite (Section 4.2.2.1), which accounts for the magnetic properties observed in this alteration product. However, in many cases, discrete iron oxide could not be resolved by BSEM within the Fe-enriched bentonite alteration zone. This might indicate that the iron is incorporated within the sheet silicate structure of the smectite. Alternatively, it may be that the iron is present as extremely finely disseminated iron oxide that is below the resolution of the scanning electron microscope technique.

In some cases, the Fe has been concentrated along a series of "fronts" (e.g. Figure 15) within the clay matrix, where the Fe content of the clay may be several tens of percent [note: this is not shown in the profile in Figure 19 because the line of profile intercepts a grain of calcite at this point].

Around many of the wires, the Fe enrichment penetrates into the bentonite matrix along microfractures that radiate away from the corroding metal, in a "stellate" pattern (Figure 16). The fractures have formed by shrinkage of the clay, which may be accentuated in the thin sections by post-experimental sample drying and preparation. However, the fact that these fractures are coated with iron oxides and the adjacent clay matrix of the fracture walls is impregnated and enriched in Fe, demonstrates clearly that these microfractures must have formed during the operation of the experiment. Fe oxide also penetrates along the boundaries of discrete areas or "domains" of bentonite that represent the boundaries of the original unhydrated bentonite grains.

Pockets of a very fine grained Mg-Al-Fe-silicate alteration product are caught up within the Fe-enrichment zone (Figure 15, Figure 17 and Figure 18). This Mg-rich phase occurs as patches in the Fe-enhanced bentonite and as a discontinuous zone, extending from the corroded metal surface out to 300 μm, from the steel. It appears to have replaced the original clay mineral fabric but it is unevenly distributed around the corroded steel wires, tending to be preferentially developed on one side of a wire (e.g. Figure 19). EXDA element profiles indicate that this phase contains up to 20 wt. % Mg. In addition, Si, Al and Fe are major components, and Ca is also detectable. The high Mg content of this alteration product might be consistent with that expected from saponite [$(\frac{1}{2}Ca,Na)_{0.66}Mg_6(Si_{7.34}Al_{0.66})O_{20}.(OH)_4.\ nH_2O$] (published data indicate up to 20 wt.% Mg, e.g. Deer et al., 1962), a Mg-rich chlorite [$(Mg,Al,Fe)_{12}(Si,Al)_8O_{20})(OH)_{16}$] (published data indicate up to 22 wt.% Mg, e.g. Deer et al., 1962) or talc [$Mg_6(Si_8O_{20})(OH)_4$] (theoretically 19.2 wt.% Mg).

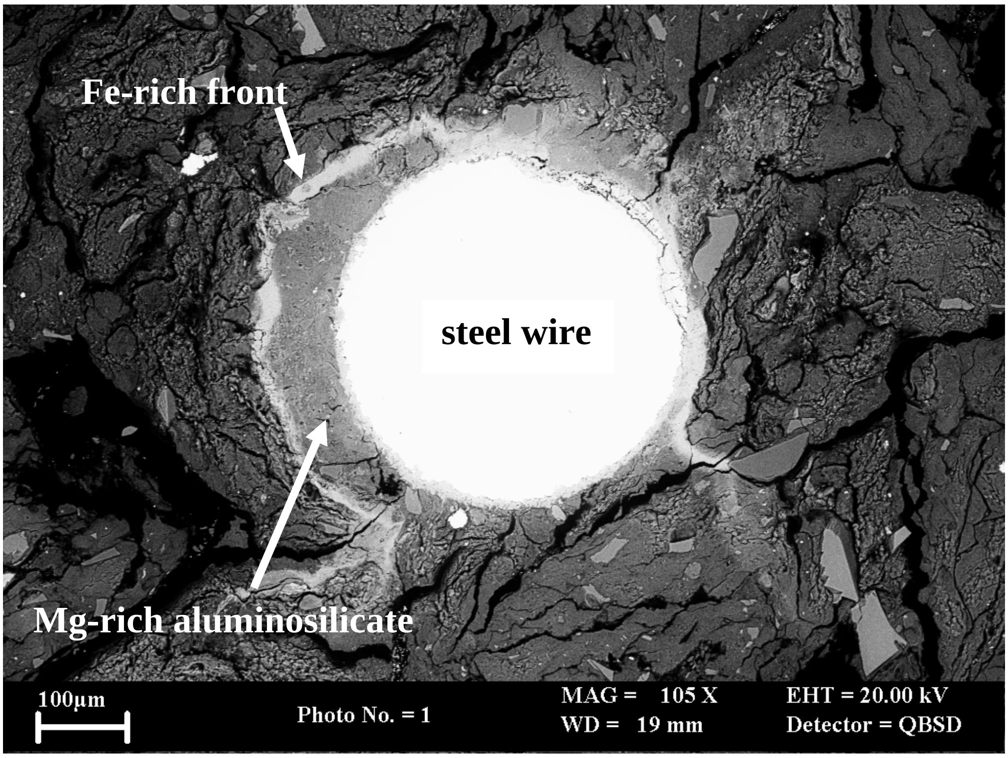

Figure 15. BSEM photomicrograph showing a halo of Fe-enriched altered bentonite (light grey) around a corroded steel wire, which encloses "pockets" of secondary Mg-rich aluminosilicate. NF-PRO-Experiment NFC4 (Serco Assurance Section 1, Cell 4 "wire/bentonite"– BGS sample MPLM771)

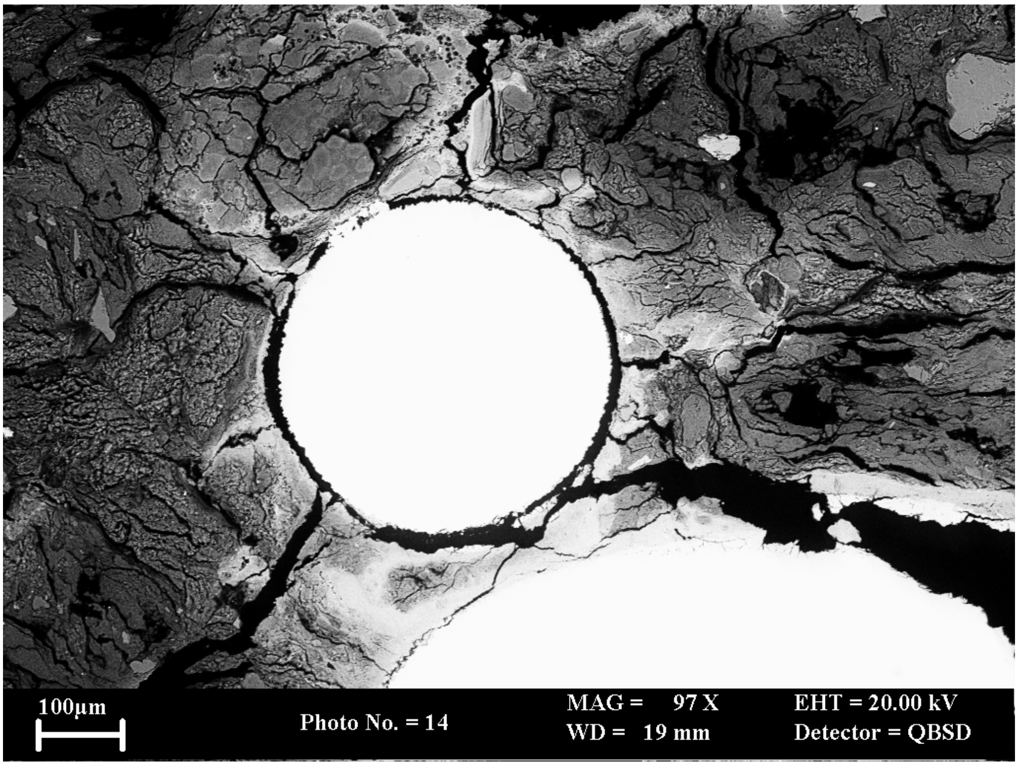

Figure 16. BSEM photomicrograph showing a halo of Fe-enriched altered bentonite (light grey) around corroded steel wires. Microfractures in the bentonite radiating away from the wire are lined by iron oxides (white), and are associated with enrichment of Fe in the adjacent clay matrix. NF-PRO-Experiment NFC4 (Serco Assurance Section 1, Cell 4 "wire/bentonite"– BGS sample MPLM771)

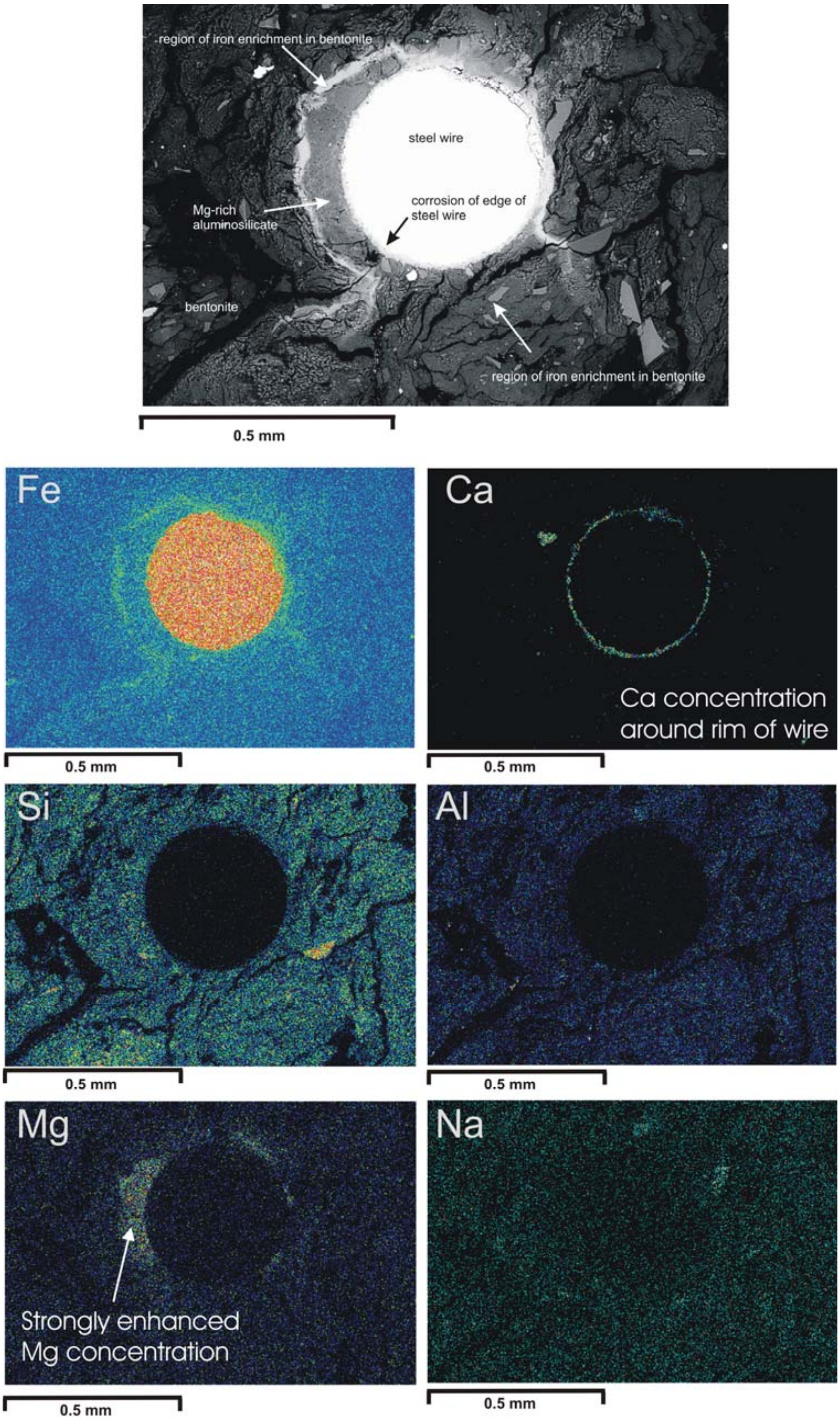

Figure 17. BSEM photomicrograph (top) with corresponding EXDA maps for Fe, Ca, Si, Al, Mg and Na distributions in bentonite around a corroding steel wire. Fe and Ca display enhanced concentrations in the bentonite close to the corroding steel wire, with Fe enrichment along a network of microfractures in the bentonite matrix; Si and Al display slight depletion relative to background bentonite; Mg locally displays patches of very strong enhancement in the bentonite within the zone of Fe-enrichment; Na distribution is largely unaffected by corroding metal. NF-PRO-Experiment NFC4 (Serco Assurance Section 1, Cell 4 “wire/bentonite” – BGS sample MPLM771)

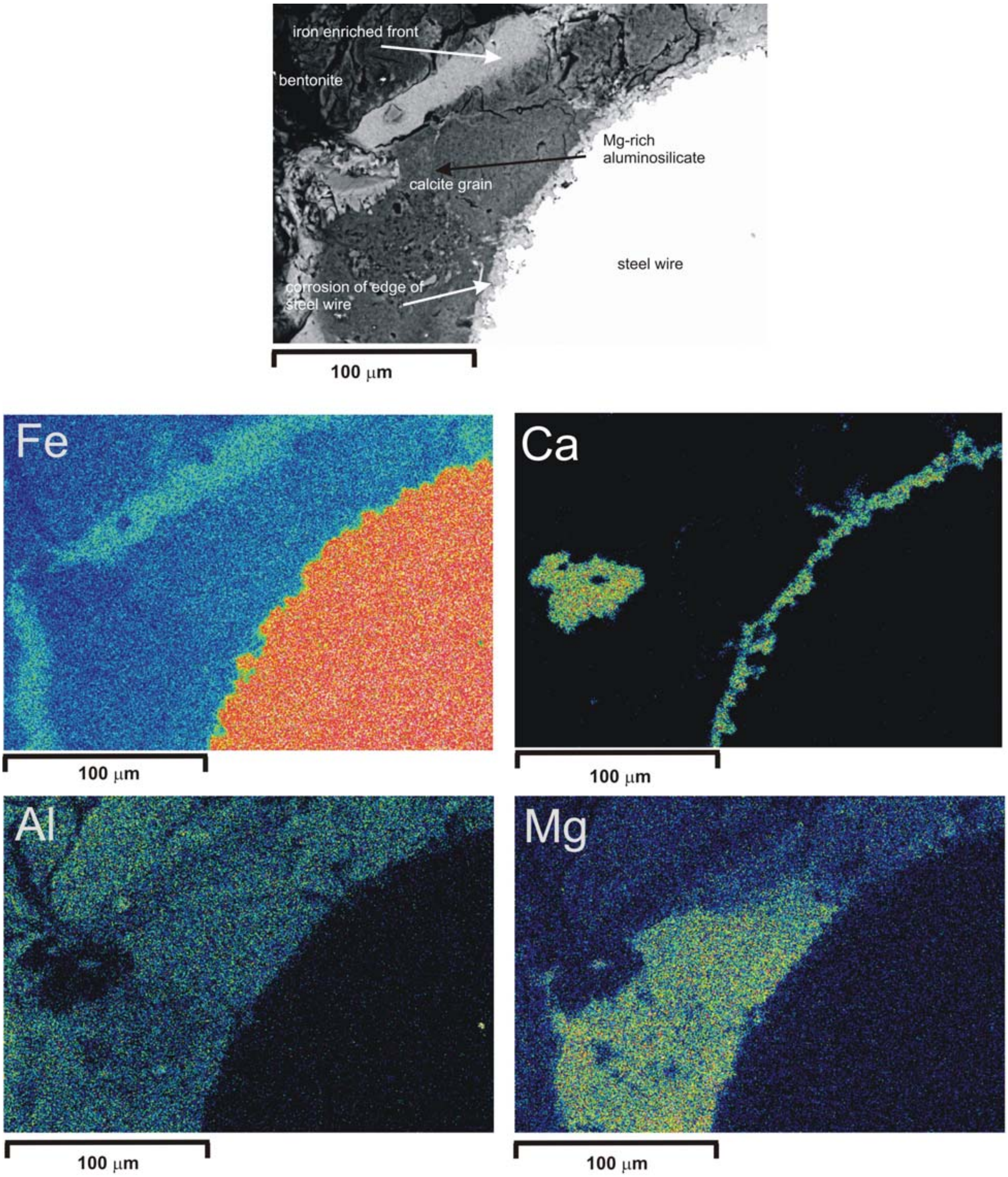

Figure 18. BSEM photomicrograph (top) with corresponding EXDA maps for Fe, Ca, Al and Mg distributions in bentonite around a corroding steel wire. Fe and Ca display enhanced concentrations in the bentonite close to the corroding steel wire; Si is slightly depleted relative to background bentonite; Mg possibly displays a very slight enhancement in the bentonite close to corroding steel. NF-PRO-Experiment NFC4 (Serco Assurance Section 1, Cell 4 "wire/bentonite" – BGS sample MPLM771)

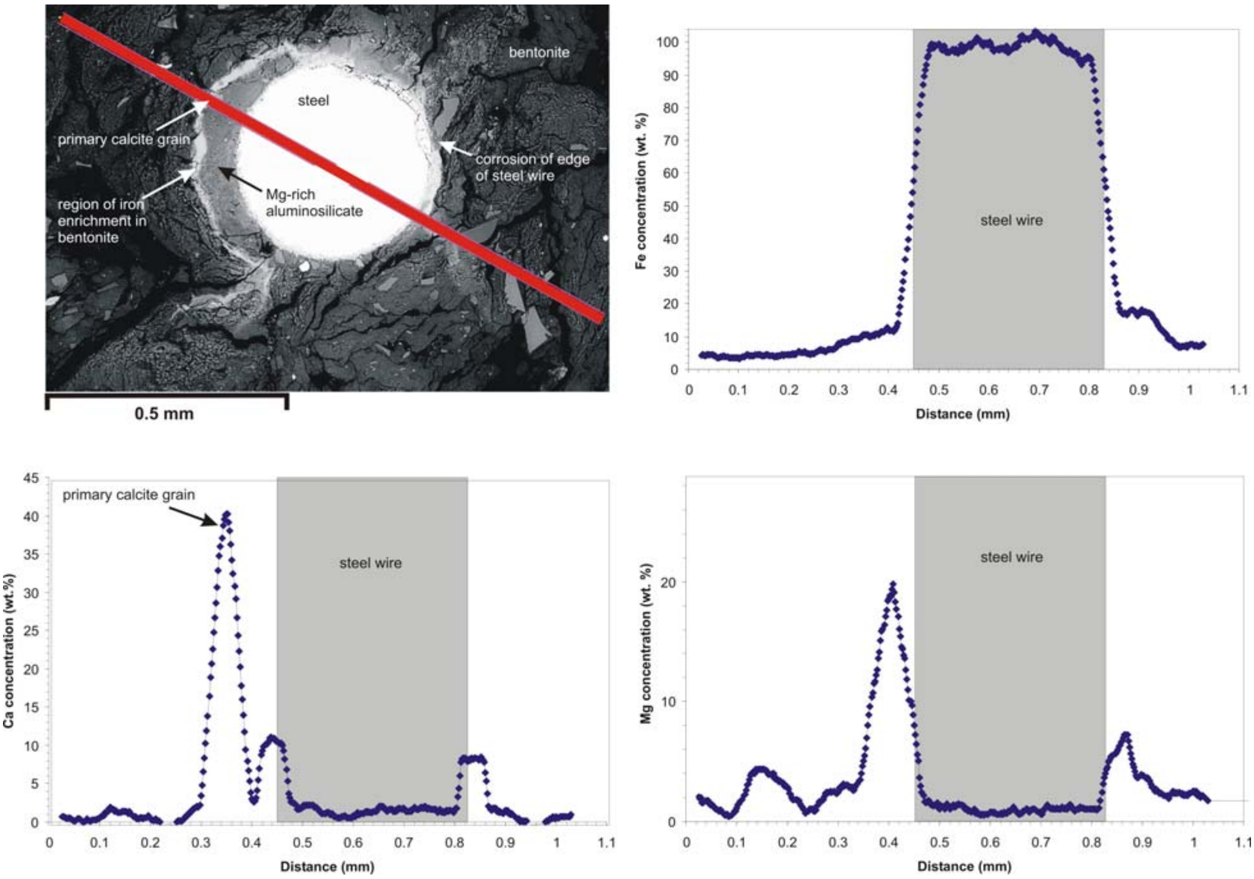

Figure 19. EDXA concentration profiles for Fe, Ca and Mg in bentonite with distance from corroding steel wire. Line of profile shown in BSEM photomicrograph (top). NF-PRO-Experiment NFC1 (Serco Assurance Section 1, Cell 4 "wire/bentonite" – BGS sample MPLM771)

EDXA microchemical maps (Figure 17 and Figure 18) and elemental profiles (Figure 19) show that Ca is concentrated within in the bentonite immediately adjacent to the corroded metal surface. BSEM-EDXA petrographical analysis shows that this coincides with the formation of an alteration band of secondary calcium carbonate, which has precipitated along this interface, and locally along the shrinkage cracks in the bentonite that are impregnated by Fe. XRD analyses (Section 4.2.2.1) show that this phase is probably aragonite.

The microchemical maps also highlighted the presence of rare grains of calcite that appear to have been present in the original bentonite.

No Mn was detected in the altered bentonite.

4.1.3 Experiment NFC 7

4.1.3.1 GENERAL OBSERVATIONS

The two small samples provided by SERCO Assurance from the cylinder of compacted bentonite recovered from Experiment NFC7 (Section 1 Cell 7 "carbon steel surface/bentonite" – BGS sample MPLM769, and Section 2 Cell 7 "wire/bentonite") represent material from the interface between a iron coupon and bentonite, and material from the edge of the central interval of bentonite containing disseminated steel wires, respectively. Both samples displayed visually-similar alteration characteristics to that seen in the experimental residue from NF-PRO Experiments NFC1 (Section 4.1.1.1) and NFC4 (4.1.2.1) and materials examined previously by Milodowski et al. (2007).

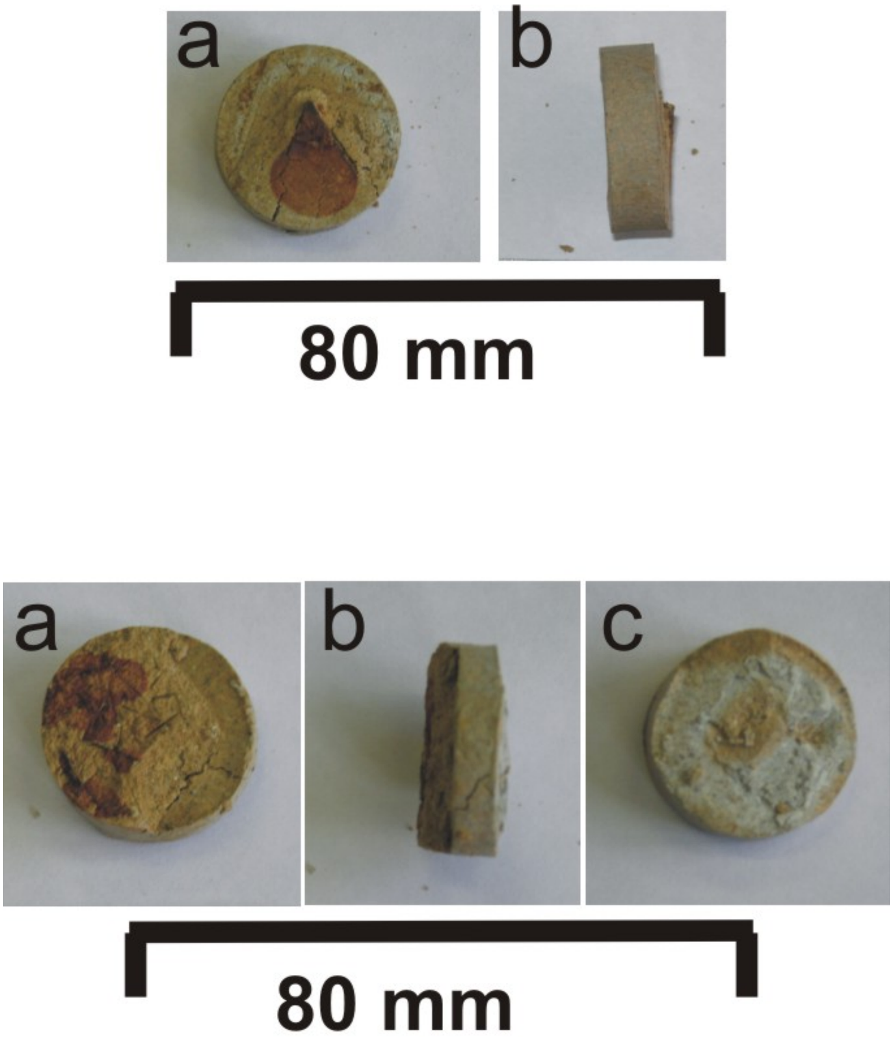

Figure 20. Photograph of bentonite samples from NF-PRO-Experiment NFC7. Top: Serco Assurance Section 1, Cell 7, "carbon steel surface/bentonite" (BGS sample MPLM769): (a) end-face containing ferruginous staining around a corroded iron coupon; (b) fractured perpendicular to axis showing the bentonite and the iron coupon to right hand side. Bottom: Serco Assurance Section 2, Cell 4 "wire/bentonite", BGS sample MPLM771): (a) end-face containing ferruginous staining around steel wires; (b) interface between heavily iron-stained zone and unaltered bentonite; (c) opposite end-face exposing relatively unaltered bentonite with patchy iron staining.

One face of the sample Section 1 Cell 7 "carbon steel surface/bentonite" (MPKM769) was defined by the interface between bentonite and a corroded iron coupon (Figure 20: top a). It was evident that the bentonite was stained by orange iron oxidation products within a narrow zone 2 to 4 mm wide around the edges of the metal (Figure 20: top a).

Much more significant alteration and reaction were evident in sample Section 2 Cell 7 "wire/bentonite"(MPLM772). The central region containing the dispersed steel wires displayed very strong red-brown to black staining of the bentonite within this region (Figure 20: bottom a, b and c). The iron-stained central region associated with the corrosion of the steel wires was quite patchy and extended for at least 5 mm from the margins of the zone containing the steel wires (Figure 20: bottom b, c). Much of the reddish brown ferruginous staining was developed along a fine, 'chicken wire mesh-like' network of interconnected hairline fractures within this central region, with extensive diffusive impregnation of the discolouration into the adjacent bentonite matrix. The steel wires were observed to be encrusted with a coating of black magnetic iron oxide, which suggests that this corrosion product is probably magnetite (Fe_3O_4) or maghemite (γ-Fe_2O_3).

4.1.3.2 DETAILED PETROGRAPHY

Alteration around the corroded iron coupon

In contrast to NF-PRO Experiment NFC4, more alteration was observed in the bentonite in contact with the corroded metal from Experiment NFC7 (Figure 21). The surface of the metal was found to be pitted and corroded, with embayments varying from <10 to 50 µm deep (Figure 21). As seen in the other NF-PRO experiments, the bentonite surrounding the corroded steel is enriched in Fe (Figure 21 and Figure 22). The zone of Fe-enhancement detectable by EDXA extends to about 0.5 mm from the metal surface, although staining by iron was visually observed to extend to 4 mm. However, no discrete iron oxide was observed under BSEM in the thin section.

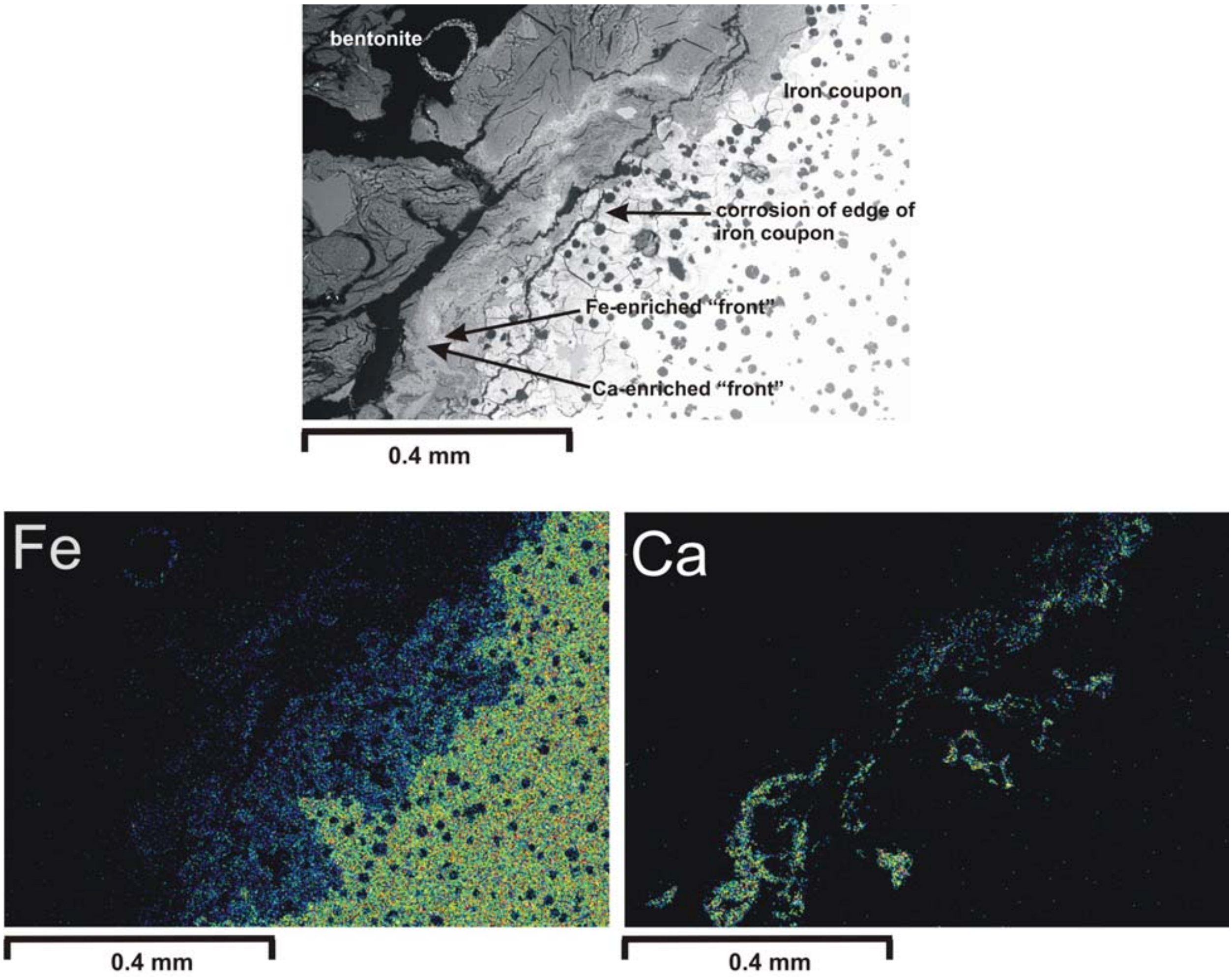

Figure 21. BSEM photomicrograph (top) showing corroded and embayed surface of the iron coupon (white) surrounded by a narrow zone of altered bentonite with "wispy" batches of bentonite containing an enhanced concentration of Fe (light grey). EDXA microchemical maps for Fe and Ca are shown for the same area, showing Fe enrichment of the clay matrix and "fronts" of Ca enrichment. [Note: dark specs in the bright iron coupon are grains of embedded polishing paste] NF-PRO-Experiment NFC7 (Serco Assurance Section 1, Cell 7 "carbon steel surface/bentonite"– BGS sample MPLM769)

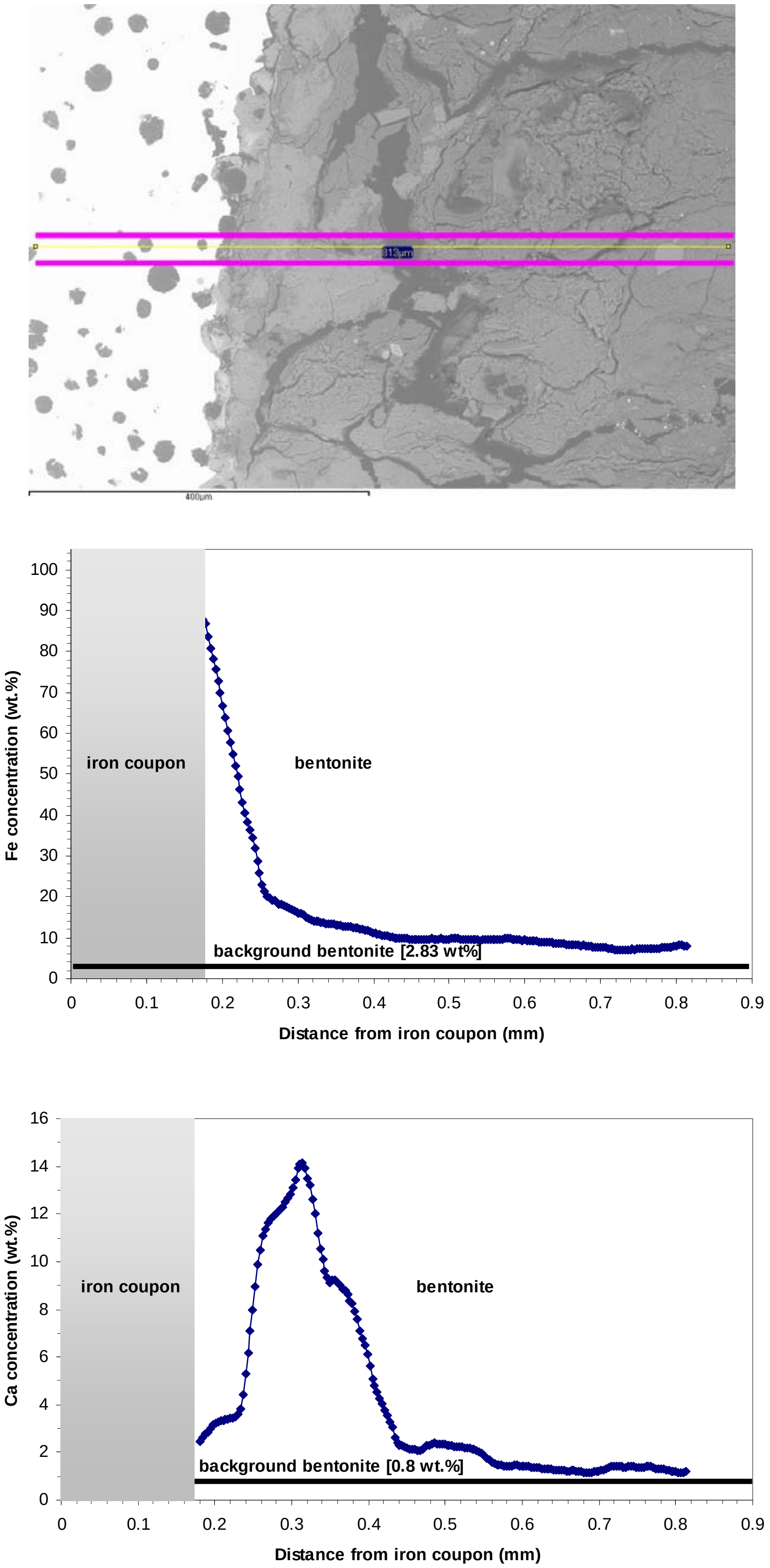

Figure 22. BSEM photomicrograph (top) with distribution profiles for Fe (middle) and Ca (bottom) in the bentonite alteration zone around corroded iron coupon. [Note: dark specs in the bright iron coupon are grains of embedded polishing paste] NF-PRO-Experiment NFC7 (Serco Assurance Section 1, Cell 7 "carbon steel surface/bentonite" – BGS sample MPLM769)

EDXA microchemical maps and element distribution profiles show that Ca is concentrated within the altered bentonite (Figure 21 and Figure 22). Some of the Ca concentrations correspond to patches of secondary calcium carbonate replacing or cementing the clay matrix (Figure 22). Ca-rich bands are also developed immediately adjacent to the steel surface, and at the "leading edge" of concentration "fronts" of Fe (Figure 21). Close examination by BSEM-EDXA revealed that these concentration "fronts" were also due to the formation of very fine secondary calcium carbonate.

Within the altered zone, the bentonite displays the development of microfracturing, particularly between 0 to 300 µm of the metal surface. Although the microfracturing is probably exaggerated by shrinkage during sample drying and section preparation, the clay matrix of the fracture walls is strongly enriched in Fe, indicating that these fractures had formed during the experiment and that they represented pathways for transport of Fe from the corroding metal. Generally, the "iron-impregnated" bentonite was observed to display less shrinkage upon sample drying than the "background" unaltered bentonite.

Alteration associated the corroded steel wires

BSEM petrographical analysis revealed significant alteration of the bentonite matrix in contact with corroding steel wires in Serco Assurance Section 1, Cell 7 "wire/bentonite" (BGS sample MPLM772). The alteration characteristics of the bentonite are very similar to that observed around corroded steel wires in NF-PRO Experiment NFC4 (4.1.2).

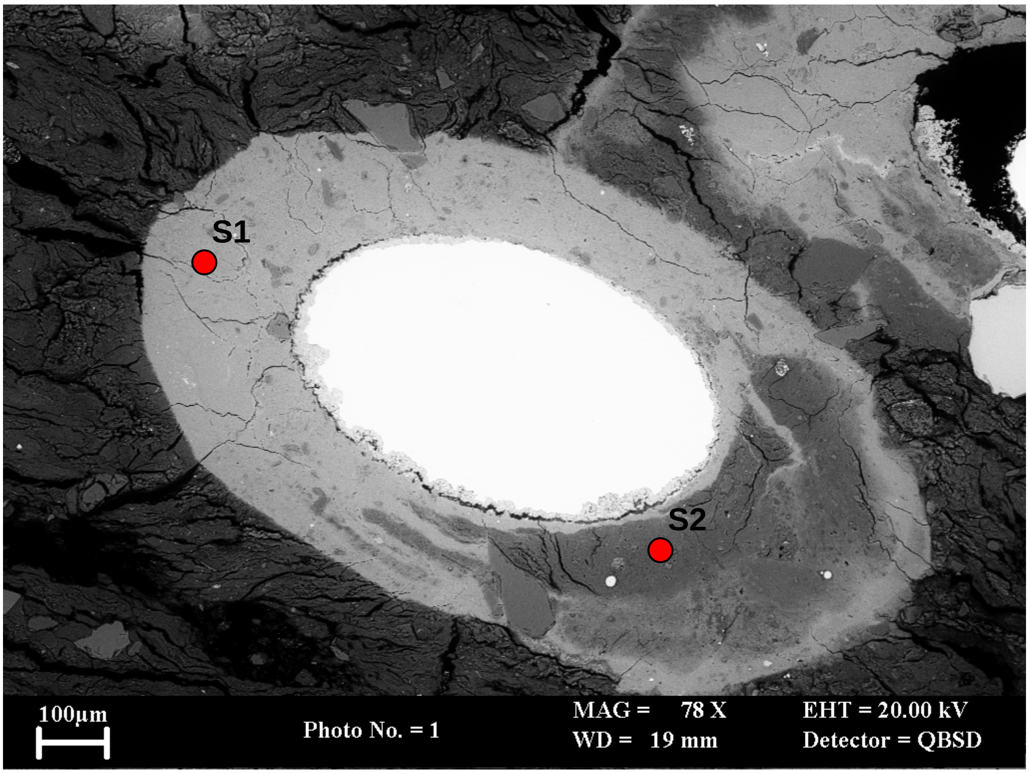

Figure 23. BSEM photomicrograph showing corroded steel wire (bright) in bentonite (dark). A thick alteration halo of Fe-impregnated/enriched aluminosilicate material (light-grey) surrounds the corroded wire, enclosing and partly replacing patches of Mg-Al-Fe-rich clay (mid-grey). S1, S2 and S3 refer to EDXA spectra shown in Figure 24 and Figure 25. NF-PRO Experiment NFC7 (Serco Assurance Section 2, Cell 7 "wire/bentonite" – BGS sample MPLM772).

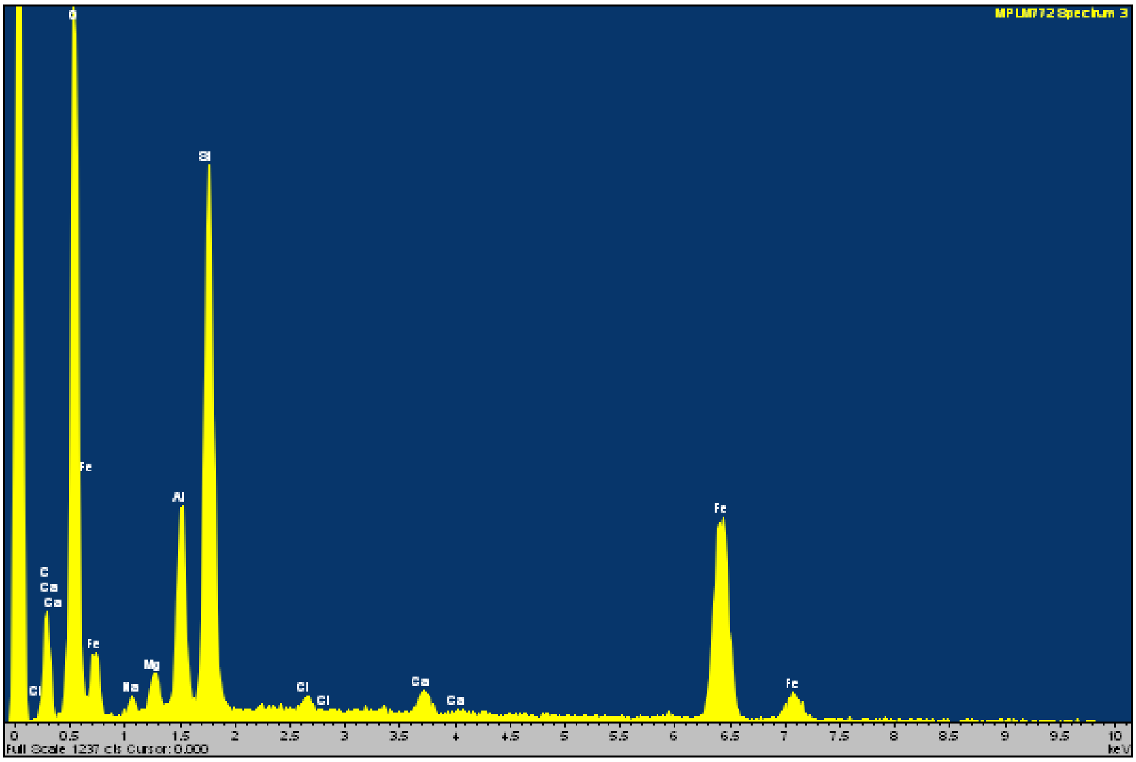

Figure 24. EDXA spectrum of Fe-rich aluminosilicate alteration product (S1) within altered bentonite halo in Figure 23. NF-PRO-Experiment NFC7 (Serco Assurance Section 2, Cell 7 "wire/bentonite" – BGS sample MPLM772)

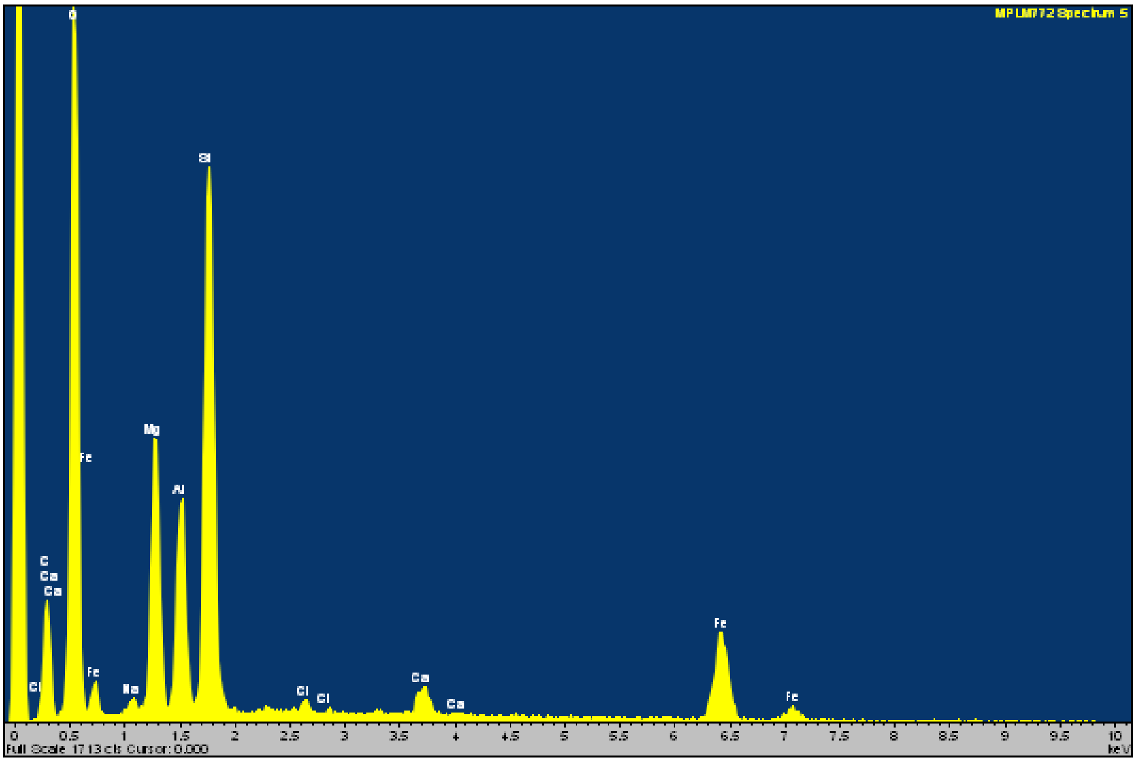

Figure 25. EDXA spectrum of Mg-rich aluminosilicate alteration product (S2) within altered bentonite halo in Figure 23. NF-PRO-Experiment NFC7 (Serco Assurance Section 2, Cell 7 "wire/bentonite" – BGS sample MPLM772)

Figure 23 illustrates the typical alteration associated with the corrosion of steel wires. Thick Fe-rich alteration haloes (up to 500 µm thick) have formed around the wires. The clay matrix in these haloes has been largely replaced or impregnated by a Fe-rich aluminosilicate phase ("S1" in Figure 23, with a composition shown by the EDXA spectrum illustrated in Figure 24). The alteration haloes have a very sharp boundary but qualitative BSEM-EDXA observations showed that the bentonite has enhanced concentrations of Fe extending at least 1 mm beyond this boundary, albeit at a much lower concentration. Si and Al show a relative depletion compared to the background bentonite.

Microfractures lined by very fine grained iron oxide radiate from the altered bentonite (e.g. Figure 26). The clay matrix in the walls of these fractures has an elevated Fe concentration, similar to that seen in the matrix of the main alteration halo. Discrete iron oxide phase could not be resolved within the Fe-rich clay matrix of the alteration halos nor in the clay matrix adjacent to the iron oxide-mineralised fractures. This suggests that the alteration product is Fe-rich aluminosilicate material, or that any iron oxide that might be present is too fine to be resolved by scanning electron microscopy.

Broad bands or patches of a Mg-Fe-rich aluminosilicate phase ("S2" in Figure 23, with a composition shown by the EDXA spectrum illustrated in Figure 25) occur within the Fe-rich alteration halo (see also Figure 26, Figure 27 and Figure 28). The Mg-rich phase is not formed immediately adjacent to the metal but within a zone of the order of 50-100 µm distant from the metal surface. Many of the steel wires show a fairly even distribution of alteration products around them. However, in some cases, the secondary Mg-rich alteration product was observed to have preferentially formed on one side of the corroded wire, as shown in Figure 23 and Figure 26. This reaction product appears to have formed relatively early in the alteration process, and is now partially replaced or overprinted by Fe-rich aluminosilicate.

As in NF-PRO Experiment NFC4, EXDA element profiles indicate that this Mg-rich phase may contain up to 20 wt. % Mg. In addition, Si, Al and Fe are major components, and Ca is also detectable (Figure 27 and Figure 28). The high Mg content of this alteration product might be consistent with that expected from saponite $[(\frac{1}{2}Ca,Na)_{0.66}Mg_6(Si_{7.34}Al_{0.66})O_{20}.(OH)_4.\ nH_2O]$ (published data indicate up to 20 wt.% Mg, e.g. Deer et al., 1962), an Mg-rich chlorite $[(Mg,Al,Fe)_{12}(Si,Al)_8O_{20})(OH)_{16}]$ (published data indicate up to 22 wt.% Mg, e.g. Deer et al., 1962) or talc $[Mg_6(Si_8O_{20})(OH)_4]$ (19.2 wt.% Mg). Alternatively, the EDXA data for this alteration product could be accounted for by a mixture of these minerals.

EDXA microchemical maps and element distribution profiles reveal that Ca is concentrated in a rim close to the corroded steel surface (Figure 26 and Figure 27). This phenomenon is similar to that observed in the reacted bentonite from the other NF-PRO experiments examined in this present study and in the previous study by Milodowski et al. (2007). As in the other experiments, closer examination by BSEM-EDXA indicates that this Ca concentration corresponds to the precipitation of a band of fine grained calcium carbonate along the original interface between the steel and the bentonite. By analogy with the XRD results from the other experiments (Section 4.2.2), this is probably aragonite. Some alteration haloes display a complex distribution of Ca and Mg (Figure 28). In addition to Ca concentration along the corroded steel-bentonite interface, Ca may also be concentrated within several discrete "bands" within the alteration halo. It appears to show an antithetic relationship to Mg, being concentrated as in a series of "chemical fronts" just ahead of Mg peak concentrations moving outwards from the corroding metal. Ca may also concentrate at the leading edge of the Fe "front" defining the sharp boundary of the alteration halo (Figure 28).

EDXA microchemical maps showed that Cl was sometimes concentrated within the iron oxide corrosion products of the steel wires (Figure 26). However, not all corroded steel wires in this experiment were found to be associated with high levels of Cl. No Mn was detected in the altered bentonite.

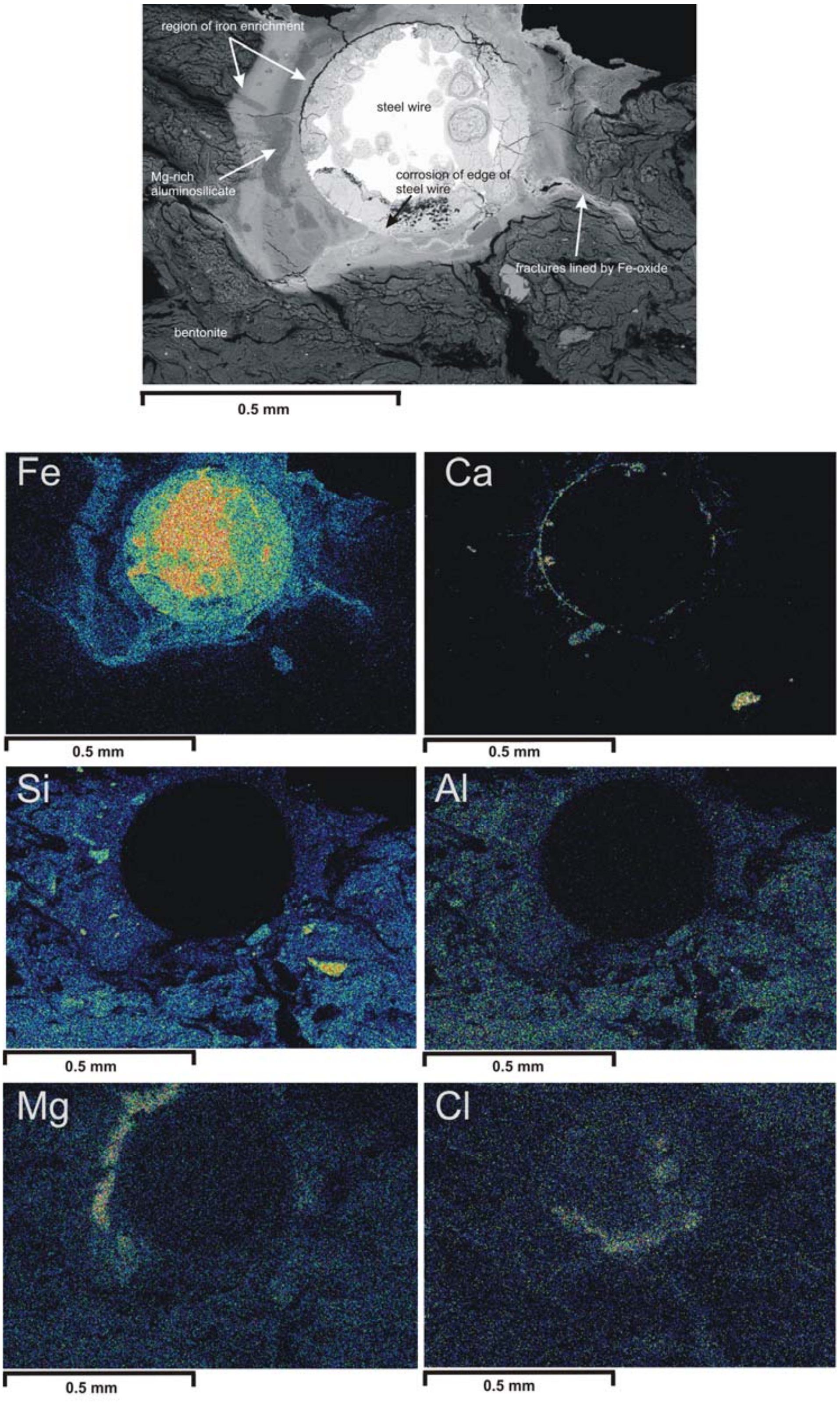

Figure 26. BSEM photomicrograph (top) with corresponding EXDA maps for Fe, Ca, Si, Al, Mg and Cl distributions in bentonite around a corroding steel wire. Ca displays enhanced concentrations in the bentonite close to the corroding steel wire, surrounded by a zone of Fe enrichment, which locally extends into the bentonite along a network of microfractures; Si and Al display slight depletion relative to background bentonite; Mg locally displays patches of very strong enhancement within the zone of Fe-enrichment; Cl is locally associated with iron oxides formed at the corroded metal surface. NF-PRO-Experiment NFC7 (Serco Assurance Section 2, Cell 7 "wire/bentonite" – BGS sample MPLM772)

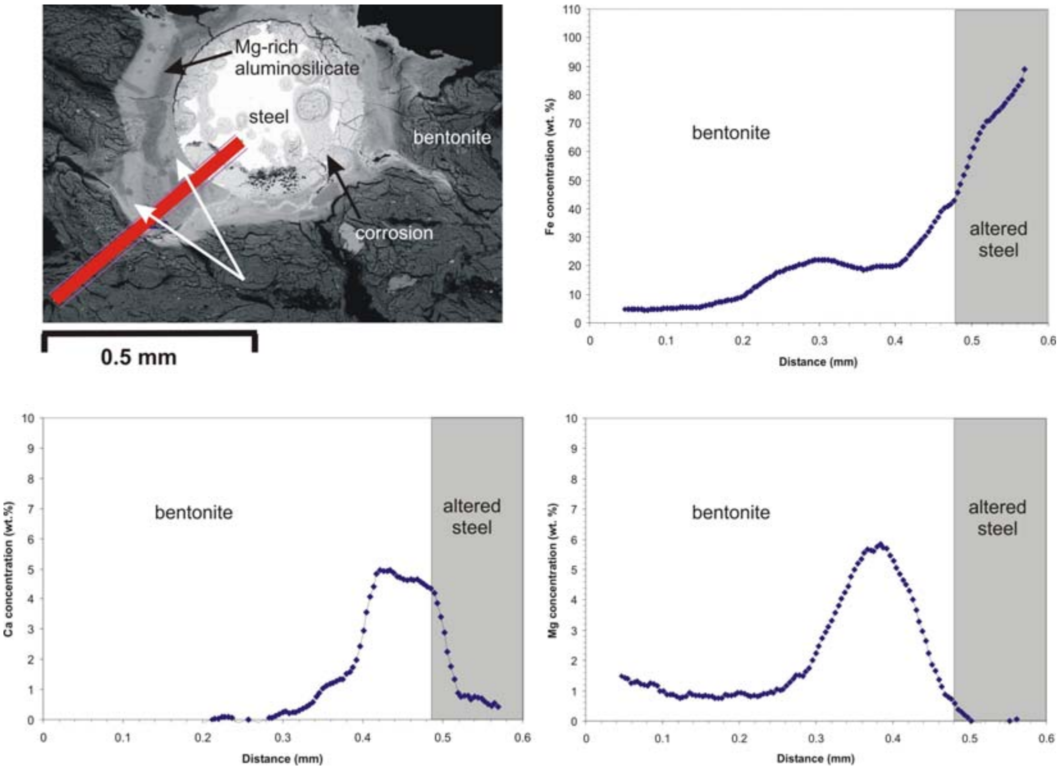

Figure 27. EDXA concentration profiles for Fe, Ca and Mg in bentonite with distance from corroding steel wire. Line of profile shown in BSEM photomicrograph (top). NF-PRO-Experiment NFC7 (Serco Assurance Section 2, Cell 7 "wire/bentonite" – BGS sample MPLM772)

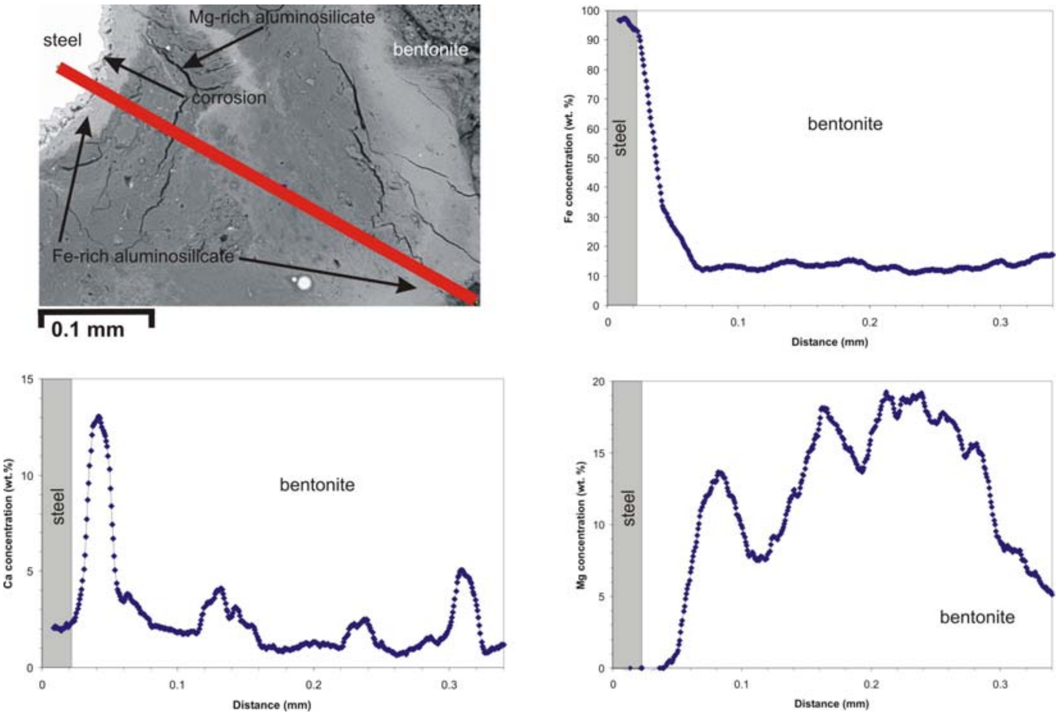

Figure 28. EDXA concentration profiles for Fe, Ca and Mg in bentonite with distance from corroding steel wire.. showing detail of Ca and Mg concentrations along a series of antithetic "fronts" within with Fe-enriched altered bentonite halo. Line of profile shown in BSEM photomicrograph (top). NF-PRO-Experiment NFC7 (Serco Assurance Section 2, Cell 7 "wire/bentonite" – BGS sample MPLM772)

4.1.4 Experiment NFC13

4.1.4.1 GENERAL OBSERVATIONS

The two small samples provided by SERCO Assurance from the cylinder of compacted bentonite recovered from Experiment NFC13 (Section 1 Cell 13 “cell end section”, BGS sample MPLM770), and Section 2 Cell 13 “wire/bentonite”, BGS sample MPLM773) represent background unaltered bentonite from the end of the reaction cell, and material from the edge of the central interval of bentonite containing disseminated steel wires, respectively. The background bentonite sample (BGS sample MPLM770) comprised compacted grey-green clay and showed no visible signs of alteration (Figure 29: top), except for the development of shrinkage cracks following drying under vacuum. Section 1 Cell 13 “steel side/bentonite” (MPKM773) displayed visually-similar alteration characteristics to that seen in the experimental residue from NF-PRO Experiments NFC1, NFC4 and NFC7, and reacted materials examined previously by Milodowski et al. (2007).

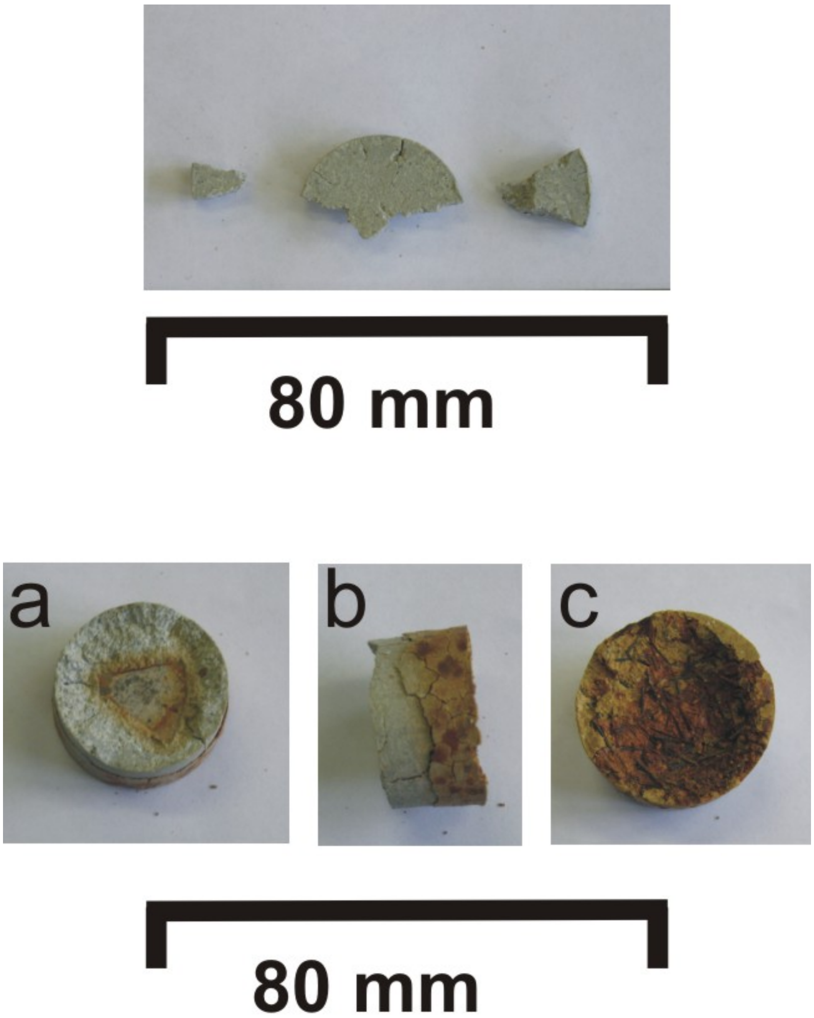

Figure 29. Photograph of bentonite samples from NF-PRO-Experiment NFC13. Top: Serco Assurance Section 1, Cell 13, “cell end section” (BGS sample MPLM770) showing unaltered grey-green background bentonite. Bottom: Serco Assurance Section 2, Cell 13 “wire/bentonite”, (BGS sample MPLM773): (a) end-face containing ferruginous staining and impression from corroded iron coupon (coupon removed); (b) interface between heavily iron-stained zone around corroded steel wires and unaltered bentonite; (c) end-face exposing corroded steel wires surrounded by halos of red-brown iron oxide and iron oxide-stained bentonite

One face of the sample Section 1 Cell 13 "steel side/bentonite" (MPKM773) was defined by the interface between bentonite and a corroded iron coupon (Figure 29: bottom a). It was evident that the bentonite was stained by orange iron oxidation products within a narrow zone 2 to 4 mm wide around the edges of the metal but with little or no iron oxide staining of the bentonite where it was adjacent to the face of the coupon (Figure 29: bottom b). Significant alteration and reaction was evident in part of the sample corresponding to the central region containing the dispersed steel wires. This displayed very strong red-brown staining of the bentonite within this region (Figure 29: bottom c). The iron-stained central region associated with the corroded steel wires extended to at least 5 mm from the margins of the zone containing the steel wires (Figure 12: bottom b). Much of the reddish brown ferruginous staining was developed along a fine, 'chicken wire mesh-like' network of interconnected hairline fractures within this central region, with extensive diffusive impregnation of the discolouration into the adjacent bentonite matrix.

Only the region of the reacted bentonite that contained dispersed corroded steel wires (BGS sample MPLM773) was examined petrographically.

Alteration associated the corroded steel wires

The alteration characteristics of bentonite associated with the corroded steel wires in NF-PRO Experiment NFC13, is very similar to that observed from NF-PRO experiments NFC4 (Section 4.1.2.2) and NFC7 (Section 4.1.3.2).

Alteration haloes with significant Fe-enrichment are seen in the bentonite in contact with the corroding steel (Figure 30). Most of the iron enrichment occurs within a zone up to 500 µm wide around the wire. However, slightly elevated iron concentrations were detected in the bentonite by EDXA for up to about 1 mm from the metal surface. Within the alteration zone, Si and Al show an antithetic relationship to Fe, which could be explained simply by the effect of the addition of Fe corrosion products from the corroding steel resulting in the dilution of Si and Al (illustrated by the Si distribution map in Figure 30). This might be expected to increase the volume of the clay matrix but actually appears to have caused shrinkage and microfracturing in the clay matrix, as seen in the other experiments.

Shrinkage microfractures in the clay matrix around the corroded steel wires are lined by fine iron oxide. The bentonite in the walls of the microfractures is also enriched in Fe (see Fe distribution map in Figure 30). The fractures vary from < 1 to 50 µm wide, and it can retain open porosity. In this sample some fractures, with associated Fe mineralisation, penetrate the bentonite for up to 1 mm from the corroding steel wires

At the inner edge of the alteration halo Ca was observed to be concentrated in a very narrow alteration rim, 1 to 20 µm wide, immediately adjacent to the corroding metal (Figure 30). BSEM-EDXA revealed that this corresponded to the formation of fine, fibrous, calcium carbonate, which XRD analysis indicates to be aragonite (Section 4.2.2.1). Ca was also found to be concentrated at the leading edge of the Fe-enriched bentonite halo, and sometimes within the Fe-enriched walls of microfractures in the altered bentonite. However, in this case the Ca was much more diffuse and no discrete calcium carbonate phase was differentiated by BSEM-EDXA.

A Mg-rich clay-like aluminosilicate alteration product was also found within the alteration halo (Figure 30). It appears to be very similar to that observed in NF-PRO experiments NFC4 and NFC7, containing significant Fe in addition to Mg. Detailed petrographical analysis and EDXA microchemical distribution maps showed that the Mg-rich phase formed close to the corroding metal, enclosing the zone of aragonite precipitation, where it formed a band up to 400 µm wide (Figure 30). It replaces the original smectite clay mineral matrix of the bentonite, leaving primary feldspar grains unaffected. Closer examination revealed that the Mg phase itself has suffered alteration and is being partially replaced or "overprinted" by more Fe-rich aluminosilicate material (Figure 31). These petrographical observations indicate that the Mg-rich phase formed relatively early, but possibly after aragonite. However, with progressive

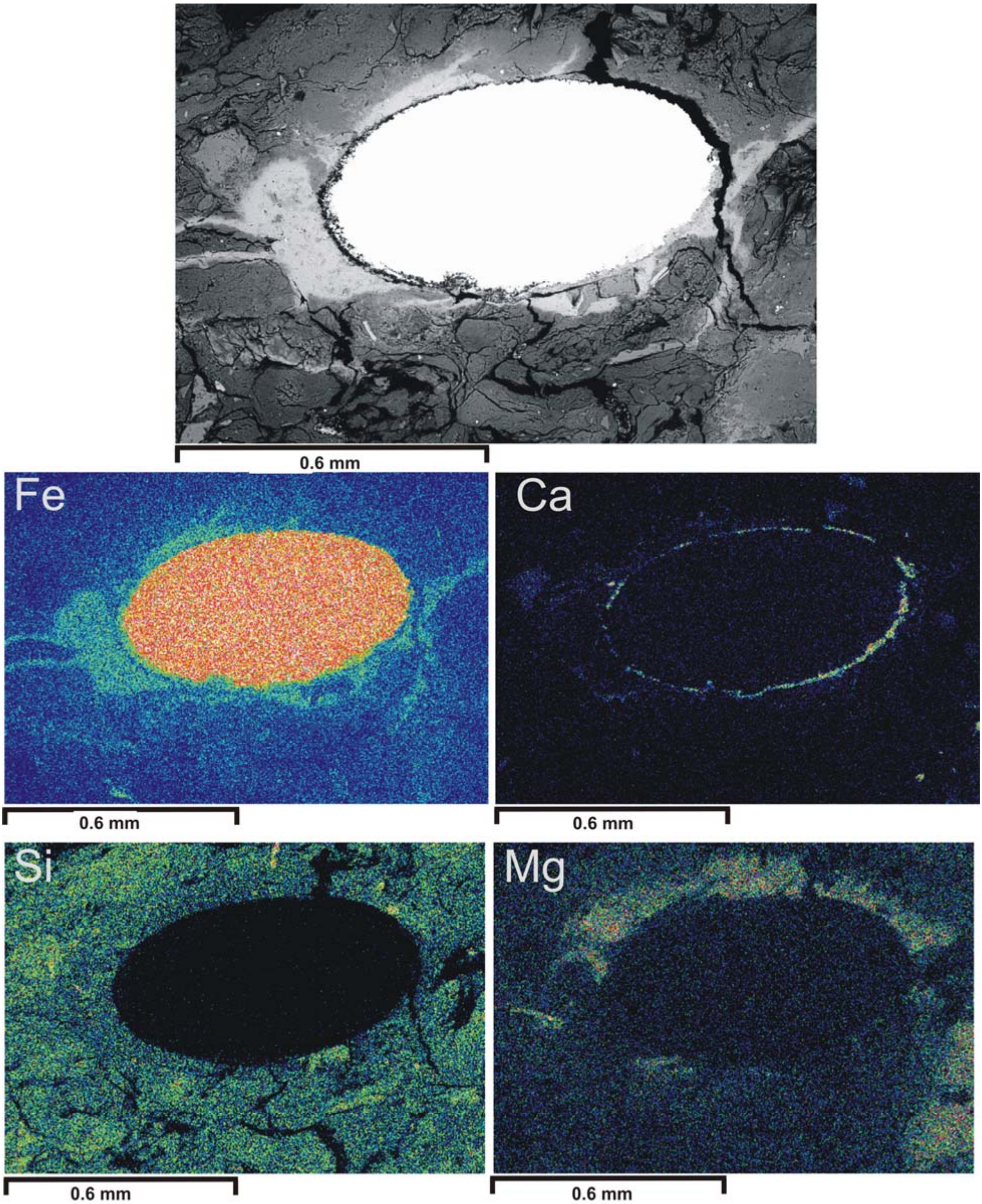

Figure 30. BSEM photomicrograph (top) with corresponding EXDA maps for Fe, Ca, Si and Mg distributions in bentonite around a corroding steel wire. Fe is concentrated in a broad alteration band around the steel wire, and along microfractures penetrating the surrounding bentonite matrix. Ca in concentrated in a narrow band immediately adjacent to the corroding metal, with weaker more diffuse concentrations of Ca evident at the margins of the alteration zone surrounded. Si displays a slight depletion within the Fe-rich alteration band, relative to background bentonite. Mg is concentrated is a broad but discontinuous band within the Fe-rich alteration zone but outside of the narrow Ca enriched band adjacent to the corroding metal. NF-PRO-Experiment NFC13 (Serco Assurance Section 2, Cell 13 “wire/bentonite” – BGS sample MPLM773

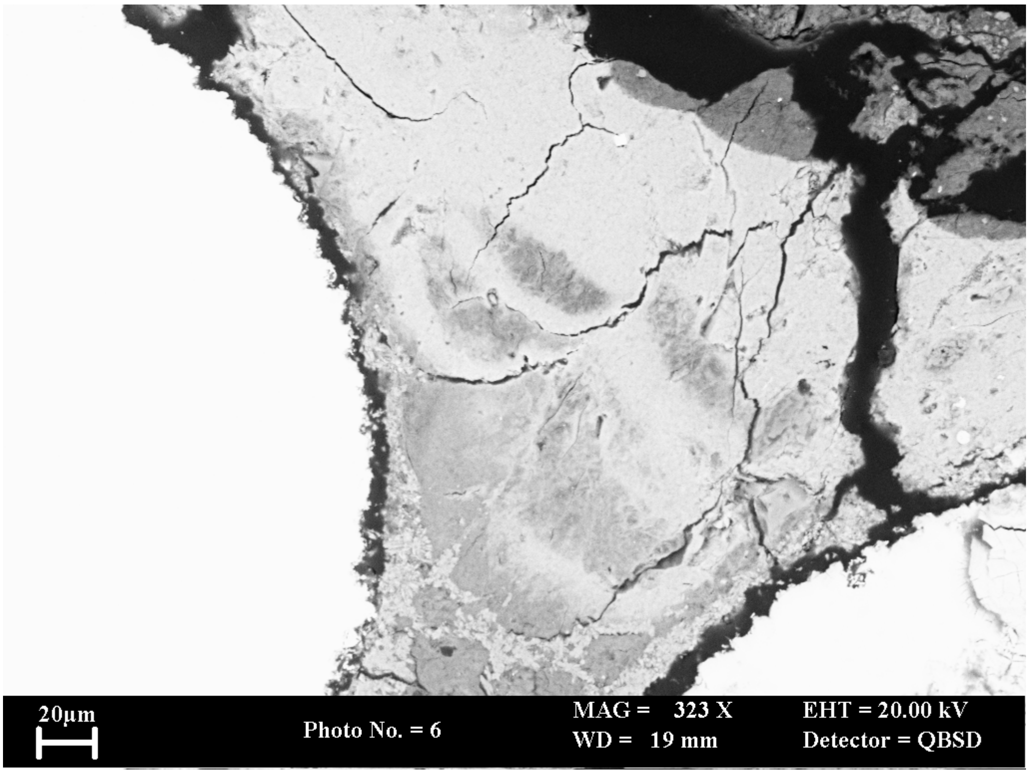

Figure 31. BSEM photomicrograph showing altered bentonite matrix between two corroded steel wires (white). Bands of Mg-rich aluminosilicate (mid grey) can be seen within a groundmass of Fe-rich aluminosilicate alteration. The Fe-rich alteration product appears to be replacing or overprinting the Mg-rich aluminosilicate. NF-PRO-Experiment NFC13 (Serco Assurance Section 2, Cell 13 "wire/bentonite" – BGS sample MPLM773

corrosion of the steel and migration of the dissolved Fe into the adjacent altered bentonite Mg was displaced by Fe, or the Mg-rich aluminosilicate was replaced by a more Fe-rich aluminosilicate. The same complex pattern and sequence of alteration was also evident in the altered bentonite in NF-PRO experiments NFC4 and NFC7.

No Mn was detected in the altered bentonite.

4.2 X-RAY DIFFRACTION ANALYSIS

The results of XRD analyses are summarised in Table 5 and Table 6.

4.2.1 "Unaltered" bentonite

4.2.1.1 Random orientation mount XRD

Random orientation XRD analyses indicate that the "unaltered", grey bentonite (represented by samples (MPLM768 and MPLM770) is predominantly composed of a smectite-group mineral together with minor-to-trace amounts of quartz, feldspar (albite and K-feldspar), cristobalite, calcite, undifferentiated mica species ("mica", possibly including muscovite, biotite, illite, illite/smectite etc) and pyrite (Figure 32). A possible trace of a zeolite-group mineral was also detected in sample MPLM768.

A mean d_{060} dimension of 1.4967 Å (range of values 1.4965 to 1.4969Å) for the "unaltered" grey bentonite subsamples indicates that the smectite-group mineral can be classified as dioctahedral and most likely is a montmorillonite species.

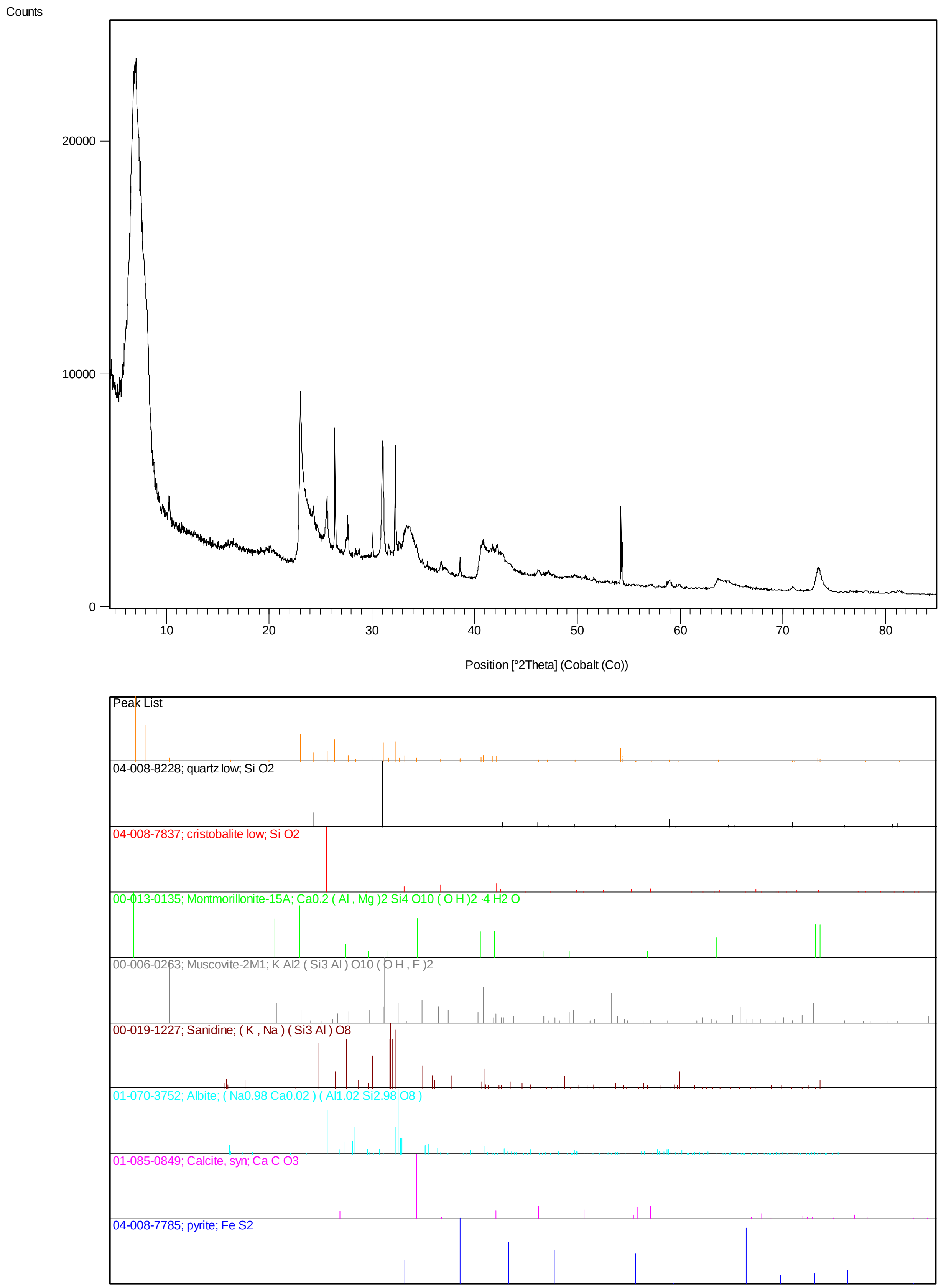

Figure 32. Random powder mount XRD trace for “unaltered” bentonite material (upper figure) compared to stick patterns for extracted peak information and ICDD standard patterns for the identified mineral phases (lower figure), sample MPLM770.

The montmorillonite in the “unaltered” grey bentonite samples displays an intense d_{001} spacing at c.14.9 Å but also shows a prominent high angle shoulder to this peak at c.13.0 Å. The position of the montmorillonite d_{001} peak can be affected both by its interlayer cation chemistry and the hydration state of these cations. Therefore, the c.14.9 Å spacing may suggest that divalent (Ca/Mg) cations dominate the smectite interlayer cations with subordinate monovalent (Na/K) cations suggested by the c.13.0 Å shoulder. However, as the relative humidity of the XRD analyses were not controlled, both spacings may result from differential hydration of different montmorillonite crystallites.

The presence of composite montmorillonite peaks in this study precluded an assessment of crystallite size distributions using the FWHM (Full Width at Half Maximum) parameter, as used in the first study.

4.2.1.2 Oriented mount XRD

Oriented mount XRD analyses confirm that the clay mineral assemblage of the “unaltered” bentonite (represented by samples (MPLM768 and MPLM770) is dominated by montmorillonite with small quantities of ‘mica’. As well as the non-clay minerals identified by random orientation XRD (see Section 4.2.1), a low intensity peak at 8.94Å in the air-dry traces of both “unaltered” bentonite samples additionally suggest the presence of small quantities of a zeolite-group mineral, probably heulandite.

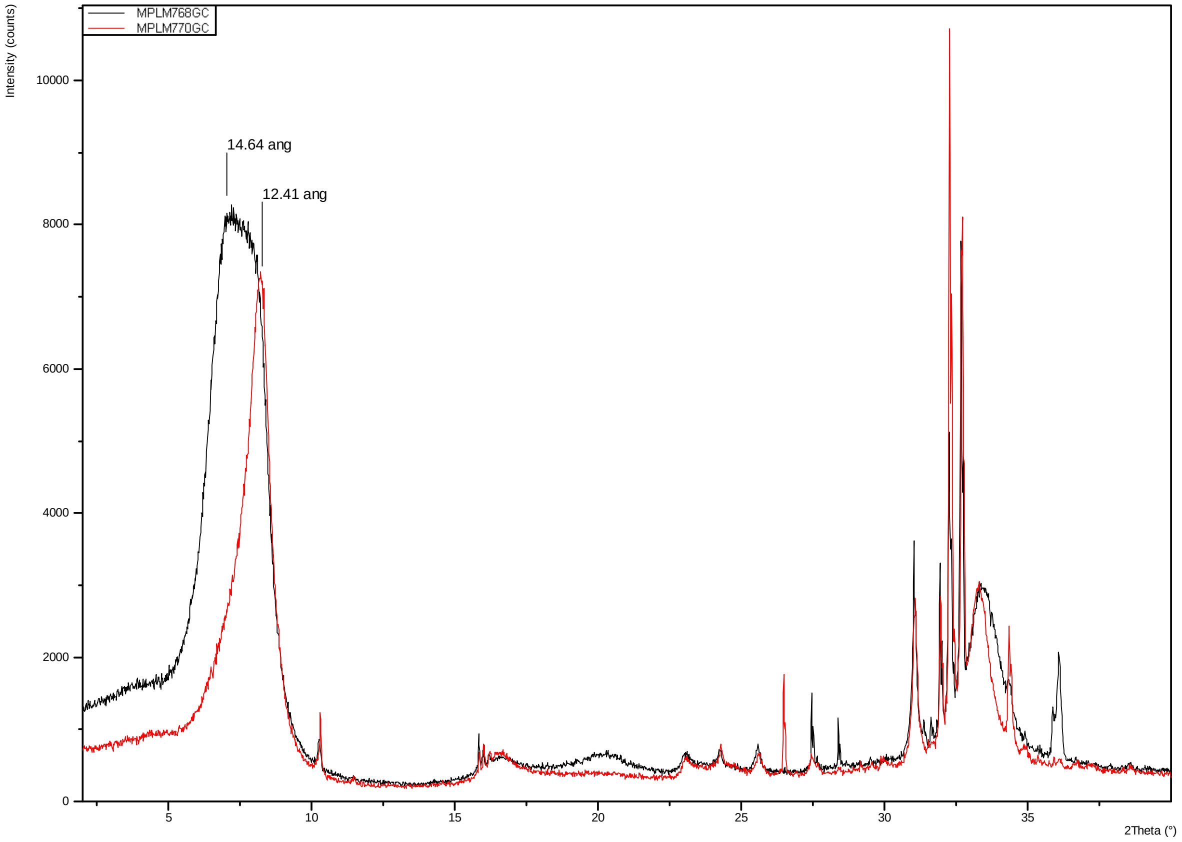

Figure 33. Comparison of air-dry, oriented mount X-ray diffraction traces for the two “unaltered” bentonite samples, samples MPLM768 and MPLM770.

Montmorillonite was identified from its characteristic c.17 Å spacing following glycol-solvation which collapses under heating to 550°C for 2 hours to an "illite-like" 9.6 Å d_{001} spacing. However, the air-dry d_{001} spacings for the two 'unaltered' bentonite samples appear different in character. Sample MPLM768 exhibits a broad, double peak with spacings of 14.64 and 12.98 Å while sample MPLM770 has a broad, single peak at 12.41 Å (Figure 33).

The montmorillonite d_{001} intensities can also be used to gain information on Fe substitution by measuring the scattering from the clay mineral octahedral sheet. The intensity ratio of the d_{002} to the d_{003} increases as the total number of electrons in the octahedral sheet increases. d_{002}/d_{003} values for the 'unaltered' bentonite subsamples are 1.18 (sample MPLM770) and 1.26 (sample MPLM768).

'Mica' was identified by its characteristic air-dry d_{001} spacing of c.10.0 Å which remains invariant after glycol-solvation and heating. A broad, low intensity superlattice peak most noticeable at c.31.4 Å on the ethylene glycol-solvated traces could not be definitively identified but may suggest the presence of trace amounts of an interlayered smectite-bearing phase.

4.2.2 "Altered" bentonite in contact with corroded steel wire corroded iron coupon

Bentonite "altered" or heavily stained by iron oxidation products associated with the corrosion of steel wires is represented by samples MPLM767B, MPLM771 and MPLM773B. "Altered" bentonite associated with the corrosion of iron coupon is represented by samples MPLM769 and MPLM772.

4.2.2.1 RANDOM ORIENTATION MOUNT XRD

Random orientation XRD analyses of the pervasively-stained bentonite in contact with the corroded steel wires indicate that it has a generally similar mineralogy to the "unaltered" bentonite. It is predominantly composed of a smectite-group mineral together with minor-to-trace amounts of quartz, feldspar (albite and K-feldspar) and cristobalite, accompanied in some cases by undifferentiated mica species ('mica', possibly including muscovite, biotite, illite, illite/smectite etc.), traces of pyrite and a zeolite-group mineral (probably heulandite). XRD analysis of the iron coupon-altered bentonite (samples MPLM769 and 772) indicate a similar mineralogy to the corroded wire-altered bentonite samples.

Further random orientation XRD analyses of the bentonite/corrosion products removed from the surface of the corroded wires in samples MPLM767B, MPLM771 and MPLM773B detected the presence of iron and aragonite along with the more typical bentonite mineral assemblage (Figure 34). Magnetite was also detected from the surface of the corroded wires from sample MPLM771 and sylvite was tentatively identified in a similar subsample from sample MPLM767B.

A mean d_{060} dimension of 1.4959 Å (range of values 1.4950 to 1.4966 Å) for the altered bentonite subsamples indicates that the smectite-group mineral is dioctahedral and most likely to be a montmorillonite species (Figure 35).

The montmorillonite in both the wire- and coupon-altered bentonite subsamples displays a composite d_{001} peak produced by peaks at c.15.1 Å and c.12.9 Å. In most cases the c.15.1 Å is the most intense peak and the 12.9 Å forms a less intense shoulder. However, in sample MPLM769, the 12.9 Å peak is more intense. The coupon-altered montmorillonites also show a slightly smaller mean spacing (14.78 Å) than the wire-altered samples (15.12 Å).

Both wire scraping subsamples exhibit a slightly larger single spacing for the montmorillonite d_{001} peak (mean spacing of c.15.8 Å, range of values 15.6 and 16.01 Å).

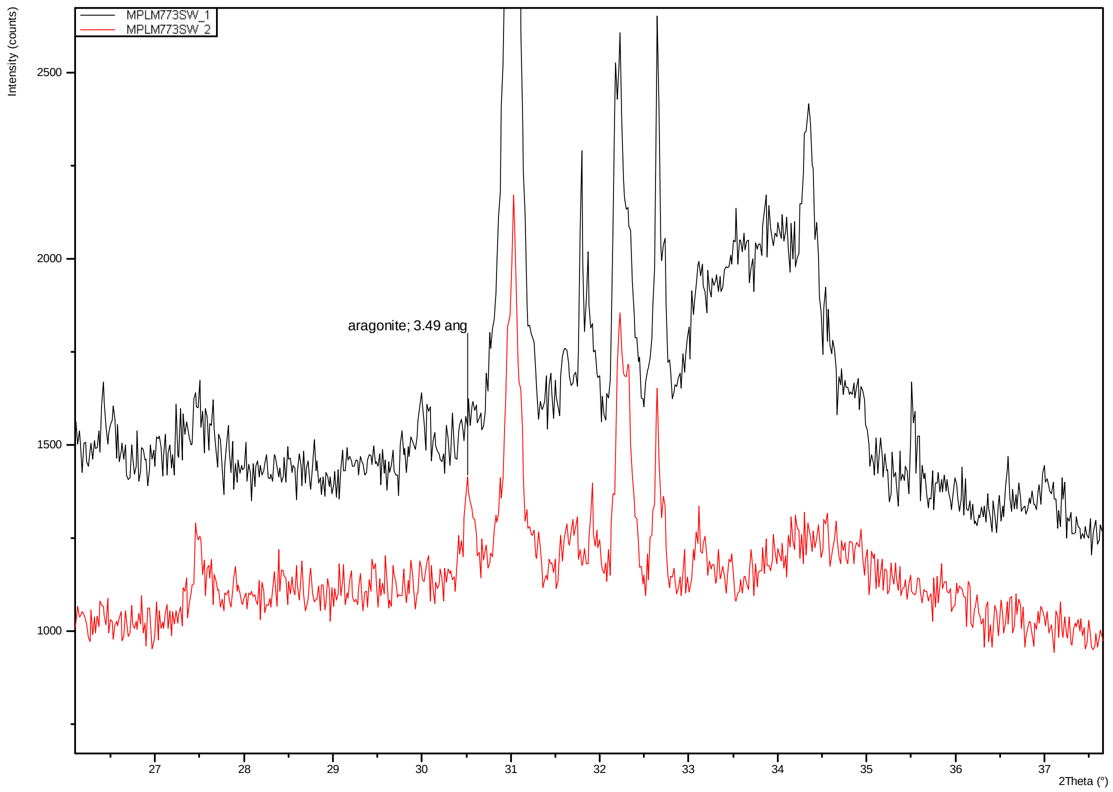

Figure 34. **Section of random powder mount XRD traces for "altered" bentonite material (black trace) and material removed from the surface of the corroding wire (red trace). Diagnostic peak position for the alteration product aragonite is shown, sample MPLM773B.**

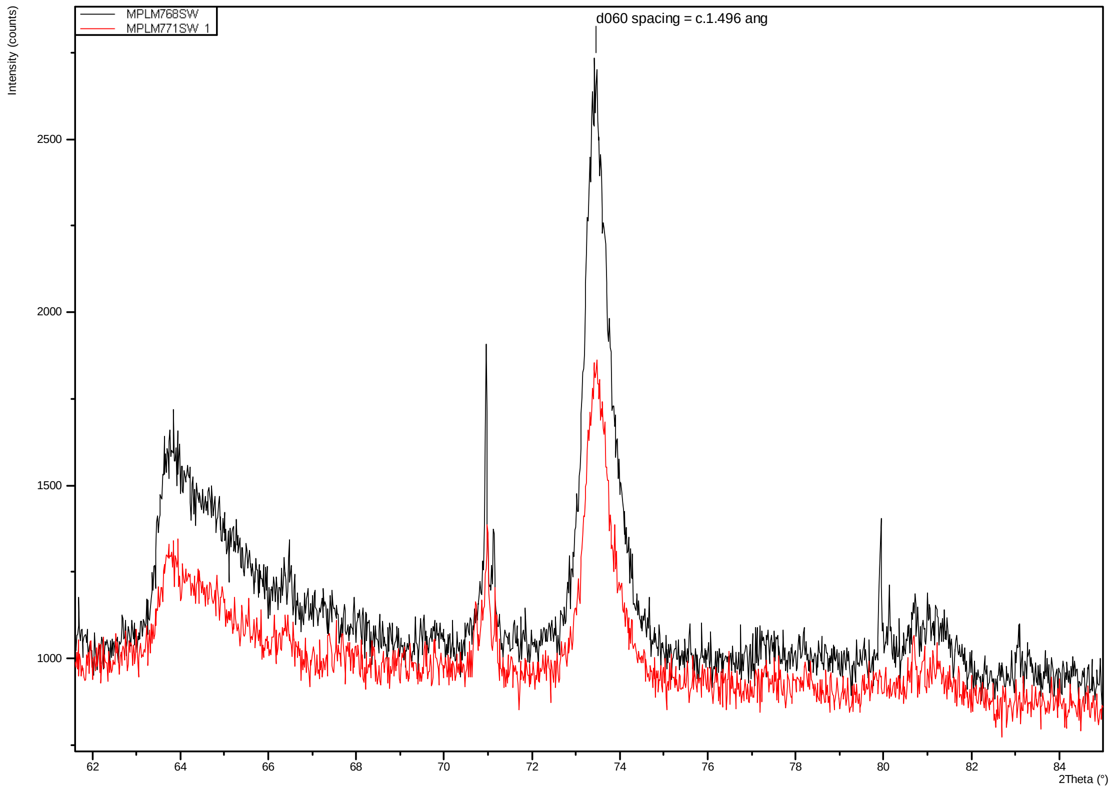

Figure 35. **High angle section of random powder mount XRD traces for "unaltered" bentonite material (black trace) and "altered" bentonite material (red trace) to illustrate a lack of change in the montmorillonite d_{060} spacing, samples MPLM768 and MPLM771.**

4.2.2.2 ORIENTED MOUNT XRD

Oriented mount XRD analyses confirm that the clay mineral assemblages of the corroded wire- and coupon-altered bentonite are dominated by montmorillonite with small quantities of 'mica'. As well as the non-clay minerals identified by random orientation XRD (see Section 4.2.2.1), a low intensity peak at 8.94 Å in the traces of all of the altered bentonite samples additionally suggest the presence of small quantities of a zeolite-group mineral, probably heulandite.

As for the 'unaltered' bentonite oriented mounts, montmorillonite was identified in the altered samples from its characteristic c.17 Å spacing following glycol-solvation which collapses under heating to 550°C for 2 hours to an 'illite-like' 9.6 Å d_{001} spacing. The air-dry d_{001} spacings for the altered bentonite samples again present a composite peak, this time with a more intense peak at c.12.5 Å and a less intense shoulder at c.14.4 Å (Figure 36). The shoulder appears very weak in sample MPLM773B.

The d_{002}/d_{003} values for the altered bentonite subsamples range from 1.14 to 1.33 (mean 1.24).

'Mica' was again identified by its characteristic air-dry d_{001} spacing of c.10.0 Å which remains invariant after glycol-solvation and heating. The very low intensity, superlattice peak noted in the 'unaltered' bentonite samples is also apparent in the altered samples, particularly at c.31.4 Å on the glycol-solvated trace.

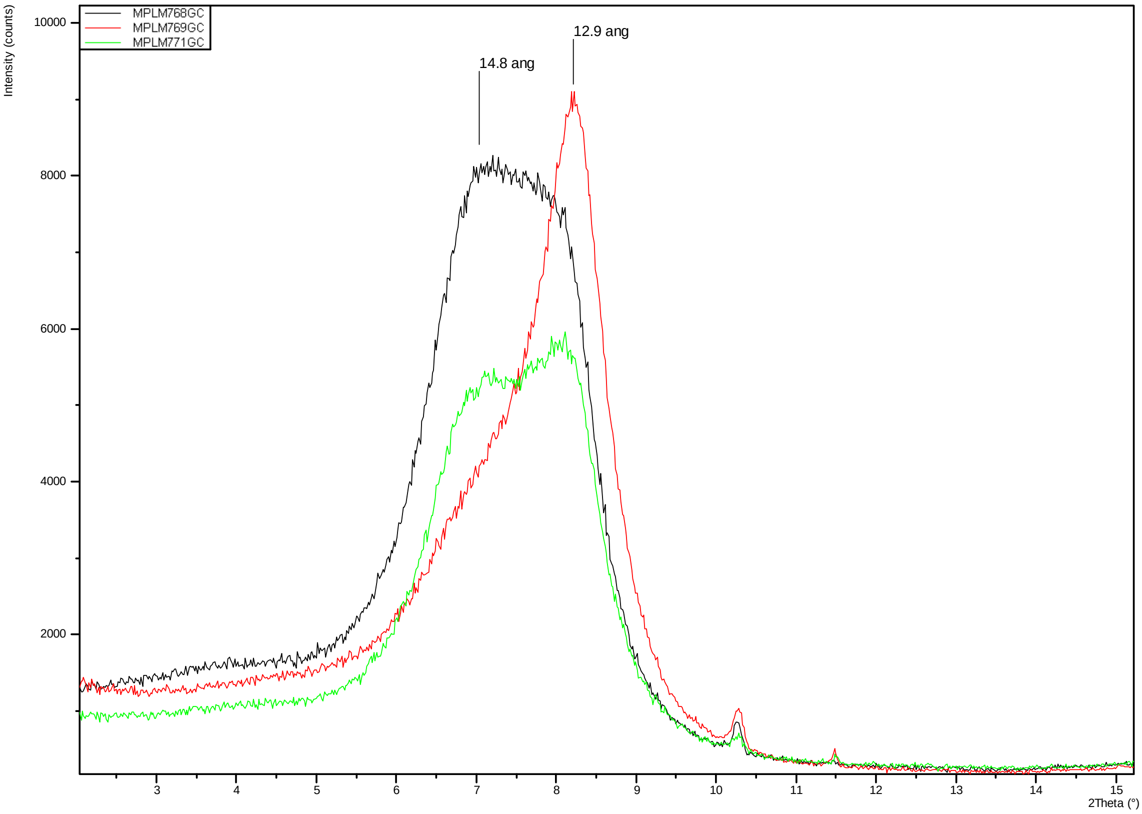

Figure 36. Low angle section of oriented mount XRD traces to illustrate the difference in the character of the montmorillonite d_{001} peak in "altered" bentonite materials (red and green traces) compared to the "unaltered" bentonite material (black trace), samples MPLM768, 769 and 771.

Table 5. Summary of random orientation mount XRD analyses

SERCO Sample Code	BGS Sample Code	Description	Subsample	Mineralogy	Montmorillonite d_{001} (Å)	Montmorillonite d_{060} (Å)
NFC1 Sample 1 CELL 1	MPLM767B	Bentonite with steel wires, pervasively stained with corrosion products	_1 wire altered	montmorillonite, quartz, K-feldspar, cristobalite, albite	15.25 & 12.98	1.4963
			_2 wire scraping	montmorillonite, quartz, iron, zeolite, aragonite, ?sylvite	15.60	nd
NFC4 Section 1 CELL4 “steel side /bentonite”	MPLM768	Grey bentonite disc	_1 ‘unaltered’	montmorillonite, quartz, K-feldspar, albite, cristobalite, calcite, mica, ?zeolite, ?pyrite	14.97 & 13.16	1.4969
NFC7 Section 1 CELL7 “carbon steel surface”	MPLM769	Grey bentonite disc with corrosion products on one side due to contact with iron coupon	_1 coupon altered	montmorillonite, quartz, cristobalite, albite, mica, K-feldspar, zeolite	14.63 & 12.94	1.4950
NFC13 Section 1 CELL 13 “cell end section”	MPLM770	Grey bentonite disc	_1 ‘unaltered’	montmorillonite, quartz, K-feldspar, albite, cristobalite, calcite, mica, pyrite	14.63 & 12.86	1.4965
NFC4 Section 1 CELL4 “wire /bentonite”	MPLM771	Bentonite with steel wires, pervasively stained with corrosion products	_1 wire altered	montmorillonite, quartz, cristobalite, albite, mica, K-feldspar, pyrite	14.83 & 12.81	1.4962
			_2 wire scraping	montmorillonite, quartz, mica, cristobalite, K-feldspar, magnetite, aragonite	16.01	nd
NFC7 Section 2 CELL7 “wire /bentonite”	MPLM772	Grey bentonite disc with corrosion products on one side due to contact with iron coupon	_1 coupon altered	montmorillonite, quartz, albite, mica, K-feldspar	14.57 & 12.86	1.4966
NFC13 Section 2 CELL 13 “wire /bentonite”	MPLM773B	Bentonite with steel wires, pervasively stained with corrosion products	_1 wire altered	montmorillonite, K-feldspar, cristobalite, albite	15.16 & 13.00	1.4952
			_2 wire scraping	montmorillonite, iron, quartz, cristobalite, aragonite, mica, K-feldspar, albite	16.40	nd

Table 6. Summary of oriented mount XRD analyses

SERCO Sample Code	BGS Sample Code	Description	Montmorillonite	
			d_{001} (Å)	XRD Peak Intensity Ratio* d_{002}/d_{003}
NFC1 Sample 1 CELL 1	MPLM767B	Bentonite with steel wires, pervasively stained with corrosion products	14.19 & 12.65	1.33
NFC4 Section 1 CELL4 “steel side /bentonite”	MPLM768	Grey bentonite disc	14.64 & 12.98	1.26
NFC7 Section 1 CELL7 “carbon steel surface”	MPLM769	Grey bentonite disc with corrosion products on one side due to contact with iron coupon	15.29 & 12.51	1.21
NFC13 Section 1 CELL 13 “cell end section”	MPLM770	Grey bentonite disc	12.41	1.18
NFC4 Section 1 CELL4 “wire /bentonite”	MPLM771	Bentonite with steel wires, pervasively stained with corrosion products	14.32 & 12.56	1.23
NFC7 Section 2 CELL7 “wire /bentonite”	MPLM772	Grey bentonite disc with corrosion products on one side due to contact with iron coupon	15.2 & 12.42	1.14
NFC13 Section 2 CELL 13 “wire /bentonite”	MPLM773B	Bentonite with steel wires, pervasively stained with corrosion products	12.59	1.30

Note:

d_{002}/d_{003} = XRD peak intensity ratio from glycol-solvated trace

4.3 CATION EXCHANGE AND EXCHANGEABLE CATION CHARACTERISTICS

The results of the CEC and exchangeable cation determinations for subsamples of “altered” (iron oxide-stained) bentonite from the bentonite-steel wire zone in each of the experiments, and background “unaltered” (green-grey) bentonite are summarised in Table 7.

The data show that Na is the dominant exchangeable cation (as expected in MX-80) but that significant exchangeable Ca and Mg are also present. Exchangeable K is present only as a very minor component of the exchangeable cation fraction. A very small amount of exchangeable Fe (0.5-1 meq/100g) was detected in two of the subsamples taken from the very heavily iron-stained alteration zones associated with corroded steel wires from experiments NFC1 and NFC13, but was not detectable in any of the other subsamples of “unaltered” or “altered” bentonite. Exchangeable Mn was not included in the analyses undertaken by Milodowski et al. (2007) during Phase 1 but it was included here in Phase 2 (at the request of Serco Assurance). However, it was found to be below detection limits (<0.5 meq/100g) in both “altered” and “unaltered” bentonite samples.

The CEC determined by magnesium sulphate titration is consistently lower than the sum of the exchangeable cations determined by ICP-AES following compulsive displacement of exchangeable cations by Ba. Although the standard CEC analysis method (Bascomb, 1964) uses a barium chloride solution buffered at pH 8.1 with triethanolamine, which is intended to inhibit the dissolution of any carbonate minerals that might be present, it seems likely that this is not completely effective. Other BGS investigations have similarly found that the method gives an excess of exchangeable cations compared to that expected from the titrimetric determination of CEC. The excess of exchangeable cations observed is most probably due to either: excess Ca derived from partial dissolution of calcium carbonate, which mineralogical and petrographical analysis shows is present in the NF-PRO materials both as original calcite or secondary aragonite (see Sections 4.1 and 4.2); or, excess Na derived from residual NaCl porefluid. Multivariate statistical analysis of the sequential chemical extraction (CISED) data also suggests that there is a component of readily-solubilised (leachable) Na derived from residual porefluid (see Section 4.4). Although it was not identified by mineralogical or petrographical observations, the CISED analysis (Section 4.4) indicate that gypsum might potentially be present, which (if correct) would also provide a relatively easily leachable source of Ca that might contribute to an excess of Ca in exchangeable cation data.

The Phase 1 analyses (Milodowski et al., 2007) superficially appeared to show very subtle differences in the CEC and exchangeable cation chemistry between the background “unaltered” bentonite and bentonite from the zone of steel wire alteration. However, it was pointed out by Milodowski et al. (op. cit.) that the dataset was very small, and that any conclusions drawn from these results should be treated cautiously. The Phase 2 results, presented in Table 7, show no systematic differences in CEC or exchangeable cations between the “unaltered” and “altered” bentonite. The variations observed between different subsamples of “unaltered” bentonite are comparable to those seen within the “altered” material taken from adjacent to corroding steel wire. In the light of these results, the small changes observed in CEC and exchangeable Na and Ca observed during Phase 1 (Milodowski et al., 2007) may also be insignificant, and within the “experimental noise” or primary heterogeneity of the bentonite samples.

The altered bentonite was sub-sampled at much too coarse a scale to realistically examine changes in the CEC and exchangeable cation characteristics within the alteration haloes observed during petrographical analysis (Section 4.1). “Altered” bentonite material taken for CEC and exchangeable cation analysis was sub-sampled on the broad basis of the colour change (iron staining), whereas petrographical evidence showed that the most significant mineralogical changes were taking place within narrow zones that were < 0.5 mm wide around the corroding steel wires. The alteration zones are far too small to analyse using the current CEC and exchangeable cation methodology, which requires between 0.1 and 1 g of sample.

Table 7. Cation exchange capacity (by titration) and exchangeable cations (determined by ICP-AES) data for reacted bentonite samples

Serco sample code	BGS sample code	CEC by titration	Exchangeable cation analysis by ICP-AES						
			Ca	Fe	Mn	Mg	Na	K	Total
		meq/100g							
NFC1 Sample 1 CELL 1 “unaltered”	MPLM767A	74.1	23	<0.5	<0.5	12	48	1	84
NFC1 Sample 1 CELL 1 “altered”	MPLM767B	82.0	26	0.5	<0.5	12	59	2	99.5
NFC13 Section 1 CELL 13 “unaltered”	MPLM770	79.2	19	<0.5	<0.5	10	78	1	108
NFC4 Section 1 CELL 4 “altered”	MPLM771	84.9	26	<0.5	<0.5	14	61	2	103
NFC13 Section 2 CELL 13 “unaltered”	MPLM773A	82.3	15	<0.5	<0.5	9	85	2	111
NFC13 Section 2 CELL 13 “altered”	MPLM773B	79.6	18	1	<0.5	7	85	2	113
Serco sample code	**BGS sample code**		**Ca**	**Fe**	**Mn**	**Mg**	**Na**	**K**	
			mg/kg						
NFC1 Sample 1 CELL 1 “unaltered”	MPLM767A		4524	<140	<5	1434	10984	540	
NFC1 Sample 1 CELL 1 “altered”	MPLM767B		5294	142	<5	1479	13521	722	
NFC13 Section 1 CELL 13 “unaltered”	MPLM770		3771	<140	<5	1161	17983	402	
NFC4 Section 1 CELL 4 “altered”	MPLM771		5278	<140	<5	1677	14011	704	
NFC13 Section 2 CELL 13 “unaltered”	MPLM773A		3040	<140	<5	1038	19542	624	
17b	MPLM773B		3655	279	<5	792	19598	608	

Note:

*concentration data for exchangeable cations are presented both as meq/100g and in mg/kg

4.4 SEQUENTIAL CHEMICAL EXTRACTION ANALYSIS

4.4.1 Data Processing

The data from the deionised water extractions and the first 0.01 M Aqua Regia extract were not used due to difficulties in separating fines from the extraction solution. The data processing was carried by combining the extraction data (excluding the samples as previously described) for samples MPLM767B, MPLM770, MPLM771, MPLM773 and a duplicate extraction of MPLM771. The element data used for each extract was Al, As, B, Ba, Ca, Co, Cr, Cu, Fe, K, Mg, Mn, Na, Ni, P, Pb, S, Si, Sr and Zn, giving rise to data matrix consisting of 55 rows (the extractions) and 20 columns (the elements). Sample MPLM770 is a 'clean' bentonite containing no steel wire. The remaining samples all contained steel wire. Prior to the extraction metallic Fe was removed from the sample by magnetic separation.

The data processing identifies distinct physico-chemical components in the bentonite samples identified by their chemical composition and their ease of extraction.

The processing identified 11 components. The name of each component is made up of those elements that make up more than 10% of its composition (listed in order of magnitude). The error bars on the profiles are derived from the root mean square fit of the modelled data to the original data set. Less significance should be given components whose error bars are large compared to the total amount of material extracted. The component names and the tentative assignments, based on the acid strength at which the component was extracted and mineralogical knowledge of the sample, are given in Table 8.

Table 9 summarises which group of extract numbers are associated with which samples and the acid extraction concentrations associated with each extract.

Table 8. Component names and tentative assignments

Component Name	Tentative Assignment
Na1	Modified cation exchangeable (after reaction with steel wire)
Ca- Mg	Carbonate
Fe1	Amorphous oxyhydroxide (poorly crystalline)
Na- Ca	Natural cation exchangeable
Fe2	Natural + synthetic crystalline Fe oxides (magnetite and ferric oxides)
S- Ca	Gypsum
Si- Fe-Al	Dissolution of clay lattice components
Al- P- Ca	Phosphate (apatite, crandallite)
Fe- Ca- Mg	Possibly from the dissolution of clay lattice components (cf. Milodowski et al., 2007)
Na2	Residual porewater
Fe-Al- Si- Ca	Clay

Table 9. Relationship between extract number, acid strength and sample name

Extract no.	Acid concentration	Sample	Extract no.	Acid concentration	Sample
1	0.01M	MPLM767B	28	0.5M	MPLM771
2	0.05M	MPLM767B	29	0.5M	MPLM771
3	0.05M	MPLM767B	30	1.0M	MPLM771
4	0.1M	MPLM767B	31	1.0M	MPLM771
5	0.1M	MPLM767B	32	5.0M	MPLM771
6	0.5M	MPLM767B	33	5.0M	MPLM771
7	0.5M	MPLM767B	34	0.01M	MPLM773
8	1.0M	MPLM767B	35	0.05M	MPLM773
9	1.0M	MPLM767B	36	0.05M	MPLM773
10	5.0M	MPLM767B	37	0.1M	MPLM773
11	5.0M	MPLM767B	38	0.1M	MPLM773
12	0.01M	MPLM770	39	0.5M	MPLM773
13	0.05M	MPLM770	40	0.5M	MPLM773
14	0.05M	MPLM770	41	1.0M	MPLM773
15	0.1M	MPLM770	42	1.0M	MPLM773
16	0.1M	MPLM770	43	5.0M	MPLM773
17	0.5M	MPLM770	44	5.0M	MPLM773
18	0.5M	MPLM770	45	0.01M	MPLM771d
19	1.0M	MPLM770	46	0.05M	MPLM771d
20	1.0M	MPLM770	47	0.05M	MPLM771d
21	5.0M	MPLM770	48	0.1M	MPLM771d
22	5.0M	MPLM770	49	0.1M	MPLM771d
23	0.01M	MPLM771	50	0.5M	MPLM771d
24	0.05M	MPLM771	51	0.5M	MPLM771d
25	0.05M	MPLM771	52	1.0M	MPLM771d
26	0.1M	MPLM771	53	1.0M	MPLM771d
27	0.1M	MPLM771	54	5.0M	MPLM771d
			55	5.0M	MPLM771d

Figure 37 summarise the extraction profiles of the 11 components. The extracts 1 to 55 are shown on the *x*-axis. Reading along the *x*-axis from left to right, extraction profiles for MPLM767B, MPLM770, MPLM771, MPLM773 and a duplicate extraction of MPLM771, respectively, are observed with increasing acid concentration within each profile. The *y*-axis of each of the plots gives the total solids extracted in mg kg^{-1} for the component in question. The composition of the 11 components is given in Table 10.

Examination of Figure 37 shows that the duplicate extracts for sample MPL771 give similar extraction profile shapes and magnitude showing that the extraction methodology is reproducible.

Two of the components only appear in the samples containing steel wire and have probably been formed due to its presence. These are Na1 and Fe1. Table 10 shows that Component Na1 is predominantly Na (c.78 %) and Figure 37 shows that it is extracted by the low concentration acid extractants. A similar component, again predominantly Na and extracted at low acid concentrations also exists (Na2 in Table 10 and Figure 37) appears in all samples. The main difference between the two components is that Na1 contains higher proportions of Ca, Fe, K and Mg (Table 10). This additional Na component is therefore likely to be derived from ion exchangeable Na derived from altered bentonite in the samples reacted with steel wire.

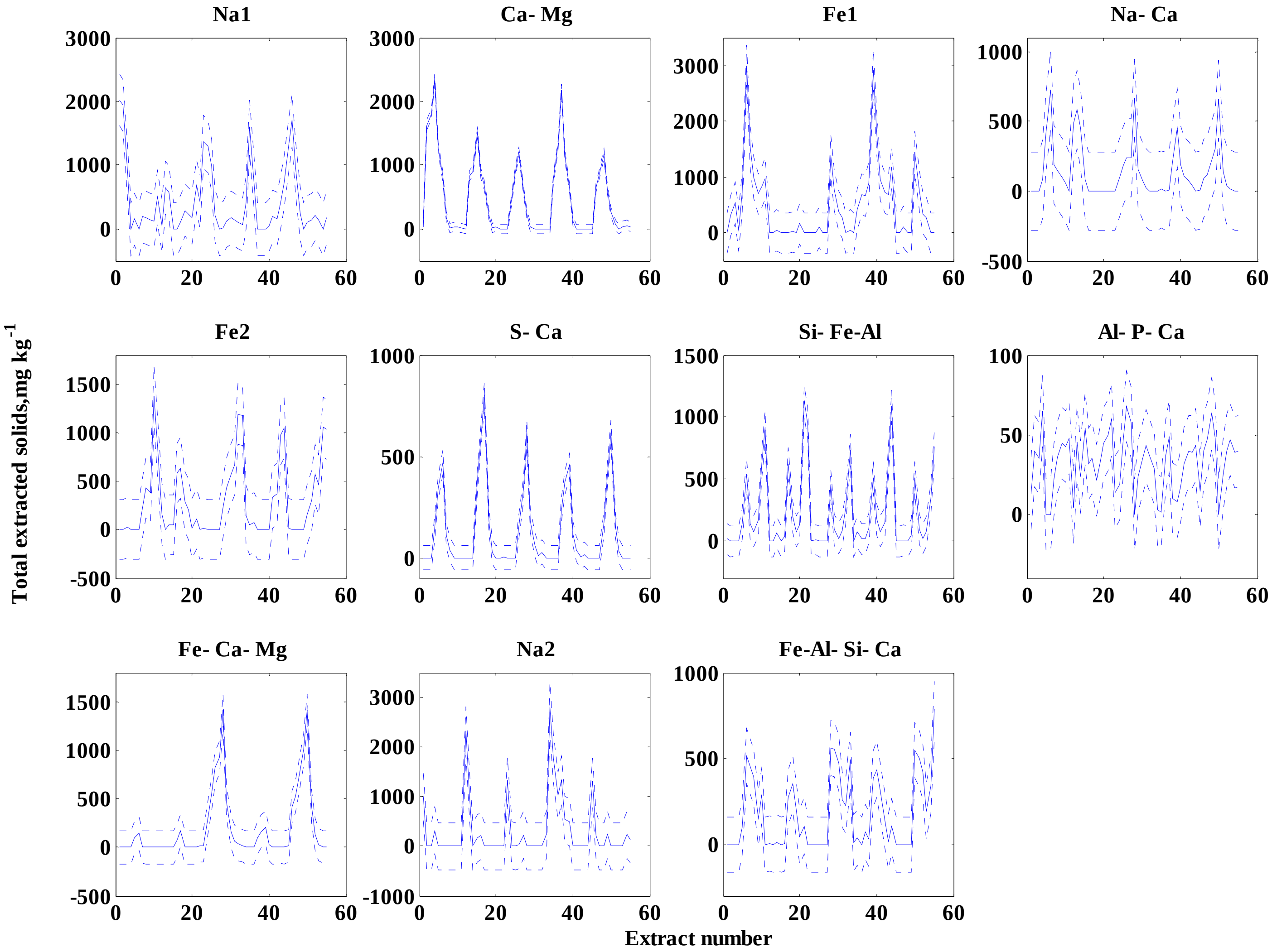

Figure 37. Component profiles for the 11 extracted components (error range for data shown by dotted lines)

Table 10. Percentage composition of the 11 geochemical components

Element	Components									
	Na1	**Ca-Mg**	**Fe1**	**Na-Ca**	**Fe2**	**S- Ca**	**Si- Fe-Al**	**Al-P-Ca**	**Fe-Ca-Mg**	**Na2**	**Fe-Al-Si-Ca**
Al	0.00	0.00	0.00	0.00	0.00	5.15	13.16	46.60	0.00	0.00	26.46
As	0.02	0.00	0.00	0.01	0.14	0.14	0.02	0.48	0.00	0.00	0.01
B	0.02	0.00	0.14	0.04	0.09	0.00	0.03	2.13	0.00	0.00	0.12
Ba	0.01	0.51	0.00	0.17	0.00	0.36	0.28	7.63	0.13	0.00	0.21
Ca	7.78	62.10	0.00	26.22	0.00	21.17	0.00	18.00	30.29	0.00	10.85
Co	0.00	0.00	0.00	0.00	0.00	0.01	0.00	0.10	0.00	0.00	0.00
Cr	0.00	0.00	0.01	0.01	0.00	0.03	0.02	0.12	0.00	0.00	0.02
Cu	0.00	0.04	0.03	0.00	0.00	0.08	0.00	0.13	0.02	0.01	0.01
Fe	6.31	7.38	95.58	0.00	80.11	0.00	30.96	0.00	43.09	0.00	41.98
K	5.14	1.38	0.00	0.09	0.00	0.00	0.00	0.00	1.07	2.06	0.88
Mg	2.19	16.48	0.00	4.65	0.00	2.19	2.75	0.00	12.34	0.00	5.38
Mn	0.08	0.95	0.10	0.09	0.06	1.88	0.10	0.00	0.00	0.01	0.23
Na	77.70	0.00	0.00	52.47	7.00	0.00	0.00	0.00	0.36	89.94	0.00
Ni	0.00	0.04	0.00	0.00	0.00	0.00	0.00	0.12	0.29	0.00	0.04
P	0.01	0.00	0.22	5.15	1.22	0.29	0.00	19.48	0.00	0.00	0.00
Pb	0.00	0.16	0.00	0.05	0.02	1.37	0.00	1.66	0.00	0.00	0.03
S	0.56	0.00	3.68	4.14	1.73	67.07	5.75	0.00	4.29	0.00	0.00
Si	0.00	9.45	0.00	6.89	9.63	0.00	44.51	0.00	6.71	7.95	13.38
Sr	0.19	1.52	0.19	0.03	0.00	0.00	0.00	0.14	1.42	0.02	0.40
Zn	0.00	0.00	0.05	0.00	0.00	0.27	2.41	3.42	0.00	0.00	0.00

Table 10 shows that the Fe1 component is predominantly Fe (c. 96 %) and Figure 37 shows it extracted in the 0.1M to 0.5M acid extraction range. This component is thought to be amorphous oxyhydroxide (poorly crystalline) derived from corrosion of the embedded steel wire. Table 10 also shows that there is another Fe dominated component (Fe2) which has been plotted separately in Figure 38 along with the Fe1 component extraction profiles. The Fe2 component is extracted at higher acid strengths and is thought to be derived from crystalline Fe oxides. In the sample with no steel wire (MPLM770) the Fe2 component is thought to be derived from primary very crystalline magnetite or ilmenite present originally in the bentonite but may also include crystalline magnetite formed as a corrosion product of the steel (which was identified by XRD in one sample; MPLM771). In the samples containing steel wire Figure 38 shows that the Fe2 component starts to be extracted at about the same acid strength as the background sample but has an additional ‘peak’ which continues to increase up to the highest acid strength. This alteration in shape suggests some of the poorly crystalline Fe oxyhydroxide from steel wire corrosion is being converted into more crystalline forms and adds to the existing natural background of crystalline Fe oxides.

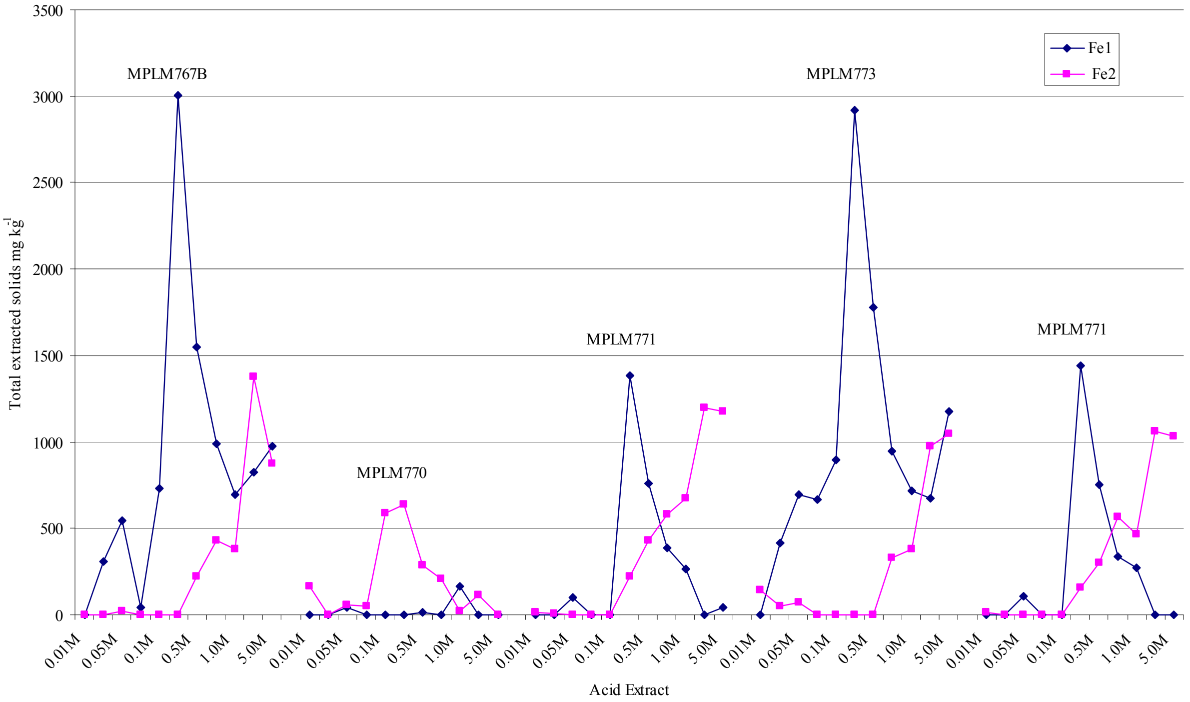

Figure 38. Extraction profiles of the Fe dominated components

Table 11. Mass distribution of Fe among the 11 components (mg/kg)

Sample	Component										
	Na1	Ca-Mg	Fe1	Na-Ca	Fe2	S-Ca	Si-Fe-Al	Al- P- Ca	Fe-Ca-Mg	Na2	Fe-Al-Si Ca
MPLM767B altered bentonite	389	610	9236	0	2655	0	814	0	107	0	797
MPLM770 background bentonite	201	373	213	0	1705	0	993	0	109	0	420
MPLM771 altered bentonite	283	257	2806	0	3440	0	517	0	2054	0	1080
MPLM773 altered bentonite	271	457	10406	0	2398	0	885	0	214	0	648
MPLM771 altered bentonite (duplicate)	316	276	2786	0	2890	0	578	0	2053	0	1169

Table 11 gives the mass distribution of the total extracted Fe between the eleven components for each bentonite sample given by the CISED modelling. The root mean square error on the modelled Fe values is ± 191 mg kg^{-1}. The total Fe extracted is the sum of the Fe in each of the components for a given sample.

The largest proportion of the Fe in most of the samples of altered bentonite can be accounted for by component Fe1, which is attributed to amorphous or poorly crystalline iron oxyhydroxide.

This component accounts for between 26 to 68 % of the Fe in the reacted bentonite, whereas only 5% of the Fe in the background bentonite can be attributed to amorphous or poorly crystalline iron oxyhydroxide.

Crystalline iron oxides (component Fe2) also accounts for a significant proportion of the Fe in the reacted bentonite: between 15 to 33 % of the total Fe. Part of this will include primary magnetite and ilmenite that were originally present in the MX-80 bentonite. However, this will also include crystalline magnetite identified by XRD that was produced as a corrosion product of the steel wires. In the unaltered bentonite, Fe2 is the major Fe component, comprising 42% of the total Fe.

The 'Ca-Mg component' is likely to be derived from dissolution of carbonates as it is dissolved at relatively low acid concentrations. It is probably contributed by calcite originally present in MX-80 bentonite and by aragonite formed as a by-product of the wire corrosion. In the background unaltered bentonite this may contribute about 9 % of the total Fe but carbonates would appear to host only a very small proportion (2.4 to 4.2 %) of the total Fe in the altered bentonite.

The sequential extraction data also appear to indicate that a significant proportion of the Fe is associated with the silicate minerals (as inferred by the Fe content of components Si-Fe-Al, Fe-Ca-Mg and Fe-Al-Si-Ca). The leaching of these components at higher acid strengths in the CISED extraction sequence is interpreted to indicate that they represent components released by the breakdown and dissolution of the silicate clay mineral lattice. If this is correct, then the CISED results in Table 11 would suggest that between 11 to 38 % of the total Fe in the altered bentonite is hosted within clay mineral/silicate components. This would appear to be compatible with the petrographical observations (Section 4.1) which showed significant Fe-enrichment of the silicate clay matrix that could not be accounted for by discrete iron oxides. The unreacted bentonite would also appear to have about 40 % of the total Fe hosted by the silicate minerals, although in this case the total amount of Fe is the unaltered bentonite is much lower (Appendix 1).

The association of Fe with Na1 component may indicate that between 1.8 to 3.1 % of the total Fe is incorporated within the cation exchange sites within the altered clay. An alternative explanation is that this might represent soluble $FeCl_2$ or $FeCl_3$ that potentially might have formed during drying of residual saline porewater containing iron in solution from the corroding metal . The data also indicate that up to 5 % of total Fe in the unaltered bentonite is present in exchangeable cation sites. At first glance, this would appear to indicate that some of the Fe from the corroding wires has possibly been mobilised into the interlayer sites in smectite. However, these observations are in disagreement with the results of direct exchangeable cation analysis determined by compulsive displacement with barium (Section 4.3), which showed that there is little or no Fe in cation exchange sites. Consequently, it seems more likely that this Fe is being contributed by minor dissolution other phases during the early stages of the CISED leaching process, and as such the results for Fe in component Na1 should be regarded with caution.

5 Discussions and conclusions

5.1 BACKGROUND MINERALOGICAL CHARACTERISTICS OF MX-80 BENTONITE

XRD and petrographical analysis in this study reveals that the “unaltered”, grey bentonite shows a similar composition to that previously described for MX-80 (e.g. Madsen, 1998). It is predominantly composed of a smectite-group mineral together with minor-trace amounts of quartz, cristobalite, feldspar (albite and K-feldspar), calcite, undifferentiated mica species (“mica”, possibly including muscovite, biotite, illite, illite/smectite etc) and pyrite (Figure 32). Small quantities of a zeolite-group mineral, probably heulandite were also detected.

However, in comparison to the “unaltered” grey bentonite analysed in the Phase 1 study (Milodowski et al., 2007), the samples from the present study do not contain any halite. As the halite detected in the previous study was thought to result from the evaporation of the experimental brine solution, this may indicate a difference in the chemistry of experimental solution used in the second experiment.

Detailed petrographical analysis shows that the feldspars and apatite are present as angular silt and sand sized grains, which show little alteration. Petrographical analysis also identified trace amounts of calcite disseminated throughout the bentonite. It occurs as irregular patches and angular grains within hydrated “clasts” of the original granular bentonite, and is seen in both background “unaltered” bentonite samples and samples of “altered” bentonite stained by iron oxide alteration. The calcite shows no evidence for dissolution in the reacted bentonite samples.

As in Phase 1 (Milodowski et al., 2007), pyrite was observed to be present as framboidal (spherical) microcrystalline aggregates of sub-micron crystallites. The pyrite appeared to be fresh in both the background “unaltered” and “altered” bentonite samples.

5.2 BENTONITE ALTERATION CHARACTERISTICS

5.2.1 Clay mineral alteration

5.2.1.1 EVIDENCE FROM XRD

XRD analysis shows that the altered, pervasively-stained bentonite in contact with the corroded steel wires has a generally similar mineralogy to the “unaltered” bentonite. Analysis of corrosion/alteration products removed directly from the surface of the steel wires detected the presence of aragonite in samples MPLM767B, MPLM771 and MPLM773 (Figure 34), which was not found in the “unaltered” MX-80 bentonite suggesting that aragonite had formed during interaction of the steel wires and bentonite.

A mean d_{060} dimension of 1.4967 Å (range of values 1.4965 to 1.4969 Å) for the “unaltered” grey bentonite subsamples measured from random XRD mounts is comparable with that obtained for the first experiments (Milodowski et al., 2007) and indicates that the smectite-group mineral can be classified as dioctahedral and most likely is a montmorillonite species. A similar mean d_{060} dimension of 1.4959 Å and range of values (1.4950 to 1.4966 Å) for the altered bentonite subsamples indicates that the smectite-group mineral has remained dioctahedral following reaction (Figure 35).

Random mount measurements indicate that the montmorillonite in the “unaltered” grey bentonite subsamples displays a composite d_{001} peak with a maxima at c.14.9 Å and a prominent high angle shoulder at c.13.0 Å. As discussed in Section 4.2.1.1, such a peak profile may suggest the presence of a mixture of exchangeable cations. The c.14.9 Å spacing may suggest the predominance of divalent (Ca/Mg) cations while the c.13.0 Å shoulder may suggest the additional presence of some monovalent (Na/K) interlayer cations. These spacings differ to those obtained for the 'unaltered' bentonite in the first experiments where a mean d_{001} spacing of c.12.74 Å was indicated and a monovalent cation-dominated interlayer inferred (Milodowski et al., 2007). Alternatively the composite peak may reflect slight differences in the hydration state of the interlayer cations. Although the relative humidity of the XRD analyses was not controlled, the samples were run as a single batch following a similar preparation methodology and in an identical manner to the samples from the first experiments. This would tend to suggest that the composite peaks reflect a mixture of exchangeable cations in the montmorillonite rather than differences in the hydration of those cations. The results of exchangeable cation analysis support this conclusion, showing that although Na is the dominant species, significant Ca is also present as an exchangeable cation.

The montmorillonite in the wire-altered bentonite subsamples displays a slightly larger divalent cation mean d_{001} spacing of c.15.08 Å (range of values 14.83 to 15.25 Å) compared to that in the "unaltered" bentonite. Such an increase in the smectite c-axis dimension may indicate the replacement of some of the divalent (Ca/Mg) interlayer cations with larger divalent cations. As the experiment involves corrosion of steel wires, these divalent cations may be Fe. Spacings for the monovalent cation spacings appear similar in the wire-altered and 'unaltered' bentonite samples. The montmorillonite from the iron coupon-altered bentonite shows approximately similar spacings to those obtained from the 'unaltered' bentonite.

Subsamples taken from the surface of the corroding wires have a mean d_{001} spacing of c.16.0 Å. This would seem to suggest that the montmorillonite in close proximity to the corroding wires have undergone further divalent ion (?Fe) exchange with the originally monovalent/divalent interlayer cations.

The results obtained for oriented mount XRD analyses are complicated and difficult to explain. The oriented clay XRD mounts for the montmorillonite in the two "unaltered" samples shows different characteristics. In sample MPLM768, the montmorillonite produces a broad, double peak with spacings of 14.64 and 12.98 Å while sample MPLM770 has a broad, single peak at 12.41 Å (Figure 2).

Similarly, the oriented clay mounts for the wire-altered bentonite samples (MPLM767B, MPLM771 and MPLM773) show different characteristics. Samples MPLM767B and MPLM771 show a composite peak with two approximately equally intense maxima at c.14.2 and 12.6 Å. Sample MPLM773B has a single maxima at 12.6 Å.

Both the coupon-altered bentonite samples (MPLM769 and MPLM772) show similar oriented XRD patterns with composite peaks produced by maxima at c.12.5 Å and indistinct shoulders at c.15.2 Å.

As was noted for the first experiments (Milodowski et al., 2007), it is unclear why the oriented mount d_{001} spacings are consistently smaller than the same spacings measured on the random mounts of similar samples. A possible reason for such behaviour might be that further cation exchange has occurred between the montmorillonite and salts precipitated on its surface during the hydration necessary for oriented mount preparation and so reduced the measured d_{001} spacing. Alternatively, the oriented mounts may have achieved a more stable, dehydrated state following overnight air-drying prior to analysis whereas the random mounts were run immediately after preparation to prevent further oxidation effects.

d_{002}/d_{003} values for the montmorillonite in the "unaltered" bentonite subsamples range from 1.18 to 1.26 (mean 1.22) while those for the altered bentonite subsamples show very slightly increased values of 1.14 to 1.33 (mean 1.24). Such a marginal increase may suggest an increase in the total number of electrons in the octahedral sheet of the "altered" bentonite, possibly as a result of Fe substitution.

The broad, low intensity superlattice peak at c.21.8 Å on the air-dry XRD trace which expands to c.31.4Å on glycolation could not be definitively identified but is present in both "unaltered" and altered subsamples. It may suggest the presence of trace amounts of an interlayered smectite-bearing phase.

5.2.1.2 PETROGRAPHICAL AND GEOCHEMICAL EVIDENCE

Detailed BSEM-EDXA petrography revealed that significant interaction between Fe released as a result of the corrosion of steel wires or iron coupons and the adjacent clay matrix of the enclosing bentonite, in all four Serco Assurance experiments (NFC1, NFC4, NFC7 and NFC13).

The reacted bentonite recovered from Experiment NFC1 showed very similar alteration characteristics, associated with the corrosion of steel wire, to those seen in the earlier Phase 1 investigation (Milodowski et al., 2007). Both BSEM images and EDXA microchemical mapping show an alteration halo around the corroded steel wires in the bentonite. The bentonite within this halo has significantly enhanced concentrations of Fe (up to 80 wt. % Fe) immediately adjacent to the corroding metal decreasing to background levels at distances of between 600 to 1000 μm from the metal Smart et al. (2006) also recorded a slight enhancement of Fe in bentonite adjacent to corroding wires in early preliminary investigations. These authors observed iron enrichment over distances varying between 0.1 and 1.5 mm from the metal. However, the alteration haloes were much less obvious and more diffuse than those observed in the experiments in this study. The reacted bentonite from experiments NFC4, NFC7 and NFC13 also displayed very pronounced alteration haloes of Fe-enriched clay matrix around corroded steel wires, although the alteration in these three experiments was found to be more complex than in NFC1. In all four experiments these alteration zones were much more strongly developed and thicker than in the earlier experiments reported from Phase 1 (Milodowski et al., 2007), with the thickest alteration zones seen in Experiment NFC4 where the alteration extended up to 2 mm from some of the wires. Similar but less well developed alteration and Fe enrichment of the bentonite was observed around the two corroded iron coupons examined from experiments NFC4, NFC7 and NFC13. The greatest penetration of Fe into the bentonite matrix occurs along hairline microfractures that radiate outwards from the corroding metal.

Close examination shows that whilst a thin layer of discrete iron oxide or iron oxyhydroxide (these cannot be differentiated by BSEM-EDXA) may be present as very fine coatings on the surface of the corroding metal and lining the walls of the microfractures, no discrete iron oxide phase (other than primary particles of accessory magnetite and ilmenite originally present bentonite) could be discerned in the Fe-enrich clay matrix within the limits of spatial resolution of the BSEM petrographical analysis (i.e. better than 0.1 μm). The matrix clay particles within the Fe-enriched halo appear brighter under BSEM than in the unaltered clay, suggesting that the clay minerals have become enriched in Fe. This is consistent with the tentative interpretations from the CISED sequential chemical extraction analyses, which suggest that from 11 to 38 % of the total Fe in the altered bentonite is associated with the clay mineral lattice. However, CISED also suggest that a very significant proportion of the Fe present in the altered clay matrix is present as amorphous or poorly crystalline iron oxyhydroxide (26 to 68 % of the total Fe) and as crystalline iron oxide (15 to 33 % of the total Fe). Some of the crystalline iron oxide will be due to primary magnetite and ilmenite (and also pyrite, which would also be dissolved at high acid strengths in the CISED sequence) originally present in the MX-80 bentonite but part of this will be attributable to crystalline magnetite formed by the corrosion of steel.

Petrographical analysis revealed that the alteration of bentonite around the corroding steel wires in NF-PRO experiments NFC4, NFC7 and NFC13 was more complex than that seen in experiment NFC1 and the earlier experiments studied in Phase 1 by Milodowski et al. (2007) or reported previously by Smart et al. (2006). In these experiments, a Mg-Fe-rich aluminosilicate was observed to have formed as a significant alteration product of the clay matrix within the Fe-rich alteration haloes. EDXA microchemical mapping did suggest some slight Mg enhancement in the reacted bentonite from NFC1 but no discrete Mg-rich phase was detected. The reaction product in NFC4, NFC7 and NFC13 contained up to 20 wt. % Mg in some alteration zones around the corroded steel wires. Such high Mg concentrations might be expected if the alteration products included phases such as saponite, Mg-rich chlorite or talc. However, the alteration product also includes significant Fe and Al, which suggests that the alteration product is not simply saponite or talc. Unfortunately, the XRD analyses have been unable to help identify this alteration product. This is possibly because the material analysed by XRD was subsampled on too coarse a scale and will effectively have been diluted with largely unaltered bentonite from outside of the main alteration zones around the wires. Petrographical relationships show that the Mg-rich "clay mineral" alteration product appears to have formed relatively early in these experiments, and has been at least partially replaced by more Fe-rich alteration products as reaction progressed.

The petrographical evidence clearly demonstrates that the clay mineralogy of the bentonite has been significantly altered in narrow zones around the corroded steel wires. Whilst Mg may potentially have been derived from the "Allard" reference water used in experiment NFC4, in the case of NFC7 and NFC13 it could only have been derived from the breakdown of the bentonite itself since the porefluid only contained NaCl in these two experiments. Therefore, the indications are that the original dioctahedral montmorillonite has been broken down to produce a Mg-Fe-rich clay mineral or other aluminosilicate, or has been replaced by an Fe-rich clay mineral or aluminosilicate. However, further work is required to be able characterise these Fe-rich and Mg-rich aluminosilicate products. We therefore suggest that further analyses using transmission electron microscopy or analytical transmission electron microscopy should be carried out to try to refine the identification of these clay mineral alteration products. Geochemical modelling of mineral stability may also be useful in indicating which clay mineral species might potentially be forming during the experiments.

5.2.2 Other mineralogical alteration

Aragonite was detected by XRD in the altered bentonite material removed directly from the surface of the steel wires in these experimental residues. Although traces of calcite are present, aragonite was not detected in the 'unaltered' background bentonite material suggesting that aragonite has formed during interaction with the steel wires.

Detailed petrographical analyses reveal that the aragonite has formed as a result of Ca concentrating in the bentonite immediately adjacent to the corroding iron, and along the leading edge of diffuse fronts of Fe within the halo of altered bentonite around the steel wires. The aragonite occurs as thin, fine grained, alteration fringes or layers (10-30 μm thick) replacing or displacing the bentonite at the interface with the corroding steel, or fine acicular crystals that line open fractures within the bentonite that radiate from the corroding wire surface.

Since the porefluid used in the experiments did not contain Ca, and there is no petrographical evidence for the dissolution of discrete Ca minerals (calcite, apatite, feldspar) originally present in the bentonite, then, the Ca must have been derived from the exchangeable cation sites in the montmorillonite. Although MX-80 is described as a Na-saturated bentonite, the presence of a significant amount of exchangeable Ca is reported in the literature (Herbert and Moog, 1999; Bradbury and Baeyens, 2003; Carlson et al., 2006; Smart et al., 2006), and up to 4524 mg/kg Ca was recorded in this study from the background 'unaltered' bentonite. The petrographical evidence indicates that Fe from the corroding steel may have displaced the Ca^{2+} from the exchangeable cation interlayer sites in the montmorillonite. Although, exchangeable cation analyses of reacted bentonite indicate very little exchangeable Fe to be present. The pattern of Ca distribution shows that the Ca has concentrated in several bands, possibly representing different 'pulses' of alteration. Initially Ca has been displaced from bentonite at the interface with the steel, or migrated towards the corroding metal as Fe has diffused into the bentonite. In addition, later bands of aragonite formed as Ca^{2+} was displaced and concentrated at the leading edge of Fe diffusion fronts as they migrated further into the bentonite matrix. These observations are consistent with potential mechanism for bentonite alteration under anoxic conditions, described previously by Kamei et al. (1999) and Idemitsu et al. (2003), involving substitution of interlayer cations such as Na^+ and Ca^{2+} by Fe^{2+} produced by iron corrosion.

5.2.3 Change in cation exchange properties

The results from the earlier Phase 1 analyses of MX-80 bentonite recovered at the end of NF-PRO experiments NFC12, NFC16 and NFC17 tentatively indicated a very subtle decrease in CEC, Ca and Na within the altered steel-wire-bentonite zone in each experiment (Milodowski et al., 2007). However, this was not confirmed by the Phase 2 results from NF-PRO experiments, NFC1, NFC4, NFC13, which showed no consistent differences in exchangeable CEC or exchangeable cations (with the possible exception of Fe) between background “unaltered” bentonite and “altered” bentonite heavily impregnated with iron corrosion products. A very small amount of exchangeable Fe (0.5-1 meq/100g) was detected in “altered” bentonite associated with the very heavily iron-stained zones containing corroded steel wires from experiments NFC1 and NFC13, but was not detectable in the “altered” bentonite from experiment NFC4 nor in background “unaltered” bentonite. Exchangeable Mn was found to be below detection limits (<0.5 meq/100g) in all of the “altered” and “unaltered” bentonite samples examined.

As discussed in the Phase 1 report (Milodowski et al., 2007), these analyses represent the overall cation exchange characteristics of the bulk of the visually “altered” iron-stained bentonite zone, containing disseminated corroded steel wires. However, petrographical analyses clearly demonstrate that the most significant alteration effects in the clay matrix occur within the narrow alteration haloes around the corroding steel wire. Unfortunately, these are on too fine a scale to subsample for standard CEC and exchangeable cation analysis. Therefore, it is likely that any changes in CEC or exchangeable cation characteristics would have been extensively diluted by essentially unaltered MX-80 bentonite that would have comprised most of the samples analysed in each case. If changes in CEC and exchangeable cations are to be detected then refinement and development of the analytical technique is required to enable finer scale micro-sampling and analyses of very small subsamples (i.e. employing only a few milligrams) for CEC and exchangeable cations.

5.2.4 Bentonite shrinkage and swelling characteristics

Petrographical examination of the thin sections of bentonite from the steel wire-bentonite zone showed that the shrinkage behaviour of the clay matrix varied significantly between the altered and unaltered bentonite. This differential behaviour was also observed in the Phase 1 experiments (Milodowski et al., 2007). Shrinkage of the bentonite had occurred in two stages:

1. Early shrinkage of the clay matrix confined within the Fe-rich alteration haloes immediately adjacent to the corroding steel. This produced microfractures with apertures up to 50 µm, although in most cases, fracture apertures range between <0.5-10 µm. These fractures clearly formed during the coarse of the experiment, as they are closely associated with the enrichment of Fe in the clay walls and the precipitation of thin coatings of aragonite produced probably as a result of the displacement of exchangeable Ca^{2+} by Fe from the montmorillonite interlayer cation sites. Similarly, the precipitation of iron oxide coatings on the walls of these fractures also illustrates that these fractures formed in situ during the course of the experiments.
2. Later unmineralised microfractures cross cutting, and sometimes accentuating or re-utilising, the earlier formed microfractures. These most probably formed post-

experimentation, as a result of clay shrinkage during sample drying and epoxy-resin impregnation for thin section preparation.

The petrographical observations show that the altered bentonite that has been significantly enriched with Fe from steel corrosion, has a tendency to show significantly reduced shrinkage on sample drying than the unaltered bentonite. Conversely, this would suggest that the reacted and altered clay will also have less ability to swell on hydration with water. Although XRD indicates that the smectite in the reacted bentonite is dioctahedral, possibly the original montmorillonite may have been converted to Fe-rich dioctahedral smectite (e.g. nontronite) within the alteration haloes. Wilson (2006b) showed that one of the effects of altering montmorillonite to an Fe-rich smectite is to reduce its expandability. This may explain the shrinkage and reduction in expandability observed in this petrographical study of the altered bentonite from the NF-PRO experiments.

The early formed fractures may have represented potentially important pathways for gas and solute transport during the course of the experiments. The irreversible shrinkage of the bentonite, as a result of interaction with Fe released from corroding iron or steel may therefore be significant in evaluating the long-term behaviour of the bentonite seal and the transport of gas and solutes around corroding waste canisters emplaced in bentonite backfill.

5.3 STEEL CORROSION

Magnetite was detected by XRD as a surface corrosion product in sample MPLM771. However, the observation that the iron oxide corrosion products from all three experiments are magnetic would suggest that magnetite is a reaction product in all of the experiments. The formation of magnetite as a corrosion product of steel or iron might be expected under the anoxic conditions of these experiments.

A poorly crystalline iron oxyhydroxide phase, tentatively identified by XRD as åkaganeite [Fe(O,OH,Cl)] was found during Phase 1, in the iron corrosion products taken directly from the steel wire surfaces in NF-PRO Experiments 12, 16 and 17. However, neither åkaganeite nor any other crystalline iron oxyhydroxide phase was identified from these longer-term experiments studied under Phase 2.

Aragonite was also detected by XRD in samples MPLM767B, 771 and 773 but on the basis of petrographical evidence this is most probably derived from attached altered bentonite.

References

BASCOMB, C. L. 1964. Rapid method for the determination of cation-exchange capacity of calcareous and noncalcareous soils. *Journal of the Science of Food and Agriculture*, **12**, 821-823.

BRADBURY, M.H. AND BAEYENS, B. 2003. Porewater chemistry in compacted re-saturated MX-80 bentonite. *Journal of Contaminant Hydrology*, **61**, 329-338.

CARLSON, L., KARNLAND, O., OVERSBY, V.M., RANCE, A.P., SMART, N.R., SNELLMAN, M., VAHANEN, M. AND WERME, L.O. 2006 (in press). Experimental studies of the interactions between anaerobically corroding iron and bentonite. *Physics and Chemistry of the Earth*, **32**, 334-345.

CAVE, M R, MILODOWSKI, A E AND FRIEL, E N. 2004. Evaluation of a method for Identification of host physico-chemical phases for trace metals and measurement of their solid-phase partitioning in soil samples by nitric acid extraction and chemometric mixture resolution. *Geochemistry: Exploration, Environment, Analysis*, **4**, 71-86.

DEER, W.A., HOWIE, R.A. AND ZUSSMAN, J. 1962. *Rock Forming Minerals. Volume 3: Sheet Silicates*. Longmans, London.

GILLESPIE, M.R., LEADER, R.U., HIGGO, J.J.W., HARRISON, I., HARDS, V.L., GOWING, C.J.B., VICKERS, B.P., BOLAND, M.P. & MORGAN, D.J. 2000a CEC & Kd determination in landfill performance evaluation: a review of methodologies and preparation of standard materials for laboratory analysis. *Environment Agency R &D Technical Report*, **P340**

GILLESPIE, M.R., LEADER, R.U., HIGGO, J.J.W., HARRISON, I., HARDS, V.L., GOWING, C.J.B., VICKERS, B.P., BOLAND, M.P. & MORGAN, D.J. 2000b CEC & Kd determination in landfill performance evaluation: a review of methodologies and preparation of standard materials for laboratory analysis. *Environment Agency R &D Project Record,* **P1/254/01**

GILLESPIE, M.R., KEMP, S J, VICKERS, B P, WATERS, C AND GOWING, C J. 2001. Cation- exchange capacity (CEC) of selected lithologies from England, Wales and Scotland. *Environment Agency R &D Technical Report*, **P2-222/TR**.

GOLDSTEIN, J.I., NEWBURY, D.E., ECHLIN, P., JOY, D.C., FIORI, C. AND LIFSHIN, E. 1981. Scanning Electron Microscopy and X-Ray Microanalysis. Plenum Press, New York.

HERBERT, H.-J. AND MOOG, H.C. 1999. Cation exchange, interlayer spacing, and water content of MX-80 bentonite in high molar saline solutions. *Engineering Geology*, **54**, 55-65.

IDEMITSU, K., YANO, S., XIA, X., KIKUCHI, Y., INAGAKI, Y. AND ARIMA, T. 2003. Migration behaviour of iron in compacted bentonite under reducing condition using electromigration. *Material Research Society Symposium Proceedings***,** **757**, II3.7.1-II3.7.8.

KAMEI, G., ODA, C., MITSUI, S., SHIBATA, M. AND SHINOZAKI. 1999. Fe(II)-Na ion exchange at interlayers of smectite: adsorption-desorption experiments and a natural analogue. *Engineering Geology* , **54**, 15-20.

KOSTKA, J.E., WU, J., NEALSON, K.H. AND STUKI, J. 1999. The impact of structural Fe(III) reduction by bacteria on the surface chemistry of smectitic clay minerals. Geochimica et Cosmochimica Acta, **63**, 3705-3713.

MADSEN, F.T. 1998. Clay mineralogical investigations related to nuclear waste disposal. *Clay Minerals*, **33**, 109-129.

MILODOWSKI, A.E., CAVE, M.R., KEMP, S.J., TAYLOR, H., VICKERS, B.P., GREEN, K, WILLIAMS, C L AND SHAW, RA. 2007. Mineralogical investigations of the interaction between iron corrosion products and bentonite from the NF-PRO Experiments (Phase 1). *British Geological Survey Commissioned Report*, **CR/07/116**.

MOORE, D.M. AND REYNOLDS, R.C. 1997. *X-Ray Diffraction and the Identification and Analysis of Clay Minerals*, Second Edition. Oxford University Press, New York.

REYNOLDS, R.C. AND REYNOLDS, R.C. 1996. *Description of Newmod-for-Windows™. The calculation of one-dimensional X-ray diffraction patterns of mixed layered clay minerals*. R C Reynolds Jr., 8 Brook Road, Hanover, NH.

SMART, N.R., CARLSON, L., HUNTER, F.M.I., KARNLAND, O., PRITCHARD, A.M., RANCE, A.P. AND WERME, L.O. 2006. Interactions between iron corrosion products and bentonite. *Serco Assurance Report*, **SA/EIG/12156/C001**.

STUKI, J.W., LOW, P.F., ROTH, C.B. AND GOLDEN, D.C. 1984. Effects of oxidation state on octahedral iron on clay swelling. *Clays and Clay Minerals*, **32**, 357-362

VUORINEN, U. AND SNELLMAN, M. 1998. Finnish reference waters for solubility, sorption and diffusion studies. *Posiva Working Report*, **98-61**. 41 p., Posiva Oy, Helsinki, Finland.

WILSON, J., SAVAGE, D., CUADROS, J., SHIBATA, M. AND RAGNARSDOTTIR, K.V. 2006a. The effect of iron on montmorillonite stability. (I) Background and thermodynamic consideration*.* *Geochimica et Cosmochimica Acta*, **70**, 306-322.

WILSON, J., CRESSEY, G., CRESSEY, B., CUADROS, J., RAGNARSDOTTIR, K.V., SAVAGE, D. AND SHIBATA, M 2006b. The effect of iron on montmorillonite stability. (I) Experimental investigations. *Geochimica et Cosmochimica Acta*, **70**, 306-322.

Appendix 1 XRFS bulk chemical analysis of altered and unaltered bentonite

Sample No.	**MPLM767A**	**MPLM767B**	**MPLM770**	**MPLM771**	**MPLM773A**	**MPLM773B**
	Fresh bentonite *NFC1* *Sample 1 Cell 1*	**Altered bentonite** *NFC1* *Sample 1 Cell 1*	**Fresh bentonite** *NFC13* *Sample 1 Cell 13*	**Altered bentonite** *NFC4* *Sample 1 Cell 4*	**Fresh bentonite** *NFC13* *Sample 2 Cell 13*	**Altered bentonite** *NFC13* *Sample 2 Cell 13*
Element (as oxide)	**wt. %**					
SiO_2	62.29	60.52	59.65	61.46	62.26	59.88
TiO_2	0.16	0.16	0.16	0.16	0.17	0.15
Al_2O_3	20.30	19.76	19.45	20.09	20.25	19.50
Fe_2O_3(t)	4.02	6.96	3.73	5.37	4.38	7.40
Mn_3O_4	0.02	0.02	0.02	0.02	0.01	0.02
MgO	2.39	2.38	2.27	2.40	2.28	2.21
CaO	1.25	1.24	1.09	1.13	0.80	1.00
Na_2O	1.96	2.12	2.59	2.04	2.87	2.98
K_2O	0.59	0.60	0.59	0.58	0.59	0.59
P_2O_5	0.06	0.06	0.05	0.05	0.06	0.05
SO_3	0.2	0.2	0.1	0.2	0.2	0.1
Cr_2O_3	0.08	0.17	0.19	0.16	0.06	0.10
SrO	0.02	0.03	0.02	0.03	0.02	0.02
ZrO_2	0.02	0.02	0.02	0.02	0.03	0.02
BaO	0.05	0.05	0.05	0.05	0.06	0.04
NiO	<0.01	<0.01	<0.01	<0.01	<0.01	<0.01
CuO	<0.01	<0.01	<0.01	<0.01	<0.01	<0.01
ZnO	0.01	0.02	0.01	0.02	0.01	0.01
PbO	<0.01	<0.01	<0.01	<0.01	<0.01	<0.01
Loss on ignition	6.01	5.74	5.87	5.66	5.62	6.09
Total	99.43	100.05	95.86	99.44	99.67	100.16

Notes:

(i) Fe_2O_3(t) represents total iron expressed as Fe_2O_3.

(ii) SO_3 represents S retained in the fused bead after fusion at 1200 ºC.